J. Fluid Mech. (2019), *vol.* 877, *pp.* 282–329. © Cambridge University Press 2019
doi:10.1017/jfm.2019.608

A kinetic-based hyperbolic two-fluid model for binary hard-sphere mixtures

Rodney O. Fox[1,2,†]

[1]Department of Chemical and Biological Engineering, 618 Bissell Road, Iowa State University, Ames, IA 50011-1098, USA

[2]Center for Multiphase Flow Research and Education, Iowa State University, Ames, IA 50011-1096, USA

(Received 11 January 2019; revised 23 July 2019; accepted 23 July 2019; first published online 19 August 2019)

Starting from coupled Boltzmann–Enskog (BE) kinetic equations for a two-particle system consisting of hard spheres, a hyperbolic two-fluid model for binary, hard-sphere mixtures is derived with separate mean velocities and energies for each phase. In addition to spatial transport, the BE kinetic equations account for particle–particle collisions, using an elastic hard-sphere collision model, and the Archimedes (buoyancy) force due to spatial gradients of the pressure in each phase, as well as other forces involving spatial gradients (e.g. lift). In the derivation, the particles in a given phase have identical mass and volume, and have no internal degrees of freedom (i.e. the particles are adiabatic). The 'hard-sphere-fluid' phase is obtained in the limit where the particle diameter in one phase tends to zero with fixed phase density so that the number of fluid particles tends to infinity. The moment system resulting from the two BE kinetic equations is closed at second order by invoking the anisotropic Gaussian closure. The resulting two-fluid model for a binary, hard-sphere mixture therefore consists (for each phase $\alpha = 1, 2$) of transport equations for the mass ϱ_α, mean momentum $\varrho_\alpha \boldsymbol{u}_\alpha$ (where $\boldsymbol{u}_\alpha$ is the velocity) and a symmetric, second-order, kinetic energy tensor $\varrho_\alpha \boldsymbol{E}_\alpha = \frac{1}{2}\varrho_\alpha(\boldsymbol{u}_\alpha \otimes \boldsymbol{u}_\alpha + \boldsymbol{\sigma}_\alpha)$. The trace of the fluctuating energy tensor $\boldsymbol{\sigma}_\alpha$ is $\mathrm{tr}(\boldsymbol{\sigma}_\alpha) = 3\Theta_\alpha$ where Θ_α is the phase temperature (or granular temperature). Thus, $\varrho_\alpha E_\alpha = \varrho_\alpha \mathrm{tr}(\boldsymbol{E}_\alpha)$ is the total kinetic energy, the sum over α of which is the total kinetic energy of the system, a conserved quantity. From the analysis, it is found that the BE finite-size correction leads to exact phase pressure (or stress) tensors that depend on the mean-slip velocity $\boldsymbol{u}_{12} = \boldsymbol{u}_1 - \boldsymbol{u}_2$, as well as the phase temperatures for both phases. These pressure tensors also appear in the momentum-exchange terms in the mean momentum equations that produce the Archimedes force, as well as drag contributions due to fluid compressibility and a lift force due to mean fluid-velocity gradients. The closed BE energy flux tensors show a similar dependence on the mean-slip velocity. The characteristic polynomial of the flux matrix from the one-dimensional model is computed symbolically and depends on five parameters: the particle volume fractions φ_1, φ_2, the phase density ratio $\mathcal{Z} = \rho_f/\rho_p$, the phase temperature ratio $\Theta_r = \Theta_2/\Theta_1$ and the mean-slip Mach number $Ma_s = \boldsymbol{u}_{12}/\sqrt{5\Theta_1/3}$. By applying Sturm's Theorem to the characteristic polynomial, it

† Email address for correspondence: rofox@iastate.edu

https://doi.org/10.1017/jfm.2019.608 Published online by Cambridge University Press

is demonstrated that the model is hyperbolic over a wide range of these parameters, in particular, for the physically most relevant values.

Key words: particle/fluid flow, kinetic theory

1. Introduction

The long history, and numerous difficulties, of the development of hyperbolic two-fluid models for disperse multiphase systems has been reviewed by Lhuillier, Chang & Theofanous (2013). These authors note that most, if not all, of the models that have been proposed in the literature suffer from being mathematically ill posed (see Drew & Passman (1998), Vazquez-Gonzalez, Llor & Fochesato (2016) for other discussions of this topic). Moreover, well posedness of nonlinear multiphase flow models implies hyperbolicity of the underlying Cauchy problem (Métivier 2005). In practice, numerical simulations with non-hyperbolic two-fluid models diverge under grid refinement due to the complex eigenvalues in the continuum limit (see, e.g. Ndjinga 2007; Kumbaro & Ndjinga 2011). To remediate this problem, various *ad hoc* correction terms have been added to make the models well posed (see, e.g. Panicker, Passalacqua & Fox 2018), albeit with dubious physical justification (Lhuillier *et al.* 2013). In particular, many authors have resorted to neglecting the Archimedes force (see, e.g. Hank, Saurel & Le Metayer 2011), which is the root cause of non-hyperbolicity. In their review, Lhuillier *et al.* (2013) demonstrate that (i) it is critical to account for the kinetic energies of each phase and (ii) the hyperbolicity is linked to the relation between the forces and stresses (referred to hereinafter as the spatial fluxes) in the momentum and energy balances. In the context of this work, the two-fluid modelling described in Lhuillier *et al.* (2013) is done at the macroscopic level. In other words, the forces and fluxes are added at the level of the mass, momentum and energy balances without an underlying microscale model. Related approaches have been used by many other authors (see, e.g. Buyevich & Shchelchkova 1978; Nigmatulin 1979; Jackson 1997; Lhuillier & Theofanous 2010; McGrath II, St. Clair & Balachandar 2016; Saurel, Chinnayya & Carmouze 2017).

Similar to the kinetic-based approach used in this work, the works of Zhang & Prosperetti (1994) and Zhang, Ma & Rauenzahn (2006) treat the particle phase using a kinetic description in terms of the N-particle distribution function. In Zhang & Prosperetti (1994), the particles evolve in an Euler fluid and averaged equations are derived for the mass and momentum of each phase. These authors demonstrate that interphase momentum interactions due to the fluid pressure at the particle surfaces generates an additional stress tensor ($\boldsymbol{T}_C$ in their notation, see (10.9) in their article) in the fluid-phase momentum balance. In Zhang *et al.* (2006), the N-particle distribution function for a dense, binary particulate system is employed to derive the averaged equations for mass and momentum, and the interspecies stress tensor $\boldsymbol{\sigma}^{(21)}$ is shown to arise from the binary interaction forces between particles of different types. By choosing a specific interaction force (i.e. binary hard-sphere collisions), in the present work explicit expressions are derived for the intra- and interspecies stress tensors and interaction forces in the momentum balances. In addition, closed forms for the total energy equations for each particulate type are derived, allowing us to investigate the hyperbolicity of the resulting two-fluid model. Here, the interaction force is specified to be hard-sphere collisions, allowing us to derive closed expressions for

https://doi.org/10.1017/jfm.2019.608 Published online by Cambridge University Press

the inter- and intra-species stress tensors, as well as the total energy equations for each species. Because binary hard-sphere collisions are a particular form of binary interactions, the mass and momentum balances derived in the present work have the same structure as in Zhang *et al.* (2006). Most notably the momentum equations contain an interspecies stress tensor that plays a significant role is the hyperbolicity of the system.

Given the difficulties described in Lhuillier *et al.* (2013) that are faced when formulating a generic two-fluid model for disperse multiphase systems, it would seem judicious to first derive a model for a specific system starting from a microscale description with simple, well-defined physics. Such a system is a binary mixture of elastic hard spheres with dissimilar properties, which has been widely analysed in the context of the kinetic theory of gas dynamics (Enskog 1911*a*,*b*; Chapman 1912; Chapman & Cowling 1952; Kolodner 1957; Sirovich 1962; Morse 1963; Hamel 1966; Goldman & Sirovich 1967; Barajas, Garcia-Colin & Pinã 1973; Santos, Yuste & López de Haro 1999). Starting from the Boltzmann–Enskog (BE) kinetic equations for a binary system, the principal objective of this work is to derive a two-fluid model for the mass, momentum and kinetic energy of each phase for a hard-sphere mixture that includes the Archimedes force, as well as other forces depending on spatial gradients (e.g. lift). Then, by going to the limit where the volume and mass for type-1 particles is very much smaller than for type-2 particles, we wish to develop a two-fluid model for fully compressible fluid–particle flow wherein all of the fluxes and forces are derived exactly from the microscale description. (The two-fluid model is compressible in the sense that each phase is governed by the gas-dynamic equations for mass, momentum and energy in the absence of the other phase.) The main limitation of this approach is that it accounts only for spatial gradients up to first order (Barajas *et al.* 1973); however, this is exactly what is required for the spatial fluxes and the Archimedes force. Note that unlike in the 'classical' kinetic theory for gas dynamics (see, e.g. Sirovich 1962; Hamel 1966), in the context of two-fluid models we do not make use the Chapman–Enskog expansion (Chapman & Cowling 1952; Garzó, Dufty & Hrenya 2007) about the system's mean velocity and temperature. Instead, the two-fluid model is written in terms of the velocity moments for each phase up to second order for a non-dissipative system. Remarkably, we shall see that the terms in the two-fluid model that determine whether the system is hyperbolic can all be expressed in closed form, thereby removing any ambiguity in the definition of the model. Thus, while the application of the two-fluid model derived in this work is limited to a specific system (i.e. binary, hard-sphere mixture), it should be possible to arrive at some general conclusions concerning the relationship between the fluxes and forces in hyperbolic two-fluid models. As noted above, our results for the mathematical form of the momentum equations agree with Zhang *et al.* (2006) whose derivation is based on a Liouville equation for dense binary mixtures with an interaction force between particles.

Starting with the seminal work of Cravath (1930), many authors have investigated the kinetic theory of molecular-scale hard spheres with disparate masses (e.g. Kolodner 1957; Sirovich 1962, 1963; Morse 1963, 1964; Hamel 1965, 1966; Goldman & Sirovich 1967, 1969). In these works, the Boltzmann collision operator (i.e. neglecting two-particle correlations) is applied to binary systems with nearly equal mole fractions (such as in a plasma). The primary focus of these works is to investigate the epochal-relaxation scenario introduced by Grad (1960). Denoting the mean velocity of each species by $\boldsymbol{u}_\alpha$ and the temperature by Θ_α (see § 2 for details), in a binary system at equilibrium $\boldsymbol{u}_1 = \boldsymbol{u}_2$ and $m_1\Theta_1 = m_2\Theta_2$, where m_α is the species mass.

https://doi.org/10.1017/jfm.2019.608 Published online by Cambridge University Press

Epochal relaxation towards this equilibrium applies when $m_1 \ll m_2$ (see, e.g. Morse 1963), and predicts that the 'diffusion velocity' $|\boldsymbol{u}_{12}| = |\boldsymbol{u}_1 - \boldsymbol{u}_2|$ approaches zero much faster than the temperature difference $|m_1\Theta_1 - m_2\Theta_2|$. In practice, this implies that the mixture can be described by one momentum and two energy equations (i.e. the well-known two-temperature model for plasmas) (Sirovich 1962; Morse 1963; Hamel 1965). For hard-sphere collisions, Morse (1963) introduced a 'diffusion' Mach number $M_d = |\boldsymbol{u}_{12}|/\sqrt{\Theta_1 + \Theta_2}$ and derived the relaxation time scales valid for spatially homogeneous systems with $M_d < 0.32$. In subsequent work on spatially inhomogeneous systems, Hamel (1966) distinguished between an equal-molar mixture and a system in which the heavy species is a trace component (i.e. when its mole fraction is negligible). The latter occurs, for example, when the diameters d_α are related by $d_1 \ll d_2$ (which is the case considered in this work). For such cases, Hamel (1966) demonstrated that epochal relaxation does not occur and, hence, two momentum equations are needed to describe the binary system. In summary, the works of Hamel (1966) and Goldman & Sirovich (1967) were the first complete kinetic-based derivations of a two-fluid model for gas mixtures. Interestingly, not much use has been made of these models in the gas-dynamics or granular flow literature. For the former, most practical system have $M_d \ll 1$ so that the 'diffusion velocity' can be replaced with a gradient-diffusion model. For the latter, the Boltzmann collision operator must be replaced by a BE kinetic model to account for the finite size of the particles. As we shall see in § 3, the BE collision model modifies both the relaxation time scales towards equilibrium and the spatial fluxes (and, hence, the hyperbolicity) of the two-fluid model.

For gas–particle flows with heavy particles (e.g. Sinclair & Jackson 1989; Wagner *et al.* 2012), the dominant exchange term is drag (Maxey 2017) (see, e.g. Capecelatro, Desjardins & Fox 2016*a*, for an analysis of the relative magnitudes of the different forces). Nonetheless, the Archimedes (or buoyancy) force is included in Euler–Lagrange (EL) simulations (Capecelatro & Desjardins 2013). The coupling of the Lagrangian particles with the Eulerian fluid is done with a filter that smooths out the small scales of the order of the particle diameter. This explicit filtering will likely eliminate any small-scale instabilities present in non-hyperbolic two-fluid models (Ndjinga 2007; Kumbaro & Ndjinga 2011; Panicker *et al.* 2018). From EL simulations, it has been found that the particle-phase granular temperature is significant due to two-way coupling (Capecelatro, Desjardins & Fox 2015; Capecelatro *et al.* 2016*a*; Capecelatro, Desjardins & Fox 2016*b*) and/or boundary conditions (Vié, Doisneau & Massot 2015; Chalons *et al.* 2017; Fox, Laurent & Vié 2018). Indeed, for strong two-way coupling particle clusters are produced with even the simplest drag model (Agrawal *et al.* 2001; Capecelatro *et al.* 2015; Capecelatro, Desjardins & Fox 2018). The corresponding two-fluid model for collisional particles should be able to account for the anisotropy of the particle-phase pressure tensor (Fox 2014; Vié *et al.* 2015; Kong & Fox 2017). In applications of the two-fluid model with a compressible fluid, the particle-phase fluctuating energy is usually either neglected (see, e.g. Theofanous & Chang 2017), or treated in an *ad hoc* manner (see, e.g. Hank *et al.* 2011). Only the two-fluid model developed by Houim & Oran (2016) contains a complete description of the coupling between the phases. As we shall see later, the model developed in this work has a similar form to their model, but with more complex expressions for the fluxes and momentum/energy-exchange terms. For compressible gas–particle flow applications (Ling *et al.* 2012; Wagner *et al.* 2012; Theofanous, Mitkin & Chang 2016, 2018), the two-fluid model developed in this work could be employed; however, additional terms would be required to account for

https://doi.org/10.1017/jfm.2019.608 Published online by Cambridge University Press

specific physics of such flows. For example, a key open point for such applications is the drag model, which must account for the fluid Mach number (see Ling *et al.* (2012), Theofanous & Chang (2017) for examples).

When developing two-fluid models for gas–particle flows, it is important to recognize that bi-modal velocity distribution functions cannot be captured by a moment closure for the particle phase that does not include at least the third-order velocity moments (see, e.g. Desjardins, Fox & Villedieu 2008; Fox 2008, 2009, 2012; Marchisio & Fox 2013; Vié *et al.* 2015). Thus, the particle-phase description developed in this work based on the anisotropic Gaussian, which closes at second order, should not be used for very dilute flows where particle–particle collisions are rare. Instead, closure at fourth order using a quadrature-based model such as the multi-Gaussian model (Chalons *et al.* 2017) or the hyperbolic quadrature method of moments (Fox *et al.* 2018; Patel, Desjardins & Fox 2019) should be preferred. In any case, the moment equations for the particle phase are derived from the BE kinetic equation. Thus, the main difference with the anisotropic Gaussian model is the assumed form of the particle-phase velocity distribution function (VDF) used to close the higher-order moments. For the fluid phase, closure at second order, as done here, should be sufficient unless the fluid is a rarefied gas (Struchtrup 2005; Torrilhon 2016). In principle, extension beyond an Euler-level description of the fluid is possible using a Chapman–Enskog expansion as done by Levermore (1996).

The remainder of this work is organized as follows. In § 2, we describe the BE kinetic model for binary, hard-sphere mixtures, leaving the detailed calculations involving the collision integrals to appendix A, but including a model for the particle-pair distribution function that produces the Archimedes force that was lacking in previous kinetic theory derivations. In § 3 we present the conservation equations for the velocity moments up to second order in various equivalent forms. The fluid limit, found by letting the volume of type-1 particles become very small while increasing their number with fixed mass concentration, is discussed in § 4. Next, in § 5 we use Sturm's Theorem to analyse the eigenvalues of the one-dimensional (1-D) fluid–particle model for all physically realistic values of the five model parameters. Finally, in § 6 we discuss the principal findings from the two-fluid model derived from the BE kinetic equation, and, from these, draw some general conclusions concerning the formulation of hyperbolic two-fluid models.

2. Kinetic model for binary mixture

2.1. *Boltzmann–Enskog kinetic equations*

We begin by introducing the VDFs $f_\alpha(t, \boldsymbol{x}, \boldsymbol{v})$ for each type of particle $\alpha = 1, 2$ with spatial location $\boldsymbol{x} \in \mathbb{R}^3$, and velocity $\boldsymbol{v} \in \mathbb{R}^3$. The integration of the VDFs over velocity phase space yields the total mass of particles of type α per unit volume (i.e. the mass concentration), which we denote by $\varrho_\alpha(t, \boldsymbol{x})$. These VDFs are assumed to obey the following coupled BE kinetic equations (Chapman & Cowling 1952; Tham & Gubbins 1971; Barajas *et al.* 1973; Marchisio & Fox 2013) (the same equations are used with the Boltzmann collision operator (Grad 1960; Sirovich 1962; Hamel 1966), but with a simpler definition for $\mathcal{C}_\alpha$. The N-particle probability function used in Zhang *et al.* (2006) can be used to derive (2.1) for the one-particle VDF for binary interactions. Nonetheless, the closure of the collision terms requires a model for the two-particle VDF expressed in terms of the one-particle VDF)

$$\partial_t f_1 + \boldsymbol{v} \cdot \partial_{\boldsymbol{x}} f_1 = \mathcal{C}_1, \quad \partial_t f_2 + \boldsymbol{v} \cdot \partial_{\boldsymbol{x}} f_2 = \mathcal{C}_2. \tag{2.1a,b}$$

https://doi.org/10.1017/jfm.2019.608 Published online by Cambridge University Press

The first two terms on the left-hand sides are accumulation and free transport, respectively. The terms $\mathcal{C}_\alpha$ on the right-hand sides correspond to particle–particle collisions, and include contributions due to like and unlike particles. In the model equations below, all collisions are assumed to be elastic so that the total energy of the system is conserved. The exact forms of the (inelastic) collision terms are given in appendix A, along with the derivation of the collisional contributions to the moment equations starting from (2.1). The inelastic forms of the collision terms can be used to describe granular flows, but a thermal energy balance would then be required to account for the loss of kinetic energy due to collisions. (Alternatively, in the fluid–particle limit, the kinetic energy dissipated in particle–particle collisions could be included as a source term in the fluid energy balance.) Results for the moment equations with the Boltzmann collision operator can be found in the literature (Grad 1960; Sirovich 1962; Hamel 1966). Here, it suffices to remark that the BE model accounts for the finite size of the particles and these additional terms are the primary focus of the present work. For clarity, in the moment equations these terms will be identified using the subscript $_{BE}$.

2.2. *Definition of hard-sphere model parameters*

In the following sections, we consider the case where $d_1 \leqslant d_2$ (and eventually $d_1 \ll d_2$, corresponding to the fluid–particle limit). Hereinafter, $V_\alpha = (\pi/6)d_\alpha^3$ and m_α are the volume and mass, respectively, of a single particle of type α. Note that the total volume of particles of type α per unit volume is $\varphi_\alpha := (V_\alpha/m_\alpha)\varrho_\alpha$. Thus, $0 < \varphi_1 + \varphi_2 < 1$, i.e. the sum of the particle volume concentrations do not sum to unity. The particles are assumed to have no internal degrees of freedom and, hence, (2.1) will conserve the total mass, momentum and energy of the particles. Body forces are not included in (2.1) (see appendix B for details on how to add them) because they do not change the spatial fluxes. The definitions of the other parameters appearing in the kinetic model are as follows. The collisional cross-section diameter for unlike collisions is

$$d := \tfrac{1}{2}(d_1 + d_2), \tag{2.2}$$

from which we define the geometric parameter $\chi_\alpha := d/d_\alpha$. The mass ratios are defined by

$$\mu_\alpha := \frac{2m_\alpha}{m_1 + m_2}, \tag{2.3}$$

and the material densities of the particles by ρ_α. Because these densities are assumed constant, we have $m_\alpha = \rho_\alpha V_\alpha$. By definition,

$$\mu_1 + \mu_2 = 2, \quad \text{and} \quad \rho^\star := \rho_1 \chi_2^3 \mu_2 = \rho_2 \chi_1^3 \mu_1 = \frac{\rho_1 \rho_2 (d_1 + d_2)^3}{4(\rho_1 d_1^3 + \rho_2 d_2^3)}, \tag{2.4a,b}$$

which can be used to demonstrate the conservation of momentum and energy. The mean velocities $\boldsymbol{u}_\alpha$ and velocity covariance tensors $\boldsymbol{\sigma}_\alpha$ are found from f_α as described in § 3. The phase temperatures are then defined in terms of the trace $\Theta_\alpha := \frac{1}{3}\mathrm{tr}(\boldsymbol{\sigma}_\alpha)$, and the 'mixture' temperature by

$$\Theta := \Theta_1 + \Theta_2 + \tfrac{1}{3}|\boldsymbol{u}_{12}|^2, \tag{2.5}$$

where the mean-slip velocity is defined by $\boldsymbol{u}_{12} := \boldsymbol{u}_1 - \boldsymbol{u}_2 = -\boldsymbol{u}_{21}$.

https://doi.org/10.1017/jfm.2019.608 Published online by Cambridge University Press

2.3. *Definition of particle-pair distribution function*

In the BE kinetic theory of hard-sphere mixtures with finite-size particles, the particle-pair distribution function appearing in the collision integrals (see appendix A for more details) plays a key role as it determines which forces and fluxes beyond the perfect-gas description will appear in the two-fluid model. Thus, in order to produce the Archimedes force in the fluid–particle limit, we propose the following approximation for the particle-pair distribution function with the geometric parameter $\frac{1}{2} \leqslant y \leqslant 1$ (aside from the factors h_α and $\mathcal{V}_{\alpha\beta}$, this model is essentially the same as the truncated series expansion for dense gases proposed by Enskog (1911*a*); see chap. 16 in Chapman & Cowling (1952) for details)

$$f^{(2)}(\boldsymbol{x} - yd\,\boldsymbol{x}_{12}, m_1, \boldsymbol{v}_1; \boldsymbol{x} + (1-y)d\,\boldsymbol{x}_{12}, m_2, \boldsymbol{v}_2) \approx g_{12} f_1 f_2 + \frac{d}{\mathcal{V}_{12}} \boldsymbol{x}_{12} \cdot [(1-y)\varrho_1 f_1^\star \partial_{\boldsymbol{x}}(h_2 f_2) - y\varrho_2 f_2^\star \partial_{\boldsymbol{x}}(h_1 f_1)], \tag{2.6}$$

where the volume ratio is defined by ($\mathcal{V}_{\alpha\alpha} = 4$)

$$\mathcal{V}_{\alpha\beta} := \frac{(d_\alpha + d_\beta)^3}{d_\alpha^3 + d_\beta^3} = \frac{\text{collision volume}}{\text{sum of particle volumes}}. \tag{2.7}$$

In (2.6), $f_\alpha(\boldsymbol{x}, \boldsymbol{v}_\alpha) = \varrho_\alpha(\boldsymbol{x}) f_\alpha^\star(\boldsymbol{x}, \boldsymbol{v}_\alpha)$ defines the normalized VDF $f_\alpha^\star$ and the unit vector $\boldsymbol{x}_{12}$ between particle centres is defined in (A 1). The model in (2.6) is mathematically consistent in the sense that it treats both types of particles in the same manner, i.e. it obeys the indifferentiability principle (Garzó, Santos & Brey 1989; Andries, Aoki & Perthame 2002). When applied to like particles (i.e. $m_1 = m_2$ and $d_1 = d_2$), the gradient terms reduce to expressions involving $\boldsymbol{x}_{12} \cdot \partial_{\boldsymbol{x}} h_\alpha \varphi_\alpha$. The indifferentiability principle also holds for the collision integrals in appendix A, and is thus inherited from the hard-sphere collision operator.

The first term on the right-hand side of (2.6) is the classical Boltzmann approximation where spatial gradients are neglected. The second term on the right-hand side accounts for spatial gradients at the particle scale. In particular, in the fluid limit where $y \to 1$, equation (2.6) models how the spatial gradients in fluid properties vary on the scale of the particle diameter d_2. Obviously, equation (2.6) neglects higher-order terms in the expansion about the point $\boldsymbol{x}$. However, this is consistent with the observations in Barajas *et al.* (1973). Nonetheless, we must emphasize that the form of the first-order derivative term in (2.6) is chosen to capture the limit where $y \to 1$ and, hence, it may not be physically accurate for equal-size particles where $y = 1/2$, but with different densities.

As will be discussed in § 3.6, the functions h_1 and h_2 are chosen such that the isotropic flux pressure and the buoyancy pressure are identical for each phase. This specification yields

$$h_1 := 1 + \mathcal{V}_{11}\varphi_1 g_0 + \mathcal{V}_{12}\varphi_2 g_{12}, \quad h_2 := 1 + \mathcal{V}_{22}\varphi_2 g_0 + \mathcal{V}_{21}\varphi_1 g_{12}. \tag{2.8a,b}$$

In order to arrive at this definition for h_α, the expansion point in the BE collision integral, defined by the choice of y, must be chosen such that the indifferentiability principle holds (these definitions provide alternative expressions for $\rho^\star = (\mathcal{V}_{12}\rho_1\mu_2/8y) = (\mathcal{V}_{12}\rho_2\mu_1/8(1-y))$, which we use to eliminate $\rho^\star$ and y in the moment equations

https://doi.org/10.1017/jfm.2019.608 Published online by Cambridge University Press

in § 3. Note that specifying y fixes the interspecies stress tensor contribution in both phases, and thus overcomes the symmetry issue discussed in Zhang *et al.* (2006))

$$y := \frac{d_2^3}{d_1^3 + d_2^3} = \frac{\text{volume of particle 2}}{\text{sum of particle volumes}} \quad \Longrightarrow \quad \mathcal{V}_{12} = 8y\chi_2^3 = 8(1-y)\chi_1^3 = \mathcal{V}_{21}. \tag{2.9}$$

Note that y depends only on the particle diameters and the h_α are symmetric with respect to $\alpha = 1, 2$. Furthermore, $\mathcal{V}_{\alpha\beta}$, y and h_α are purely geometrical and do not depend on the particle masses. The first contribution to h_α is from the Boltzmann approximation for a perfect gas. The second is the Enskog correction due to the excluded volume from particles of the same type, while the third arises from the excluded volume of the other particles. For equal-size particles, equation (2.8) yields $h_1 = h_2 = 1 + 4\varphi g_0$ (i.e. the indifferentiability principle holds); and for a perfect gas (see § 4) $h_1 = 1/(1-\varphi_2) = 1/\alpha_f$ so that $\varrho_1 h_1 = \rho_f$ is the gas-phase density (which should not be confused with ρ_1 or ρ_2). For any other choice of y than (2.9), the indifferentiability principle will not be satisfied for equal-sized particles. Thus, equation (2.9) is unique given the assumption of equality between the flux and buoyancy pressures.

In the limit where $d_1 \ll d_2$, $\mathcal{V}_{12} \to 1$ and $y \to 1$, whereas $\mathcal{V}_{12} = 4$ and $y \to 1/2$ when $d_1 = d_2$. In the fluid–particle limit introduced in § 4, (2.6) reduces to

$$f^{(2)}(\boldsymbol{x} - d\,\boldsymbol{x}_{12}, m_1, \boldsymbol{v}_1; \boldsymbol{x}, m_2, \boldsymbol{v}_2) \approx g_{12} f_1 f_2 - \tfrac{1}{2} d_2 \boldsymbol{x}_{12} \cdot \varrho_2 f_2^\star \partial_{\boldsymbol{x}}(h_1 f_1). \tag{2.10}$$

The first term on the right-hand side of (2.10) is the molecular chaos hypothesis (Cercignani 1988) with the excluded volume correction, while the second accounts for the spatial gradient of $h_1 f_1$ across a particle of diameter d_2. (For the Boltzmann collision operator, $f^{(2)} = f_1 f_2$ and, hence, g_{12} and the gradient term arise due to the finite particle size.) Note that when evaluating the collision integral $\int_{\mathbb{S}^+}$, the surface $\mathbb{S}^+$ corresponds to the surface of type-2 particles in the fluid–particle limit. In other words, the last term in (2.10) models the changes in $h_1 f_1$ (i.e. the fluid-particles' VDF) on the surface of type-2 particles. In principle, additional forces such as virtual mass could be accounted for by modifying (2.6), but this is very challenging to do based on physical arguments (Chliamovitch, Malaspinas & Chopard 2017). Nonetheless, as is well known (Lhuillier *et al.* 2013), inclusion of the Archimedes force often leads to non-hyperbolic two-fluid models, so we restrict our hyperbolicity analysis to (2.10) in this work.

Furthermore, it is important to note that when applied to like particles of type-2 (i.e. macroscale particles), equation (2.10) completely neglects particle–particle velocity correlations mediated by the fluid phase (sometimes referred to as three-way coupling), which are known to be very important, for example, in dense inertial suspensions (Blanc *et al.* 2013; Guazzelli & Pouliquen 2018). Thus, the resulting two-fluid model will at best be accurate for gas–solid flows where the material density of the solid phase is much larger than that of the fluid phase. In such systems, the forms of the inter- and intra-particle stress tensors are largely determined by particle–particle collisions with the fluid playing a negligible role (e.g. modifying the coefficient of restitution). In principle, the N-particle probability function in Zhang *et al.* (2006) overcomes this limitation, but appropriate (closed) forms for the particle–particle interaction force must be postulated to close the moment system arising from the Liouville equation. An alternative approach could be to modify the stress tensors and interaction forces to account for the presence of the fluid phase as suggested in Zhang & Prosperetti (1994). Particle-resolved direction-numerical simulations could a useful tool for validating such closures (see, e.g. Tenneti & Subramaniam 2014, for examples). However, care must be taken to ensure that the resulting two-fluid model is hyperbolic when developing such closures.

https://doi.org/10.1017/jfm.2019.608 Published online by Cambridge University Press

2.4. *Definition of radial distribution function*

The radial distribution function g_{12} depends on the total volume concentration $\varphi := \varphi_1 + \varphi_2$. For a binary, hard-sphere mixture g_{12} can be approximated as (Santos *et al.* 1999; Hansen-Goos & Roth 2006)

$$g_{12} = \frac{1}{1-\varphi} + \left(g_0 - \frac{1}{1-\varphi} \right) \frac{\langle d^2 \rangle}{\langle d^3 \rangle} \frac{d_1 d_2}{d}, \tag{2.11}$$

wherein g_0 is modelled as (Carnahan & Starling 1969)

$$g_0 = \frac{2-\varphi}{2(1-\varphi)^3}. \tag{2.12}$$

In (2.11), $\langle d^n \rangle := x_1 d_1^n + x_2 d_2^n$ where $x_\alpha := (\varrho_\alpha / m_\alpha)/(\varrho_1/m_1 + \varrho_2/m_2)$ is the number (or mole) fraction of particles of type α. This model for g_{12} is a linear interpolation between the limit $d_1 = d_2$ where $g_{12} = g_0$, and the limit $d_1 \ll d_2$ where $g_{12} = (1/1-\varphi)$ accounts for the excluded volume occupied by the large particles. In Santos *et al.* (1999), the model is validated for diameter ratios down to 0.05 against molecular dynamic simulations. It should be noted that (2.11) does not include non-equilibrium effects due, for example, to a mean-slip velocity in fluid–particle systems, quantified by the mean-slip Mach number $Ma_s := \boldsymbol{u}_{12}/\sqrt{5\Theta_1/3}$. As discussed in appendix A, it is possible to include corrections to g_{12} that depend on Ma_s but further research is needed to validate such corrections.

In this work, we consider only kinetic models with moments up to second order, which is appropriate for collisional flows (Fox 2014). The higher-order moments are closed using the anisotropic Gaussian (AG) approximation (Levermore & Morokoff 1996; Vié *et al.* 2015); most notably the third-order central moments $\boldsymbol{Q}$ are null. To go beyond this assumption, it is possible to a derive transport equation for $\boldsymbol{Q}$ (and higher-order moments) (Fox *et al.* 2018), or to employ a Chapman–Enskog expansion (Chapman & Cowling 1952; Levermore & Morokoff 1996) to express $\boldsymbol{Q}$ in terms of the spatial gradients of lower-order moments. However, as such terms do not change the hyperbolicity of the two-fluid model, the AG approximation suffices for our purposes. Finally, we should note that the moment equations derived in § 3 can be applied to polydisperse rapid granular and gas–particle flows with minimal modifications (Kong & Fox 2019).

3. Moment equations

Starting from (2.1) and using the closure in (2.6), we first find the transport equations for the velocity moments up to second order defined by

$$\varrho_\alpha := \int_{\mathbb{R}^3} f_\alpha \, \mathrm{d}\boldsymbol{v}, \quad \varrho_\alpha \boldsymbol{u}_\alpha := \int_{\mathbb{R}^3} f_\alpha \boldsymbol{v} \, \mathrm{d}\boldsymbol{v}, \quad \varrho_\alpha \boldsymbol{E}_\alpha := \frac{1}{2} \int_{\mathbb{R}^3} f_\alpha \boldsymbol{v} \otimes \boldsymbol{v} \, \mathrm{d}\boldsymbol{v}. \tag{3.1a–c}$$

The symmetric, second-order tensor $\boldsymbol{E}_k$ can be decomposed as

$$\boldsymbol{E}_\alpha = \tfrac{1}{2}(\boldsymbol{u}_\alpha \otimes \boldsymbol{u}_\alpha + \boldsymbol{\sigma}_\alpha). \tag{3.2}$$

The trace of $\varrho_\alpha \boldsymbol{E}_\alpha$, denoted by $\varrho_\alpha E_\alpha$, corresponds to the total energy in phase α. Note that the primitive variables for the phases are ϱ_α, $\boldsymbol{u}_\alpha$ and $\boldsymbol{\sigma}_\alpha$; and all other quantities appearing in the model can be written in terms of these variables. The (classical but tedious) mathematical details of the derivation of the BE collisional contributions to the moment equations are provided in appendix A. Hereinafter, we will limit our comments to the physical interpretation of these terms. As noted earlier, particular attention should be paid to the BE terms, which do not appear in previous derivations (e.g. Sirovich 1962; Hamel 1966).

https://doi.org/10.1017/jfm.2019.608 Published online by Cambridge University Press

3.1. *Mass balances*

The balance equations for mass found from (2.1) are

$$\partial_t \varrho_1 + \partial_{\boldsymbol{x}} \cdot \varrho_1 \boldsymbol{u}_1 = 0, \quad \partial_t \varrho_2 + \partial_{\boldsymbol{x}} \cdot \varrho_2 \boldsymbol{u}_2 = 0. \tag{3.3a,b}$$

Here we have used $\int \mathcal{C}_\alpha \, \mathrm{d}\boldsymbol{v} = 0$, i.e. the collisions do not change the particle masses. The system density $\varrho := \varrho_1 + \varrho_2$ is a conserved quantity.

3.2. *Momentum balances*

The balance equations for mean momentum are

$$\left.\begin{aligned} \partial_t \varrho_1 \boldsymbol{u}_1 + \partial_{\boldsymbol{x}} \cdot (\varrho_1 \boldsymbol{u}_1 \otimes \boldsymbol{u}_1 + \varrho_1 \boldsymbol{\sigma}_1 + \boldsymbol{P}_1 + \boldsymbol{P}_{12}) &= \boldsymbol{C} - K\boldsymbol{u}_{12}, \\ \partial_t \varrho_2 \boldsymbol{u}_2 + \partial_{\boldsymbol{x}} \cdot (\varrho_2 \boldsymbol{u}_2 \otimes \boldsymbol{u}_2 + \varrho_2 \boldsymbol{\sigma}_2 + \boldsymbol{P}_2 + \boldsymbol{P}_{21}) &= -\boldsymbol{C} + K\boldsymbol{u}_{12}. \end{aligned}\right\} \tag{3.4}$$

The collisional pressure tensors (e.g. $\boldsymbol{P}_1$ and $\boldsymbol{P}_{12}$) and the source terms on the right-hand side of (3.4) are presented below. It is important to recognize that the collisional pressure tensors for like and unlike collisions arise from the same physical mechanisms and, therefore, must both be included in the momentum balances. Moreover, for hard-sphere collisions these pressure tensors are exact (i.e. they do not depend on the form of the velocity VDF). For mono-disperse granular flows, $\boldsymbol{P}_\alpha$ is the same as in previous derivations (see, e.g. Jenkins & Savage 1983). From (3.4), we can observe that the system momentum $\varrho \boldsymbol{u} := \varrho_1 \boldsymbol{u}_1 + \varrho_2 \boldsymbol{u}_2$ is a conserved quantity. As discussed in Zhang *et al.* (2006), the interspecies stress $\boldsymbol{\sigma}^{(12)} = -(\boldsymbol{P}_{12} + \boldsymbol{P}_{21})/\varphi_1$ is non-zero and contributes to the total mixture stress, as it should to satisfy the indifferentiability principle. However, the expression for $\boldsymbol{T}_C$ $(= \boldsymbol{\sigma}^{(21)})$ in (10.9) of Zhang & Prosperetti (1994) has positive trace, which implies a negative contribution to the mixture pressure. In contrast, the trace of $\boldsymbol{P}_{\alpha\beta}$ is always non-negative, implying a positive contribution to the mixture pressure. In terms of the hyperbolicity of the system, a negative pressure contribution increases the likelihood of having complex eigenvalues.

The drag coefficient on the right-hand side of (3.4), which results directly from the unclosed collision integral in (A 30), is approximated by (Gross & Krook 1956; Morse 1963; Andries *et al.* 2002; Marchisio & Fox 2013)

$$K = \pi g_{12} \varrho_1 \varrho_2 \sqrt{\frac{\Theta}{2}} \frac{(d_1 + d_2)^2}{m_1 + m_2} = 6 g_{12} \varrho_1 \varrho_2 \sqrt{\frac{\Theta}{2}} \frac{(d_1 + d_2)^2}{\rho_1 d_1^3 + \rho_2 d_2^3}. \tag{3.5}$$

As drag does not contribute to the spatial fluxes, the exact form of K will not be important when determining whether the two-fluid model is hyperbolic. However, g_{12} and g_0 appear in the collisional pressure tensors below, so it is important to keep in mind that the model in (2.11) is limited to small Ma_s.

In contrast to the drag term, the collisional pressure tensors for like ($\boldsymbol{P}_1$, $\boldsymbol{P}_2$) and unlike ($\boldsymbol{P}_{12}$, $\boldsymbol{P}_{21}$) particles directly affect the system eigenvalues. As shown in appendix A, these symmetric second-order tensors can be computed exactly and are defined by

$$\left.\begin{aligned} \boldsymbol{P}_1 &:= \tfrac{1}{5} \mathcal{V}_{11} \varrho_1 \varphi_1 g_0 (3\Theta_1 \boldsymbol{I} + 2\boldsymbol{\sigma}_1), \quad & \boldsymbol{P}_2 &:= \tfrac{1}{5} \mathcal{V}_{22} \varrho_2 \varphi_2 g_0 (3\Theta_2 \boldsymbol{I} + 2\boldsymbol{\sigma}_2), \\ \boldsymbol{P}_{12} &:= \tfrac{1}{5} \mathcal{V}_{12} \mu_2 \varrho_1 \varphi_2 g_{12} \boldsymbol{P}_{BE}, \quad & \boldsymbol{P}_{21} &:= \tfrac{1}{5} \mathcal{V}_{12} \mu_1 \varrho_2 \varphi_1 g_{12} \boldsymbol{P}_{BE}, \end{aligned}\right\} \tag{3.6}$$

https://doi.org/10.1017/jfm.2019.608 Published online by Cambridge University Press

where the BE contribution from unlike collisions is

$$\boldsymbol{P}_{BE} := \tfrac{3}{2}\Theta\boldsymbol{I} + \boldsymbol{\sigma}_1 + \boldsymbol{\sigma}_2 + \boldsymbol{u}_{12} \otimes \boldsymbol{u}_{12}. \tag{3.7}$$

As shown in appendix A, the relations in (3.6) and (3.7) are exact in the sense that they do not depend on the shapes of the VDFs. The same is true for the momentum-exchange terms on the right-hand side of (3.4), defined by

$$\boldsymbol{C} := \tfrac{1}{5}\mu_2\varphi_2(\partial_{\boldsymbol{x}} - \partial_{\boldsymbol{x}}^{(2)}) \cdot \varrho_1 h_1 \boldsymbol{P}_{BE} - \tfrac{1}{5}\mu_1\varphi_1(\partial_{\boldsymbol{x}} - \partial_{\boldsymbol{x}}^{(1)}) \cdot \varrho_2 h_2 \boldsymbol{P}_{BE}, \tag{3.8}$$

where the gradient operator $\partial_{\boldsymbol{x}}^{(\alpha)}$ acts only on velocity statistics of type-α particles (e.g. $\partial_{\boldsymbol{x}}^{(1)}\boldsymbol{u}_1 = \partial_{\boldsymbol{x}}\boldsymbol{u}_1$ but $\partial_{\boldsymbol{x}}^{(1)}\boldsymbol{u}_2 = \boldsymbol{0}$). Note that $\boldsymbol{P}_{BE}$ involves only velocity statistics (and not ϱ_α). Thus, for example, we have the identity

$$(\partial_{\boldsymbol{x}} - \partial_{\boldsymbol{x}}^{(2)}) \cdot \varrho_1 h_1 \boldsymbol{P}_{BE} = \varrho_1 h_1 \partial_{\boldsymbol{x}}^{(1)} \cdot \boldsymbol{P}_{BE} + \boldsymbol{P}_{BE} \cdot \partial_{\boldsymbol{x}} \varrho_1 h_1, \tag{3.9}$$

which can be used to evaluate the terms in $\boldsymbol{C}$ when required. Similar identities hold for the BE tensors in the energy balances below.

Comparing the momentum balances in (3.4) to those derived by Zhang *et al.* (2006), we see that the interaction force densities, denoted by $n^{(i)}\overline{\boldsymbol{f}^{(ij)}}$, have the following definitions for hard-sphere collisions:

$$\left.\begin{aligned} n^{(1)}\overline{\boldsymbol{f}^{(11)}} &= \partial_{\boldsymbol{x}} \cdot \varphi_1 \boldsymbol{\sigma}^{(11)} = -\partial_{\boldsymbol{x}} \cdot \boldsymbol{P}_1, \quad & n^{(1)}\overline{\boldsymbol{f}^{(12)}} &= -\partial_{\boldsymbol{x}} \cdot \boldsymbol{P}_{12} + \boldsymbol{C} - K\boldsymbol{u}_{12}, \\ n^{(2)}\overline{\boldsymbol{f}^{(22)}} &= \partial_{\boldsymbol{x}} \cdot \varphi_2 \boldsymbol{\sigma}^{(22)} = -\partial_{\boldsymbol{x}} \cdot \boldsymbol{P}_2, \quad & n^{(2)}\overline{\boldsymbol{f}^{(21)}} &= -\partial_{\boldsymbol{x}} \cdot \boldsymbol{P}_{21} - \boldsymbol{C} + K\boldsymbol{u}_{12}. \end{aligned}\right\} \tag{3.10}$$

The intraphase stress tensors $\boldsymbol{\sigma}^{(ii)}$ are thus related to the like-particle pressure tensors $\boldsymbol{P}_i$, while the interphase stress tensors can be expressed as $\boldsymbol{\sigma}^{(ij)} = -\varphi_j(\rho_2\mu_1 + \rho_1\mu_2)\frac{1}{5}\mathcal{V}_{12}g_{12}\boldsymbol{P}_{BE}$ where $\varphi_i\boldsymbol{\sigma}^{(ij)} = \varphi_j\boldsymbol{\sigma}^{(ji)}$ (Zhang *et al.* 2006). As discussed in Zhang *et al.* (2006), the sum of the interspecies force densities is not equal to zero because they are calculated for different particle configurations, thereby giving rise to the interspecies stress tensor. For hard-sphere collisions of finite-size particles, this stress is proportional to $\boldsymbol{P}_{BE}$.

The momentum-exchange term in (3.8) produces the Archimedes force of phase 1 on phase 2 when $d_1 \ll d_2$ (i.e. $\mu_1 = 0$), as well as other contributions due to density and velocity gradients. As shown by Barajas *et al.* (1973), the mixture pressure contribution from unlike collisions ($\boldsymbol{P}_{12} + \boldsymbol{P}_{21}$) does not depend on y. However, as seen above, the phase pressure tensors do depend on the choice of y. Finally, it is remarkable that $\boldsymbol{P}_{BE}$ is always anisotropic due to the mean-slip velocity. Momentum-exchange terms involving gradients of the mean-slip-velocity kinetic energy are known to result in a hyperbolic system under certain conditions (see Syamlal 2011, in the context of a simpler two-fluid model).

3.3. *Energy tensor balances*

Neglecting the third-order central moments $\boldsymbol{Q}$, the balance equations for the total energy tensors $\varrho_\alpha\boldsymbol{E}_\alpha$ found from (2.1) are

$$\left.\begin{aligned} \partial_t\varrho_1\boldsymbol{E}_1 + \partial_{\boldsymbol{x}} \cdot (\boldsymbol{u}_1 \otimes \varrho_1\boldsymbol{E}_1 + (\varrho_1\boldsymbol{\sigma}_1 \otimes \boldsymbol{u}_1)^* + \boldsymbol{G}_1 + \boldsymbol{G}_{12}) &= \boldsymbol{D}_1 + \boldsymbol{D}_{0,12} + \boldsymbol{D}_{1,12}, \\ \partial_t\varrho_2\boldsymbol{E}_2 + \partial_{\boldsymbol{x}} \cdot (\boldsymbol{u}_2 \otimes \varrho_2\boldsymbol{E}_2 + (\varrho_2\boldsymbol{\sigma}_2 \otimes \boldsymbol{u}_2)^* + \boldsymbol{G}_2 + \boldsymbol{G}_{21}) &= \boldsymbol{D}_2 + \boldsymbol{D}_{0,21} + \boldsymbol{D}_{1,21}, \end{aligned}\right\} \tag{3.11}$$

https://doi.org/10.1017/jfm.2019.608 Published online by Cambridge University Press

where $X^*_{ijk} := \frac{1}{2}(X_{ijk} + X_{ikj})$ for the third-order tensor $\boldsymbol{X}$ with component X_{ijk}. On the right-hand side of (3.11), the traceless isotropization terms, which result directly from the unclosed collision integral due to like collisions, are defined by

$$\boldsymbol{D}_\alpha := \frac{6g_0\varrho_\alpha\varphi_\alpha\sqrt{\Theta_\alpha}}{\sqrt{\pi}d_\alpha}(\Theta_\alpha\boldsymbol{I} - \boldsymbol{\sigma}_\alpha). \tag{3.12}$$

In the limit $d_1 \ll d_2$, $\boldsymbol{D}_1$ will drive $\boldsymbol{\sigma}_1$ towards isotropy despite the other anisotropic source terms, in which case it suffices to solve for the scalar energy E_1.

The exchange terms in (3.11) due to unlike collisions have two parts. The first part does not involve spatial gradients

$$\left.\begin{aligned}\boldsymbol{D}_{0,12} &:= K[\tfrac{1}{4}\mu_2(\Theta\boldsymbol{I} + \boldsymbol{\sigma}_1 + \boldsymbol{\sigma}_2 + \boldsymbol{u}_{12}\otimes\boldsymbol{u}_{12}) - \boldsymbol{\sigma}_1 - (\boldsymbol{u}_1\otimes\boldsymbol{u}_{12})^\dagger],\\ \boldsymbol{D}_{0,21} &:= K[\tfrac{1}{4}\mu_1(\Theta\boldsymbol{I} + \boldsymbol{\sigma}_1 + \boldsymbol{\sigma}_2 + \boldsymbol{u}_{12}\otimes\boldsymbol{u}_{12}) - \boldsymbol{\sigma}_2 + (\boldsymbol{u}_2\otimes\boldsymbol{u}_{12})^\dagger],\end{aligned}\right\} \tag{3.13}$$

where $\boldsymbol{X}^\dagger := \frac{1}{2}(\boldsymbol{X} + \boldsymbol{X}^\mathrm{t})$ is the symmetric second-order tensor formed from $\boldsymbol{X}$. Note that $\boldsymbol{D}_{0,12} + \boldsymbol{D}_{0,21} = \frac{1}{2}K(\Theta\boldsymbol{I} - \boldsymbol{\sigma}_1 - \boldsymbol{\sigma}_2 - \boldsymbol{u}_{12}\otimes\boldsymbol{u}_{12})$ has zero trace, and thus these terms do not alter the total energy of the system. Furthermore, they do not directly affect the hyperbolic nature of the two-fluid model.

As shown in appendix A, the third-order collisional flux tensors in (3.11) have the forms

$$\left.\begin{aligned}\boldsymbol{G}_1 &:= (\boldsymbol{P}_1\otimes\boldsymbol{u}_1)^*, \quad \boldsymbol{G}_2 := (\boldsymbol{P}_2\otimes\boldsymbol{u}_2)^*,\\ \boldsymbol{G}_{12} &:= \tfrac{1}{5}\mathcal{V}_{12}\mu_2\varrho_1\varphi_2 g_{12}\boldsymbol{G}_{BE,12}, \quad \boldsymbol{G}_{21} := \tfrac{1}{5}\mathcal{V}_{12}\mu_1\varrho_2\varphi_1 g_{12}\boldsymbol{G}_{BE,21},\end{aligned}\right\} \tag{3.14}$$

where the third-order tensors $\boldsymbol{G}_{BE}$ due to the BE contribution (given in table 1) are expressed exactly in terms of the velocity moments. As expected, the components of $\boldsymbol{G}_{BE}$ have the property $G_{BE,ijk} = G_{BE,ikj}$. In terms of these tensors, the gradient-dependent contributions to the energy-exchange terms are

$$\left.\begin{aligned}\boldsymbol{D}_{1,12} &:= \tfrac{1}{5}\mu_2\varphi_2(\partial_{\boldsymbol{x}} - \partial^{(2)}_{\boldsymbol{x}})\cdot\varrho_1 h_1\boldsymbol{G}_{BE,12} - \tfrac{1}{5}\mu_1\varphi_1(\partial_{\boldsymbol{x}} - \partial^{(1)}_{\boldsymbol{x}})\cdot\varrho_2 h_2\boldsymbol{G}_{BE,12},\\ \boldsymbol{D}_{1,21} &:= \tfrac{1}{5}\mu_2\varphi_2(\partial_{\boldsymbol{x}} - \partial^{(2)}_{\boldsymbol{x}})\cdot\varrho_1 h_1\boldsymbol{G}_{BE,21} - \tfrac{1}{5}\mu_1\varphi_1(\partial_{\boldsymbol{x}} - \partial^{(1)}_{\boldsymbol{x}})\cdot\varrho_2 h_2\boldsymbol{G}_{BE,21}.\end{aligned}\right\} \tag{3.15}$$

Using the definition of $\boldsymbol{G}_{BE}$, it can be shown that $\mathrm{tr}(\boldsymbol{D}_{1,12}) + \mathrm{tr}(\boldsymbol{D}_{1,21}) = 0$ so that the total energy of the system is conserved.

3.4. *Total energy balances*

Balances for the total energy in each phase, $\varrho_\alpha E_\alpha := \varrho_\alpha\mathrm{tr}(\boldsymbol{E}_\alpha)$, can be found by taking the trace of (3.11). This leads to

$$\left.\begin{aligned}\partial_t\varrho_1 E_1 + \partial_{\boldsymbol{x}}\cdot(\varrho_1\boldsymbol{u}_1 E_1 + \varrho_1\boldsymbol{\sigma}_1\cdot\boldsymbol{u}_1 + \boldsymbol{P}_1\cdot\boldsymbol{u}_1 + \boldsymbol{q}_{12}) &= C_E + D_E,\\ \partial_t\varrho_2 E_2 + \partial_{\boldsymbol{x}}\cdot(\varrho_2\boldsymbol{u}_2 E_2 + \varrho_2\boldsymbol{\sigma}_2\cdot\boldsymbol{u}_2 + \boldsymbol{P}_2\cdot\boldsymbol{u}_2 + \boldsymbol{q}_{21}) &= -C_E - D_E,\end{aligned}\right\} \tag{3.16}$$

where the drag exchange term is given by (as done for $\boldsymbol{q}_{BE}$ in table 1, we use the symmetric form for D_E)

$$D_E := \tfrac{1}{2}(\mathrm{tr}(\boldsymbol{D}_{0,12}) - \mathrm{tr}(\boldsymbol{D}_{0,21})) = \tfrac{3}{2}K[\mu_2\Theta_2 - \mu_1\Theta_1 - \tfrac{1}{3}(\mu_2\boldsymbol{u}_2 + \mu_1\boldsymbol{u}_1)\cdot\boldsymbol{u}_{12}], \tag{3.17}$$

https://doi.org/10.1017/jfm.2019.608 Published online by Cambridge University Press

$$\boldsymbol{G}_{BE,12} = \langle \boldsymbol{g}\otimes\boldsymbol{g}\otimes\boldsymbol{v}\rangle_1 + \tfrac{1}{2}(\boldsymbol{I}\otimes\langle g^2\boldsymbol{v}\rangle_1)^* - \tfrac{3}{14}\mu_2(\langle \boldsymbol{g}\otimes\boldsymbol{g}\otimes\boldsymbol{g}\rangle + (\boldsymbol{I}\otimes\langle g^2\boldsymbol{g}\rangle)^\diamond)$$

$$\boldsymbol{G}_{BE,21} = \langle \boldsymbol{g}\otimes\boldsymbol{g}\otimes\boldsymbol{v}\rangle_2 + \tfrac{1}{2}(\boldsymbol{I}\otimes\langle g^2\boldsymbol{v}\rangle_2)^* + \tfrac{3}{14}\mu_1(\langle \boldsymbol{g}\otimes\boldsymbol{g}\otimes\boldsymbol{g}\rangle + (\boldsymbol{I}\otimes\langle g^2\boldsymbol{g}\rangle)^\diamond)$$

$$\boldsymbol{q}_{BE,12} = \langle(\boldsymbol{g}\cdot\boldsymbol{v})\boldsymbol{g}\rangle_1 + \tfrac{1}{2}\langle g^2\boldsymbol{v}\rangle_1 - \tfrac{3}{4}\mu_2\langle g^2\boldsymbol{g}\rangle$$

$$\boldsymbol{q}_{BE,21} = \langle(\boldsymbol{g}\cdot\boldsymbol{v})\boldsymbol{g}\rangle_2 + \tfrac{1}{2}\langle g^2\boldsymbol{v}\rangle_2 + \tfrac{3}{4}\mu_1\langle g^2\boldsymbol{g}\rangle$$

$$\boldsymbol{q}_{BE} = \tfrac{1}{2}[\langle(\boldsymbol{g}\cdot\boldsymbol{v})\boldsymbol{g}\rangle_1 + \langle(\boldsymbol{g}\cdot\boldsymbol{v})\boldsymbol{g}\rangle_2 + \tfrac{1}{2}(\langle g^2\boldsymbol{v}\rangle_1 + \langle g^2\boldsymbol{v}\rangle_2) + \tfrac{3}{4}(\mu_1-\mu_2)\langle g^2\boldsymbol{g}\rangle]$$

where $(\boldsymbol{I}\otimes\boldsymbol{g})^\diamond$ has components $(\delta_{ij}g_k)^\diamond = (\delta_{ij}g_k)^* + \tfrac{1}{2}\delta_{jk}g_i$ and

$$\langle g^2\boldsymbol{v}\rangle_1 = 2\boldsymbol{\sigma}_1\cdot\boldsymbol{u}_{12} + (3\Theta_1 + 3\Theta_2 + |\boldsymbol{u}_{12}|^2)\boldsymbol{u}_1$$

$$\langle g^2\boldsymbol{v}\rangle_2 = 2\boldsymbol{\sigma}_2\cdot\boldsymbol{u}_{21} + (3\Theta_1 + 3\Theta_2 + |\boldsymbol{u}_{12}|^2)\boldsymbol{u}_2$$

$$\langle g^2\boldsymbol{g}\rangle = 2(\boldsymbol{\sigma}_1+\boldsymbol{\sigma}_2)\cdot\boldsymbol{u}_{12} + (3\Theta_1 + 3\Theta_2 + |\boldsymbol{u}_{12}|^2)\boldsymbol{u}_{12}$$

$$\langle(\boldsymbol{g}\cdot\boldsymbol{v})\boldsymbol{g}\rangle_1 = (3\Theta_1\boldsymbol{I}+\boldsymbol{\sigma}_1)\cdot\boldsymbol{u}_{12} + (\boldsymbol{\sigma}_1+\boldsymbol{\sigma}_2+\boldsymbol{u}_{12}\otimes\boldsymbol{u}_{12})\cdot\boldsymbol{u}_1$$

$$\langle(\boldsymbol{g}\cdot\boldsymbol{v})\boldsymbol{g}\rangle_2 = (3\Theta_2\boldsymbol{I}+\boldsymbol{\sigma}_2)\cdot\boldsymbol{u}_{21} + (\boldsymbol{\sigma}_1+\boldsymbol{\sigma}_2+\boldsymbol{u}_{12}\otimes\boldsymbol{u}_{12})\cdot\boldsymbol{u}_2$$

$$\langle \boldsymbol{g}\otimes\boldsymbol{g}\otimes\boldsymbol{v}\rangle_1 = \boldsymbol{u}_{12}\otimes\boldsymbol{\sigma}_1 + (\boldsymbol{\sigma}_1\otimes\boldsymbol{u}_{12})^* + ((\boldsymbol{\sigma}_1+\boldsymbol{\sigma}_2)\otimes\boldsymbol{u}_1)^* + \boldsymbol{u}_{12}\otimes(\boldsymbol{u}_{12}\otimes\boldsymbol{u}_1)^\dagger$$

$$\langle \boldsymbol{g}\otimes\boldsymbol{g}\otimes\boldsymbol{v}\rangle_2 = \boldsymbol{u}_{21}\otimes\boldsymbol{\sigma}_2 + (\boldsymbol{\sigma}_2\otimes\boldsymbol{u}_{21})^* + ((\boldsymbol{\sigma}_1+\boldsymbol{\sigma}_2)\otimes\boldsymbol{u}_2)^* + \boldsymbol{u}_{21}\otimes(\boldsymbol{u}_{21}\otimes\boldsymbol{u}_2)^\dagger$$

$$\langle \boldsymbol{g}\otimes\boldsymbol{g}\otimes\boldsymbol{g}\rangle = \boldsymbol{u}_{12}\otimes(\boldsymbol{\sigma}_1+\boldsymbol{\sigma}_2) + 2((\boldsymbol{\sigma}_1+\boldsymbol{\sigma}_2)\otimes\boldsymbol{u}_{12})^* + \boldsymbol{u}_{12}\otimes\boldsymbol{u}_{12}\otimes\boldsymbol{u}_{12}$$

TABLE 1. Third-order tensors $\boldsymbol{G}_{BE}$ and contracted first-order tensor $\boldsymbol{q}_{BE}$ appearing in the energy conservation equations. In these expressions, the vectors $\boldsymbol{u}_1$, $\boldsymbol{u}_2$, $\boldsymbol{u}_{12}$ and $\boldsymbol{u}_{21} = -\boldsymbol{u}_{12}$, and the velocity covariance tensors $\boldsymbol{\sigma}_1$ and $\boldsymbol{\sigma}_2$ appear. For isotropic systems, $\boldsymbol{\sigma}_\alpha = \Theta_\alpha\boldsymbol{I}$ and the formulae simplify considerably. The third-order tensors have the symmetry property $G_{ijk} = G_{ikj}$. Using these definitions and $\mu_1+\mu_2 = 2$, it is straightforward to prove that $\boldsymbol{q}_{BE,12} = \boldsymbol{q}_{BE,21}$. Thus, we define $\boldsymbol{q}_{BE} := \tfrac{1}{2}(\boldsymbol{q}_{BE,12} + \boldsymbol{q}_{BE,21})$. As a corollary, $\boldsymbol{G}_{BE,12} - \boldsymbol{G}_{BE,21} = \tfrac{1}{14}[8\langle \boldsymbol{g}\otimes\boldsymbol{g}\otimes\boldsymbol{g}\rangle + (\boldsymbol{I}\otimes\langle g^2\boldsymbol{g}\rangle)^* - 3\langle g^2\boldsymbol{g}\rangle\otimes\boldsymbol{I}]$ and contraction of the difference is null. Finally, note that $\langle g^2\boldsymbol{g}\rangle + |\boldsymbol{u}_{12}|^2\boldsymbol{u}_{21}$ is proportional to $\boldsymbol{P}_{BE}\cdot\boldsymbol{u}_{12}$, which can be used to re-express $\boldsymbol{q}_{BE}$ with terms involving $\boldsymbol{P}_{BE}$.

and the energy fluxes by

$$\boldsymbol{q}_{12} := \tfrac{1}{5}\mathcal{V}_{12}\mu_2\varrho_1\varphi_2 g_{12}\boldsymbol{q}_{BE}, \quad \boldsymbol{q}_{21} := \tfrac{1}{5}\mathcal{V}_{12}\mu_1\varrho_2\varphi_1 g_{12}\boldsymbol{q}_{BE}. \tag{3.18a,b}$$

The BE collisional correction to the energy flux $\boldsymbol{q}_{BE}$ has components $q_{BE,i} := \sum_j G_{BE,ijj}$ (see table 1). The total-energy-exchange term is given by

$$C_E := \mathrm{tr}(\boldsymbol{D}_{1,12}) = \tfrac{1}{5}\mu_2\varphi_2(\partial_{\boldsymbol{x}} - \partial_{\boldsymbol{x}}^{(2)})\cdot\varrho_1 h_1\boldsymbol{q}_{BE} - \tfrac{1}{5}\mu_1\varphi_1(\partial_{\boldsymbol{x}} - \partial_{\boldsymbol{x}}^{(1)})\cdot\varrho_2 h_2\boldsymbol{q}_{BE}. \tag{3.19}$$

Thus, we can observe that the system total energy $\varrho E := \varrho_1 E_1 + \varrho_2 E_2$ is a conserved quantity. It is worth noting the important contribution of the relative velocity $\boldsymbol{u}_{12}$ in the production and exchange of energy between the two phases. At equilibrium, the mass ratios μ_α determine the energy distribution between the two phases.

3.5. *Covariance tensors and fluctuating energy*

Balance equations for the covariance tensors can be derived by subtracting off the contributions from the mean kinetic energy tensor $\varrho_\alpha\boldsymbol{K}_\alpha := \tfrac{1}{2}\varrho_\alpha\boldsymbol{u}_\alpha\otimes\boldsymbol{u}_\alpha$ in (3.11). First, starting from the mean momentum balances, we derive balances for the mean kinetic

https://doi.org/10.1017/jfm.2019.608 Published online by Cambridge University Press

energy tensors

$$\left.\begin{aligned}&\partial_t \varrho_1 \boldsymbol{K}_1 + \partial_{\boldsymbol{x}} \cdot \varrho_1 \boldsymbol{u}_1 \otimes \boldsymbol{K}_1 + (\boldsymbol{u}_1 \otimes \partial_{\boldsymbol{x}} \cdot (\varrho_1 \boldsymbol{\sigma}_1 + \boldsymbol{P}_1 + \boldsymbol{P}_{12}))^\dagger \\ &\quad = (\boldsymbol{u}_1 \otimes \boldsymbol{C} - K \boldsymbol{u}_1 \otimes \boldsymbol{u}_{12})^\dagger, \\ &\partial_t \varrho_p \boldsymbol{K}_2 + \partial_{\boldsymbol{x}} \cdot \varrho_2 \boldsymbol{u}_2 \otimes \boldsymbol{K}_2 + (\boldsymbol{u}_2 \otimes \partial_{\boldsymbol{x}} \cdot (\varrho_2 \boldsymbol{\sigma}_2 + \boldsymbol{P}_2 + \boldsymbol{P}_{21}))^\dagger \\ &\quad = -(\boldsymbol{u}_2 \otimes \boldsymbol{C} - K \boldsymbol{u}_2 \otimes \boldsymbol{u}_{12})^\dagger.\end{aligned}\right\} \tag{3.20}$$

We then subtract these expressions from the total energy tensor balances to find

$$\left.\begin{aligned}&\tfrac{1}{2}\partial_t \varrho_1 \boldsymbol{\sigma}_1 + \tfrac{1}{2}\partial_{\boldsymbol{x}} \cdot \varrho_1 \boldsymbol{u}_1 \otimes \boldsymbol{\sigma}_1 + ((\varrho_1 \boldsymbol{\sigma}_1 + \boldsymbol{P}_1) \cdot \partial_{\boldsymbol{x}} \boldsymbol{u}_1)^\dagger + \partial_{\boldsymbol{x}} \cdot \boldsymbol{G}_{12} - (\boldsymbol{u}_1 \otimes \partial_{\boldsymbol{x}} \cdot \boldsymbol{P}_{12})^\dagger \\ &\quad = \boldsymbol{D}_1 + \boldsymbol{D}_{0,12} + K(\boldsymbol{u}_1 \otimes \boldsymbol{u}_{12})^\dagger + \boldsymbol{D}_{1,12} - (\boldsymbol{u}_1 \otimes \boldsymbol{C})^\dagger, \\ &\tfrac{1}{2}\partial_t \varrho_2 \boldsymbol{\sigma}_2 + \tfrac{1}{2}\partial_{\boldsymbol{x}} \cdot \varrho_2 \boldsymbol{u}_2 \otimes \boldsymbol{\sigma}_2 + ((\varrho_2 \boldsymbol{\sigma}_2 + \boldsymbol{P}_2) \cdot \partial_{\boldsymbol{x}} \boldsymbol{u}_2)^\dagger + \partial_{\boldsymbol{x}} \cdot \boldsymbol{G}_{21} - (\boldsymbol{u}_2 \otimes \partial_{\boldsymbol{x}} \cdot \boldsymbol{P}_{21})^\dagger \\ &\quad = \boldsymbol{D}_2 + \boldsymbol{D}_{0,21} - K(\boldsymbol{u}_2 \otimes \boldsymbol{u}_{12})^\dagger + \boldsymbol{D}_{1,21} + (\boldsymbol{u}_2 \otimes \boldsymbol{C})^\dagger.\end{aligned}\right\} \tag{3.21}$$

The velocity covariance tensors will be non-zero if there is a non-zero mean-slip velocity. Also, in general, they will be anisotropic due to the anisotropy of their source terms.

The traces of the velocity covariance tensors in (3.21) lead to the fluctuating energy balance equations

$$\left.\begin{aligned}&\tfrac{3}{2}\partial_t \varrho_1 \Theta_1 + \tfrac{3}{2}\partial_{\boldsymbol{x}} \cdot \varrho_1 \boldsymbol{u}_1 \Theta_1 + (\varrho_1 \boldsymbol{\sigma}_1 + \boldsymbol{P}_1) : \partial_{\boldsymbol{x}} \boldsymbol{u}_1 + \partial_{\boldsymbol{x}} \cdot \boldsymbol{q}_{12} - \boldsymbol{u}_1 \cdot (\partial_{\boldsymbol{x}} \cdot \boldsymbol{P}_{12}) \\ &\quad = D_E + K \boldsymbol{u}_1 \cdot \boldsymbol{u}_{12} + C_E - \boldsymbol{u}_1 \cdot \boldsymbol{C}, \\ &\tfrac{3}{2}\partial_t \varrho_2 \Theta_2 + \tfrac{3}{2}\partial_{\boldsymbol{x}} \cdot \varrho_2 \boldsymbol{u}_2 \Theta_2 + (\varrho_2 \boldsymbol{\sigma}_2 + \boldsymbol{P}_2) : \partial_{\boldsymbol{x}} \boldsymbol{u}_2 + \partial_{\boldsymbol{x}} \cdot \boldsymbol{q}_{21} - \boldsymbol{u}_2 \cdot (\partial_{\boldsymbol{x}} \cdot \boldsymbol{P}_{21}) \\ &\quad = -D_E - K \boldsymbol{u}_2 \cdot \boldsymbol{u}_{12} - C_E + \boldsymbol{u}_2 \cdot \boldsymbol{C},\end{aligned}\right\} \tag{3.22}$$

which govern the phase temperatures. The terms on the left-hand sides involving the phase pressure tensors correspond to compression heating. The other terms on the right-hand side are production/redistribution of fluctuating energy between phases. The sum of the two balances in (3.22) is the total fluctuating energy. For the latter, we can observe that there is a source term $K|\boldsymbol{u}_{12}|^2$ due to the transfer of mean kinetic energy to fluctuations when the phases have a mean-slip velocity. On the other hand, $\boldsymbol{u}_{21} \cdot \boldsymbol{C}$ can function as a source or sink of fluctuating energy depending on the signs of the gradients appearing in $\boldsymbol{C}$. These observations imply that even in the absence of mean gradients, the phase temperatures will be non-zero if the phases are initially in relative mean motion. Finally, using the momentum balances in (3.4) and (3.22), it is possible to derive the balance equation for the 'mixture' temperature Θ.

3.6. *Equilibrium state*

The equilibrium state for a homogeneous, binary system is $\boldsymbol{u}_1 = \boldsymbol{u}_2$, $\mu_1 \Theta_1 = \mu_2 \Theta_2$ and $\boldsymbol{\sigma}_\alpha = \Theta_\alpha \boldsymbol{I}$ (see, e.g. Kolodner 1957; Grad 1960; Morse 1963; Goldman & Sirovich 1967), and the densities, velocities and temperatures are spatially uniform. The functions h_1 and h_2 introduced in (2.6) are chosen such that the isotropic flux pressure, i.e. for type-1 particles

$$\varrho_1 \boldsymbol{\sigma}_1 + \boldsymbol{P}_1 + \boldsymbol{P}_{12} = \varrho_1 \Theta_1 (1 + \mathcal{V}_{11} \varphi_1 g_0 + \mathcal{V}_{12} \varphi_2 g_{12}) \boldsymbol{I} = p_1 \boldsymbol{I}, \tag{3.23}$$

https://doi.org/10.1017/jfm.2019.608 Published online by Cambridge University Press

and the buoyancy pressure, defined to be the non-zero term in $\boldsymbol{C}$ at equilibrium, i.e. for type-1 particles (the other terms in $\boldsymbol{C}$ depend on gradients in density and velocity and correspond to forces other than the buoyancy force)

$$\tfrac{1}{5}\mu_2\varrho_1 h_1 \boldsymbol{P}_{BE}|_{eq} = \varrho_1\Theta_1 h_1 \boldsymbol{I} = p_1\boldsymbol{I}, \tag{3.24}$$

are identical for each particle type. In equilibrium, the phase pressures are isotropic and the momentum balances reduce to

$$\partial_{\boldsymbol{x}} p_1 = \varphi_2\partial_{\boldsymbol{x}} p_1 - \varphi_1\partial_{\boldsymbol{x}} p_2, \quad \partial_{\boldsymbol{x}} p_2 = \varphi_1\partial_{\boldsymbol{x}} p_2 - \varphi_2\partial_{\boldsymbol{x}} p_1. \tag{3.25a,b}$$

Thus, $\partial_{\boldsymbol{x}}(p_1 + p_2) = \boldsymbol{0}$, i.e. the mixture pressure is uniform, and hence $\partial_{\boldsymbol{x}} p_1 = -\partial_{\boldsymbol{x}} p_2$. It then follows that in order for the above momentum balances to hold, $\partial_{\boldsymbol{x}} p_\alpha = \boldsymbol{0}$ at equilibrium, i.e. the phase pressures must be uniform.

If the mean momentum is initially null, $\varrho_1\boldsymbol{u}_1 + \varrho_2\boldsymbol{u}_2 = \boldsymbol{0}$ but $\boldsymbol{u}_1 \neq \boldsymbol{u}_2$, then at equilibrium $\boldsymbol{u}_1 = \boldsymbol{u}_2 = \boldsymbol{0}$ and the mean kinetic energy will be transferred to Θ_α through collisions. Thus, in the limit where $\mu_1 \ll \mu_2$, the phase temperatures will be very different at equilibrium with $\Theta_2 \ll \Theta_1$. (For systems in motion, Θ_2 has a source term due to phase compression and, hence, can be much larger than its equilibrium value. For fluid–particle systems in § 4, the equilibrium value of Θ_2 is essentially zero.) As the particles are assumed to have no internal degrees of freedom, their internal energies are null. In the absence of external forces (e.g. gravity), the mean momentum and total energy of the system are conserved. As first described by Grad (1960), the rates of relaxation to equilibrium for the mean velocities and granular temperatures can be very different for components with disparate masses. For example, under certain conditions (e.g. plasmas) the mean velocities will rapidly equilibrate so that only the two temperatures differ (i.e. the so-called two-temperature model (Sirovich 1962)). Hereinafter, we will focus on cases for which a two-fluid description is required, i.e. the heavy component is a trace component with very small molar concentration as first described in Hamel (1966).

4. The fluid–particle limit

The balances derived in the previous section hold for any binary, non-dissipative, hard-sphere mixture. We now want to consider the case where $d_1 \ll d_2$ and $\mu_1 \ll \mu_2$, which corresponds to phase 1 being a molecular hard-sphere fluid and phase 2 composed of macroscopic particles. (See Zhang *et al.* (2006) for a discussion of this limit for arbitrary binary interaction forces.) Furthermore, we will assume that the VDFs are Maxwellian, i.e. $\boldsymbol{\sigma}_\alpha = \Theta_\alpha\boldsymbol{I}$. This assumption decreases significantly the number of variables in the two-fluid model (Levermore & Morokoff 1996). However, with finite-size (type-2) particles, it is more accurate to solve for $\boldsymbol{\sigma}_2$ using the anisotropic Gaussian model (Levermore & Morokoff 1996; Vié *et al.* 2015; Kong *et al.* 2017; Patel *et al.* 2017). By definition, the volume fraction occupied by type-α particles is $\varphi_\alpha = \varrho_\alpha/\rho_\alpha$, and the total occupied volume fraction is $\varphi = \varphi_1 + \varphi_2$. Thus, when φ_1 is negligibly small relative to φ_2, the fluid phase will be a perfect gas and terms involving $\varrho_1\varphi_1$ can be dropped. Otherwise, the fluid phase will be a non-ideal gas (i.e. a hard-sphere fluid). In terms of the mole fractions, that of phase 2 is negligible because the number of type-1 particles is allowed to go to infinity as d_1 goes to zero such that φ_1 remains constant. Thus, type-2 particles are a trace component in the sense of Hamel (1966). Finally, the Maxwellian assumption for the fluid phase implies that the fluid is inviscid and hence governed by the Euler equation in the absence of particles.

https://doi.org/10.1017/jfm.2019.608 Published online by Cambridge University Press

Mass balances

$$\partial_t \varrho_1 + \partial_{\boldsymbol{x}} \cdot \varrho_1 \boldsymbol{u}_1 = 0$$
$$\partial_t \varrho_2 + \partial_{\boldsymbol{x}} \cdot \varrho_2 \boldsymbol{u}_2 = 0$$

Momentum balances

$$\varrho_1(\partial_t + \boldsymbol{u}_1 \cdot \partial_{\boldsymbol{x}})\boldsymbol{u}_1 + \partial_{\boldsymbol{x}} \varrho_1 \Theta_1 (1 + 4\varphi_1 g_0) + \partial_{\boldsymbol{x}} \cdot \varphi_2 \varrho_1 g_{12} \boldsymbol{P}^*_{BE} =$$
$$\varphi_2(\partial_{\boldsymbol{x}} - \partial^{(2)}_{\boldsymbol{x}}) \cdot \varrho_1 h_1 \boldsymbol{P}^*_{BE} - K\boldsymbol{u}_{12}$$
$$\varrho_2(\partial_t + \boldsymbol{u}_2 \cdot \partial_{\boldsymbol{x}})\boldsymbol{u}_2 + \partial_{\boldsymbol{x}} \varrho_2 \Theta_2 (1 + 4\varphi_2 g_0) = -\varphi_2(\partial_{\boldsymbol{x}} - \partial^{(2)}_{\boldsymbol{x}}) \cdot \varrho_1 h_1 \boldsymbol{P}^*_{BE} + K\boldsymbol{u}_{12}$$

Total energy balances

$$\varrho_1(\partial_t + \boldsymbol{u}_1 \cdot \partial_{\boldsymbol{x}})E_1 + \partial_{\boldsymbol{x}} \cdot \varrho_1 \Theta_1 (1 + 4\varphi_1 g_0)\boldsymbol{u}_1 + \partial_{\boldsymbol{x}} \cdot \varphi_2 \varrho_1 g_{12} \boldsymbol{q}^*_{BE} =$$
$$\varphi_2(\partial_{\boldsymbol{x}} - \partial^{(2)}_{\boldsymbol{x}}) \cdot \varrho_1 h_1 \boldsymbol{q}^*_{BE} + D_E$$
$$\varrho_2(\partial_t + \boldsymbol{u}_2 \cdot \partial_{\boldsymbol{x}})E_2 + \partial_{\boldsymbol{x}} \cdot \varrho_2 \Theta_2 (1 + 4\varphi_2 g_0)\boldsymbol{u}_2 = -\varphi_2(\partial_{\boldsymbol{x}} - \partial^{(2)}_{\boldsymbol{x}}) \cdot \varrho_1 h_1 \boldsymbol{q}^*_{BE} - D_E$$

where

$$\boldsymbol{P}^*_{BE} = (\Theta_1 + \Theta_2 + \tfrac{1}{5}|\boldsymbol{u}_{12}|^2)\boldsymbol{I} + \tfrac{2}{5}\boldsymbol{u}_{12} \otimes \boldsymbol{u}_{12} \quad \boldsymbol{q}^*_{BE} = \boldsymbol{P}^*_{BE} \cdot \boldsymbol{u}_2 + 2\Theta_2 \boldsymbol{u}_{21}$$
$$(\partial_{\boldsymbol{x}} - \partial^{(2)}_{\boldsymbol{x}}) \cdot \varrho_1 h_1 \boldsymbol{P}^*_{BE} = \boldsymbol{P}^*_{BE} \cdot \partial_{\boldsymbol{x}} \varrho_1 h_1 + \varrho_1 h_1 (\partial_{\boldsymbol{x}} \Theta_1 + \tfrac{2}{5}\boldsymbol{u}_{12} \cdot \partial_{\boldsymbol{x}} \boldsymbol{u}_1 + \tfrac{4}{5}(\partial_{\boldsymbol{x}} \cdot \boldsymbol{u}_1)\boldsymbol{u}_{12})$$
$$(\partial_{\boldsymbol{x}} - \partial^{(2)}_{\boldsymbol{x}}) \cdot \varrho_1 h_1 \boldsymbol{q}^*_{BE} = [(\partial_{\boldsymbol{x}} - \partial^{(2)}_{\boldsymbol{x}}) \cdot \varrho_1 h_1 \boldsymbol{P}^*_{BE}] \cdot \boldsymbol{u}_2 - 2\varrho_1 h_1 \Theta_2 \partial_{\boldsymbol{x}} \cdot \boldsymbol{u}_1$$
$$D_E = K(3\Theta_2 + \boldsymbol{u}_2 \cdot \boldsymbol{u}_{21}) \quad h_1 = g_{12} + (4g_0 - g_{12})\varphi_1 \quad g_{12} = \frac{1}{1-\varphi} \quad g_0 = \frac{2-\varphi}{2(1-\varphi)^3}$$

TABLE 2. Fluid–particle model for a binary, hard-sphere mixture with independent variables $(\varrho_\alpha, \boldsymbol{u}_\alpha, E_\alpha)$. The operator $(\partial_{\boldsymbol{x}} - \partial^{(2)}_{\boldsymbol{x}})$ produces gradients of the variables $(\varrho_1, \boldsymbol{u}_1, E_1, \varrho_2)$, i.e. $(\partial_{\boldsymbol{x}} - \partial^{(2)}_{\boldsymbol{x}}) \cdot \boldsymbol{u}_2 = 0$ and $(\partial_{\boldsymbol{x}} - \partial^{(2)}_{\boldsymbol{x}})E_2 = 0$. In this two-fluid model, the material densities ρ_1 and ρ_2 are constant and the volume fractions φ_α are found from $\varrho_\alpha = \rho_\alpha \varphi_\alpha$. The other variables appearing in the model are $\varphi = \varphi_1 + \varphi_2$, $\boldsymbol{u}_{12} = -\boldsymbol{u}_{21} = \boldsymbol{u}_1 - \boldsymbol{u}_2$, and $\Theta_\alpha = \frac{2}{3}(E_\alpha - \frac{1}{2}|\boldsymbol{u}_\alpha|^2)$. Note that $\boldsymbol{P}^*_{BE} := \frac{2}{5}\boldsymbol{P}_{BE}$ and $\boldsymbol{q}^*_{BE} := \frac{2}{5}\boldsymbol{q}_{BE}$. For a perfect gas, $\varrho_1 = \rho_1 \varphi_1 = \rho_f(1 - \varphi_2)$ is finite in the limit $\varphi_1 \to 0$ with fluid density ρ_f and void fraction $\alpha_f := 1 - \varphi_2$, in which case $p_f := \rho_f \Theta_1$ is the fluid pressure.

In the fluid limit where $d_1 \ll d_2$, the parameters appearing in the balance equations can be approximated as follows:

$$\left.\begin{aligned} \mathcal{V}_{12} = 1, \quad g_{12} = \frac{1}{1-\varphi}, \; \mu_1 = 0, \; \mu_2 = 2, \quad K = \frac{6\varrho_1 \varphi_2 \sqrt{\Theta/2}}{d_2(1-\varphi)}, \\ h_1 = \frac{1-\varphi_1}{1-\varphi} + 4\varphi_1 g_0, \quad h_2 = \frac{1-\varphi_2}{1-\varphi} + 4\varphi_2 g_0. \end{aligned}\right\} \tag{4.1}$$

The parameters, ρ_1, ρ_2 and d_2 are constants. The fluid–particle model solves for state variables: $(\varrho_1, \varrho_2, \boldsymbol{u}_1, \boldsymbol{u}_2, E_1, E_2)$. For completeness, we provide the complete three-dimensional (3-D) two-fluid model written in these variables in table 2. In § 5, we investigate the hyperbolicity of the one-dimensional (1-D) model for various sets of parameters, including for a perfect gas. For clarity, in the remainder of this section, we will consider only the case where the fluid is a perfect gas. This corresponds to neglecting φ_1 and replacing $\varrho_1 = \rho_f \alpha_f$ and $\varrho_2 = \rho_p \alpha_p$. By definition, $\alpha_f := 1 - \alpha_p$ and $\alpha_p := \varphi_2$, and $\alpha_f g_{12} = \alpha_f h_1 = 1$. The fluid pressure is then defined as $p_f = \rho_f \Theta_f$ and $p_p = \rho_p \alpha_p \Theta_p (1 + 4\alpha_p g_0)$ is the granular pressure. In general, the subscript $_f$ denotes type-1 particles and $_p$ denotes type-2 particles.

https://doi.org/10.1017/jfm.2019.608 Published online by Cambridge University Press

Mass balances

$$\partial_t \rho_f \alpha_f + \partial_{\boldsymbol{x}} \cdot \rho_f \alpha_f \boldsymbol{u}_f = 0$$

$$\partial_t \rho_p \alpha_p + \partial_{\boldsymbol{x}} \cdot \rho_p \alpha_p \boldsymbol{u}_p = 0$$

Momentum balances

$$\rho_f \alpha_f (\partial_t + \boldsymbol{u}_f \cdot \partial_{\boldsymbol{x}}) \boldsymbol{u}_f + \partial_{\boldsymbol{x}} \cdot (\alpha_p \rho_f \boldsymbol{R}) + \alpha_f \partial_{\boldsymbol{x}} p_f = \boldsymbol{F}_{pf} + K \boldsymbol{u}_{pf} + \rho_f \alpha_f \boldsymbol{g}$$

$$\rho_p \alpha_p (\partial_t + \boldsymbol{u}_p \cdot \partial_{\boldsymbol{x}}) \boldsymbol{u}_p + \partial_{\boldsymbol{x}} p_p + \alpha_p \partial_{\boldsymbol{x}} p_f = \boldsymbol{F}_{fp} + K \boldsymbol{u}_{fp} + \rho_p \alpha_p \boldsymbol{g}$$

Total energy balances

$$\rho_f \alpha_f (\partial_t + \boldsymbol{u}_f \cdot \partial_{\boldsymbol{x}}) E_f + \partial_{\boldsymbol{x}} \cdot (\alpha_f p_f \boldsymbol{u}_f + \alpha_p \rho_f \boldsymbol{r}) + p_f \partial_{\boldsymbol{x}} \cdot (\alpha_p \boldsymbol{u}_p) = D_{pf} + D_E + \rho_f \alpha_f \boldsymbol{g} \cdot \boldsymbol{u}_f$$

$$\rho_p \alpha_p (\partial_t + \boldsymbol{u}_p \cdot \partial_{\boldsymbol{x}}) E_p + \partial_{\boldsymbol{x}} \cdot (p_p \boldsymbol{u}_p) + \alpha_p \boldsymbol{u}_p \cdot \partial_{\boldsymbol{x}} p_f = D_{fp} - D_E + \rho_p \alpha_p \boldsymbol{g} \cdot \boldsymbol{u}_p$$

where $\alpha_f + \alpha_p = 1$,

$$\boldsymbol{R} = (\Theta_p + \tfrac{1}{5}|\boldsymbol{u}_{fp}|^2)\boldsymbol{I} + \tfrac{2}{5}\boldsymbol{u}_{fp} \otimes \boldsymbol{u}_{fp} \quad \boldsymbol{r} = \boldsymbol{R} \cdot \boldsymbol{u}_p + 2\Theta_p \boldsymbol{u}_{pf}$$

$$\boldsymbol{F}_{pf} = -\boldsymbol{F}_{fp} = \alpha_p \boldsymbol{R} \cdot \partial_{\boldsymbol{x}} \rho_f + \tfrac{2}{3}\alpha_p \rho_f (\partial_{\boldsymbol{x}} \cdot \boldsymbol{u}_f) \boldsymbol{u}_{fp} + \tfrac{4}{5}\alpha_p \rho_f \boldsymbol{S} \cdot \boldsymbol{u}_{fp}$$

$$D_{pf} = -D_{fp} = \boldsymbol{u}_p \cdot \boldsymbol{F}_{pf} + 2\alpha_p \Theta_p (\boldsymbol{u}_{pf} \cdot \partial_{\boldsymbol{x}} \rho_f - \rho_f \, \partial_{\boldsymbol{x}} \cdot \boldsymbol{u}_f) \quad D_E = K(3\Theta_p + \boldsymbol{u}_p \cdot \boldsymbol{u}_{pf})$$

$$\boldsymbol{\Gamma} = \tfrac{1}{2}[\partial_{\boldsymbol{x}} \otimes \boldsymbol{u}_f + (\partial_{\boldsymbol{x}} \otimes \boldsymbol{u}_f)^{\mathrm{t}}] \quad \boldsymbol{S} = \boldsymbol{\Gamma} - \tfrac{1}{3}\mathrm{tr}(\boldsymbol{\Gamma})\boldsymbol{I}$$

$$\boldsymbol{u}_{fp} = -\boldsymbol{u}_{pf} = \boldsymbol{u}_f - \boldsymbol{u}_p \quad p_f = \rho_f \Theta_f \quad p_p = \rho_p \alpha_p \Theta_p (1 + 4\alpha_p g_0) \quad g_0 = \frac{1 + \alpha_f}{2\alpha_f^3}$$

$$\Theta_f = (\gamma_f - 1)(E_f - \tfrac{1}{2}|\boldsymbol{u}_f|^2) \quad \Theta_p = (\gamma_p - 1)(E_p - \tfrac{1}{2}|\boldsymbol{u}_p|^2)$$

TABLE 3. Compressible gas–particle two-fluid model for elastic hard-sphere particles in an ideal gas with $\rho_f \ll \rho_p$. The particle material density ρ_p is constant and the specific heat ratios are γ_f and $\gamma_p = 5/3$. The stress tensor $\boldsymbol{R}$, energy flux $\boldsymbol{r}$, momentum exchange $\boldsymbol{F}_{pf}$ and energy exchange D_{pf} arise due to the finite-size particles. For constant fluid density, only the term involving $\boldsymbol{S}$ is significant in $\boldsymbol{F}_{pf}$, providing a model for the lift force. K is the drag coefficient that depends on the particle Reynolds number, Mach number and volume fraction. The second term in $\boldsymbol{F}_{pf}$, resulting from fluid compressibility, can be combined with the drag force. The first term in $\boldsymbol{F}_{pf}$ has the form of a dispersion force, but resulting here from fluid-density gradients. A constant body force $\boldsymbol{g}$ is included for completeness (see appendix B).

For convenience, the model equations for the ideal-gas case are provided in table 3 and have the form employed in 'classical' two-fluid models for compressible gas–particle flows, albeit with additional terms due to fluid compressibility and fluid-velocity gradients arising from the BE tensors for finite-size particles. Note, as expected, that for $\alpha_p = 0$ the fluid phase reduces to the Euler equation of gas dynamics. The BE tensors depend on

$$(\partial_{\boldsymbol{x}} - \partial_{\boldsymbol{x}}^{(2)}) \cdot \rho_f \boldsymbol{R} = \boldsymbol{R} \cdot \partial_{\boldsymbol{x}} \rho_f + \rho_f \partial_{\boldsymbol{x}}^{(1)} \cdot \boldsymbol{R}, \tag{4.2}$$

where $\partial_{\boldsymbol{x}}^{(1)} \cdot \boldsymbol{R} = \frac{4}{5}\boldsymbol{u}_{fp} \cdot \boldsymbol{\Gamma} + \frac{2}{5}\mathrm{tr}(\boldsymbol{\Gamma})\boldsymbol{u}_{fp}$ and $\boldsymbol{\Gamma}$ is the rate-of-deformation tensor for the fluid phase. In (4.2), $\partial_{\boldsymbol{x}}^{(1)} \cdot \boldsymbol{R}$ can be further decomposed into an isotropic and a traceless component, yielding the second and third terms, respectively, in the exchange force

$$\boldsymbol{F}_{pf} = \alpha_p \boldsymbol{R} \cdot \partial_{\boldsymbol{x}} \rho_f + \tfrac{2}{3}\alpha_p \rho_f (\partial_{\boldsymbol{x}} \cdot \boldsymbol{u}_f) \boldsymbol{u}_{fp} + \tfrac{4}{5}\alpha_p \rho_f \boldsymbol{S} \cdot \boldsymbol{u}_{fp}. \tag{4.3}$$

Analogous manipulations on $\rho_f \boldsymbol{r}$ lead to D_{pf}. It is important to notice that the buoyancy force due to $p_f = \rho_f \Theta_f$ is not included among the exchange forces in (4.3),

https://doi.org/10.1017/jfm.2019.608 Published online by Cambridge University Press

as it appears separately on the left-hand side of the momentum balances. When the fluid density is constant, the first two terms on the right-hand side of (4.3) will be null or negligible. (Aside from g_0 in p_p, the kinetic-theory model does not account for nonlinear terms in α_p. Thus, when ρ_f is constant, $\partial_{\boldsymbol{x}} \cdot \boldsymbol{u}_f = 0$ up to first order in α_p. For a perfect gas, non-zero $\partial_{\boldsymbol{x}} \rho_f$ at constant $p_f = \rho_f \Theta_f$ implies that a fluid temperature gradient exists.) The third term involving the fluid strain-rate tensor $\boldsymbol{S}$ can be further decomposed into a force component in the direction $\boldsymbol{u}_{fp}$ and a tangential force. The former can be combined with the drag force, while the latter represents a lift force. Furthermore, from the point of view of hyperbolicity, the terms involving Θ_p in $\boldsymbol{R}$ and $\boldsymbol{r}$ can be dropped when Θ_p, scaled by the speed of sound in the fluid, is small. (The eigenvalues of the particle phase depend on Θ_p through p_p.) Indeed, dropping the contribution in $\boldsymbol{r}$ significantly simplifies the characteristic equation discussed in § 5.3 and slightly increases the region of hyperbolicity. In practice, all of the terms (including those in $\boldsymbol{R}$) in the direction $\boldsymbol{u}_{fp}$ can be combined with the drag force. Then, as is done for the drag coefficient K, the lift-force definition can be modified to account for viscous flow physics without changing the hyperbolicity of the two-fluid model. Except perhaps across a shock wave, the forces in (4.3) arising due to fluid compressibility will most likely be negligible in actual applications. Likewise, the lift force will be negligible when the density ratio ρ_f/ρ_p is small.

The fluid momentum balance in table 3 can be rewritten in a more familiar form (Lhuillier *et al.* 2013):

$$\rho_f \alpha_f (\partial_t + \boldsymbol{u}_f \cdot \partial_{\boldsymbol{x}}) \boldsymbol{u}_f + \partial_{\boldsymbol{x}} \cdot \boldsymbol{\Pi}_f + \alpha_f \partial_{\boldsymbol{x}} p_f = \boldsymbol{F}, \tag{4.4}$$

where $\boldsymbol{\Pi}_f := \alpha_p \rho_f \boldsymbol{R}$ is the fluid-phase stress tensor arising due to the presence of finite-size particles. The exchange force $\boldsymbol{F} = \boldsymbol{F}_{pf} + K \boldsymbol{u}_{pf}$ has the combined effects of fluid compressibility, drag, and lift due to a mean fluid-velocity gradient. As shall be seen in § 5, this combination of fluid-phase stress tensor and exchange force is sufficient to restore hyperbolicity to the two-fluid model. By summing the two momentum (energy) equations, the mixture pressure tensor and energy flux are, respectively,

$$\boldsymbol{P} = (p_f + p_p) \boldsymbol{I} + \alpha_p \rho_f \boldsymbol{R}, \quad \text{and} \quad \boldsymbol{q} = \alpha_f p_f \boldsymbol{u}_f + (p_p + \alpha_p p_f) \boldsymbol{u}_p + \alpha_p \rho_f \boldsymbol{r}, \tag{4.5a,b}$$

wherein $\boldsymbol{R}$ always increases the mixture pressure (i.e. the trace of $\boldsymbol{P}$). Moreover, the mixture balance equations have the form of hyperbolic conservation laws. Thus, as discussed in Chu & Prosperetti (2016) for volume averaging, the kinetic-theory derivation provides a unique distribution of $\boldsymbol{P}$ and $\boldsymbol{q}$ between the two phases. In addition, it uniquely defines the contribution of the stress tensor $\boldsymbol{R}$, the energy flux $\boldsymbol{r}$, and the momentum/energy-exchange terms, which must be modelled (or neglected) in a volume-averaging approach. Also, it is interesting to note that the term $\alpha_p \boldsymbol{R} \cdot \partial_{\boldsymbol{x}} \rho_f$ in $\boldsymbol{F}_{pf}$ has the form of a dispersion force, which is known to make the system hyperbolic under certain conditions on $\boldsymbol{R}$ (see discussion in Lhuillier *et al.* 2013). However, here the dispersion force is due to fluid-density gradients and not volume-fraction gradients as is usually the case (see Panicker *et al.* 2018). Thus, this dispersion force will be null in flows with constant fluid density and, therefore, must play a minor role in determining the hyperbolicity of the two-fluid model. Nonetheless, one cannot entirely rule out the existence of a dispersion force proportional to $\partial_{\boldsymbol{x}} \alpha_f$. For example, if in (2.10) the model for $f^{(2)}$ had $h_1 \partial_{\boldsymbol{x}} f_1$ in place of $\partial_{\boldsymbol{x}}(h_1 f_1)$ then such a force would be present in $\boldsymbol{F}_{pf}$ for a perfect gas where $h_1 = g_{12} = 1/\alpha_f$. (Writing $h_1 \partial_{\boldsymbol{x}} f_1 = \partial_{\boldsymbol{x}}(h_1 f_1) - h_1 f_1 \partial_{\boldsymbol{x}} \ln h_1$, for a perfect gas the dispersion force would take the form $\alpha_p \rho_f \boldsymbol{R} \cdot \partial_{\boldsymbol{x}} \alpha_f$ and would be added to $\boldsymbol{F}_{pf}$ in (4.3).) However, as $g_{12} f_1$ represents

https://doi.org/10.1017/jfm.2019.608 Published online by Cambridge University Press

the probability of a type-1 particle to be located at the surface of a type-2 particle (Chapman & Cowling 1952), experimentally verifiable physical arguments would be needed to justify inclusion of a dispersion force in the two-fluid model in table 3.

The total energy balances in table 3 can be replaced by the fluctuating energy balances (written here for $\gamma_f = \gamma_p = 5/3$)

$$\left.\begin{array}{c} \frac{3}{2}\rho_f\alpha_f(\partial_t + \boldsymbol{u}_f\cdot\partial_{\boldsymbol{x}})\Theta_f + p_f\partial_{\boldsymbol{x}}\cdot(\alpha_f\boldsymbol{u}_f + \alpha_p\boldsymbol{u}_p) + \partial_{\boldsymbol{x}}\cdot(\alpha_p\rho_f\boldsymbol{r}) - \boldsymbol{u}_f\cdot(\partial_{\boldsymbol{x}}\cdot\alpha_p\rho_f\boldsymbol{R}) \\ = D_{pf} - \boldsymbol{u}_f\cdot\boldsymbol{F}_{pf} + K(3\Theta_p + |\boldsymbol{u}_{fp}|^2), \\ \frac{3}{2}\rho_p\alpha_p(\partial_t + \boldsymbol{u}_p\cdot\partial_{\boldsymbol{x}})\Theta_p + p_p\partial_{\boldsymbol{x}}\cdot\boldsymbol{u}_p = D_{fp} + \boldsymbol{u}_p\cdot\boldsymbol{F}_{pf} - 3K\Theta_p, \end{array}\right\} \quad (4.6)$$

where the source terms due to compression heating are evident on the left-hand sides. Compression heating in the particle phase is transferred to the fluid phase by drag (i.e. K). This model with six equations and six variables (i.e. $\rho_f\alpha_f$, $\boldsymbol{u}_f$, Θ_f, $\rho_p\alpha_p$, $\boldsymbol{u}_p$, Θ_p) is the simplest possible two-fluid model that accounts for fluctuating energy in both phases. It is worth noting that this model is reminiscent of the so-called turbulent dilute two-phase flow model proposed by Hank *et al.* (2011). In that work, the particle pressure is found by invoking turbulence, while in this work it naturally arises from the microscopic description employed in the kinetic-theory model due, for example, to bi-modal velocity distribution functions (see Février, Simonin & Squires 2005; Desjardins *et al.* 2008; Fox, Laurent & Massot 2008; Fox 2009; Vié *et al.* 2011; Fox 2012, 2014; Vié *et al.* 2015, for complete discussions of this topic).

Finally, note that the BE term in the fluid-phase momentum equation removes the need for *a posteriori* corrections to describe the 'nozzling effect' discussed in Saurel & Abgrall (1999), which arises in a perfect gas ($\varphi_1 \to 0$) due to a spatial gradient in α_p when p_f is uniform, the velocities are null and $\Theta_p = 0$. Likewise, for the same conditions, the fluid-phase equations in table 3 are nearly the same as in Houim & Oran (2016), but with the additional BE terms $\boldsymbol{R}$ and $\boldsymbol{r}$. In Houim & Oran (2016), they define $E_s = \frac{3}{2}\Theta_s$, i.e. the fluctuating instead of the total energy, which corresponds to (4.6) for Θ_p in this work. Again, except for the BE terms, their particle-phase equations are the same as in table 3. Thus, any differences in the region of hyperbolicity for a perfect gas from their work will be due to the BE terms. Finally, unlike in Houim & Oran (2016), the phase entropies will have source/exchange terms that arise to due to $\boldsymbol{R}$ and $\boldsymbol{r}$, which makes the characteristic polynomial used to check with hyperbolicity in § 5 significantly more complex.

5. Hyperbolicity of 1-D model

In order to determine whether the full 3-D model in table 2 is hyperbolic with respect to the spatial fluxes, it suffices to consider a system with one spatial direction (see, e.g. Ndjinga 2007; Kumbaro & Ndjinga 2011; Lhuillier *et al.* 2013). This 1-D model is given in table 4, written in terms of the six independent variables $\boldsymbol{X} = (\varphi_1, u_1, E_1, \varphi_2, u_2, E_2)^{\mathrm{t}}$. Here, we are interested in whether the 1-D model is hyperbolic (i.e. the flux matrix has real and distinct eigenvalues). The terms on the right-hand side (e.g. drag) do not contain gradients in time nor space, and therefore do not play any role in the hyperbolicity of the system. As a reference, we begin with the uncoupled model wherein the eigenvalues for one phase are uncoupled from the other phase.

5.1. *Uncoupled model*

Formally, the 1-D model can be rewritten as

$$\boldsymbol{A}(\boldsymbol{X})\partial_t\boldsymbol{X} + \boldsymbol{B}(\boldsymbol{X})\partial_x\boldsymbol{X} = \boldsymbol{C}(\boldsymbol{X}), \quad (5.1)$$

https://doi.org/10.1017/jfm.2019.608 Published online by Cambridge University Press

$$\partial_t\varphi_1 + u_1\partial_x\varphi_1 + \varphi_1\partial_x u_1 = 0$$
$$\varphi_1\partial_t u_1 + \varphi_1 u_1\partial_x u_1 + \partial_x[\varphi_1\Theta_1(1+4\varphi_1 g_0) + \varphi_1\varphi_2 g_{12}P^*] - \varphi_2(\partial_x - \partial_x^{(2)})\varphi_1 h_1 P^* = K^* u_{21}$$
$$\varphi_1\partial_t E_1 + \varphi_1 u_1\partial_x E_1 + \partial_x[\varphi_1\Theta_1(1+4\varphi_1 g_0)u_1 + \varphi_1\varphi_2 g_{12}q^*] - \varphi_2(\partial_x - \partial_x^{(2)})\varphi_1 h_1 q^* = D_E^*$$
$$\partial_t\varphi_2 + u_2\partial_x\varphi_2 + \varphi_2\partial_x u_2 = 0$$
$$\varphi_2\partial_t u_2 + \varphi_2 u_2\partial_x u_2 + \partial_x\varphi_2\Theta_2(1+4\varphi_2 g_0) + Z\varphi_2(\partial_x - \partial_x^{(2)})\varphi_1 h_1 P^* = ZK^* u_{12}$$
$$\varphi_2\partial_t E_2 + \varphi_2 u_2\partial_x E_2 + \partial_x\varphi_2\Theta_2(1+4\varphi_2 g_0)u_2 + Z\varphi_2(\partial_x - \partial_x^{(2)})\varphi_1 h_1 q^* = -ZD_E^*$$
$$P^* = \Theta_1 + \Theta_2 + \tfrac{3}{5}u_{12}^2 \quad (\partial_x - \partial_x^{(2)})\varphi_1 h_1 P^* = P^*\partial_x\varphi_1 h_1 + \varphi_1 h_1(\partial_x\Theta_1 + \tfrac{6}{5}u_{12}\partial_x u_1)$$
$$q^* = P^* u_2 - 2\Theta_2 u_{12} \quad (\partial_x - \partial_x^{(2)})\varphi_1 h_1 q^* = u_2(\partial_x - \partial_x^{(2)})\varphi_1 h_1 P^* - 2\varphi_1 h_1\Theta_2\partial_x u_1$$
$$D_E^* = K^*(3\Theta_2 + u_2 u_{21}) \quad h_1 = g_{12} + (4g_0 - g_{12})\varphi_1 \quad g_0 = \frac{2-\varphi}{2(1-\varphi)^3} \quad g_{12} = \frac{1}{1-\varphi}$$

TABLE 4. One-dimensional two-fluid model with six independent variables $\boldsymbol{X} := (\varphi_1, u_1, E_1, \varphi_2, u_2, E_2)^{\mathrm{t}}$. Material densities ρ_1 and ρ_2 are constant and $Z = \rho_1/\rho_2$. The other variables are $\varphi = \varphi_1 + \varphi_2$, $u_{12} = -u_{21} = u_1 - u_2$ and $\Theta_\alpha = \frac{2}{3}(E_\alpha - \frac{1}{2}u_\alpha^2)$. Note that $P^* := P_{BE}^*/\rho_1$, $K^* := K/\rho_1$ and $q^* := q_{BE}^*/\rho_1$.

where the coefficient matrices $\boldsymbol{A}$ and $\boldsymbol{B} := \boldsymbol{B}^* + \boldsymbol{B}_0$ yield the flux matrix $\boldsymbol{F} := \boldsymbol{A}^{-1}\boldsymbol{B}$. The matrix $\boldsymbol{B}_0$ is the contribution due to the coupled behaviour, and its form is complicated due to the nonlinear dependencies of g_0 and g_{12} on φ_α. However, as done here, $\boldsymbol{B}_0$ can be easily computed using symbolic software. $\boldsymbol{A}$ and $\boldsymbol{B}^*$ are from the uncoupled system with only drag (i.e. $K > 0$ and $P^* = q^* = g_0 = 0$). Written in terms of the components of $\boldsymbol{X}$, the latter are

$$\boldsymbol{A} := \begin{bmatrix} 1 & 0 & 0 & 0 & 0 & 0 \\ 0 & \varphi_1 & 0 & 0 & 0 & 0 \\ 0 & 0 & \varphi_1 & 0 & 0 & 0 \\ 0 & 0 & 0 & 1 & 0 & 0 \\ 0 & 0 & 0 & 0 & \varphi_2 & 0 \\ 0 & 0 & 0 & 0 & 0 & \varphi_2 \end{bmatrix}, \tag{5.2}$$

and

$$\boldsymbol{B}^* := \begin{bmatrix} \boldsymbol{B}_1 & 0 \\ 0 & \boldsymbol{B}_2 \end{bmatrix}, \tag{5.3}$$

with

$$\boldsymbol{B}_1 := \begin{bmatrix} u_1 & \varphi_1 & 0 \\ \frac{2}{3}E_1 - \frac{1}{3}u_1^2 & \frac{1}{3}\varphi_1 u_1 & \frac{2}{3}\varphi_1 \\ u_1\left(\frac{2}{3}E_1 - \frac{1}{3}u_1^2\right) & \varphi_1\left(\frac{2}{3}E_1 - u_1^2\right) & \frac{5}{3}\varphi_1 u_1 \end{bmatrix}, \tag{5.4}$$

and

$$\boldsymbol{B}_2 := \begin{bmatrix} u_2 & \varphi_2 & 0 \\ \frac{2}{3}E_2 - \frac{1}{3}u_2^2 & \frac{1}{3}\varphi_2 u_2 & \frac{2}{3}\varphi_2 \\ u_2\left(\frac{2}{3}E_2 - \frac{1}{3}u_2^2\right) & \varphi_2\left(\frac{2}{3}E_2 - u_2^2\right) & \frac{5}{3}\varphi_2 u_2 \end{bmatrix}. \tag{5.5}$$

Given the form of (5.3), we observe that the fluid- and particle-phase fluxes are uncoupled and have an identical structure. The six eigenvalues for the flux matrix of the uncoupled model are

$$u_1,\ u_1 \pm \sqrt{\tfrac{5}{3}\Theta_1}, \quad u_2,\ u_2 \pm \sqrt{\tfrac{5}{3}\Theta_2}, \tag{5.6a,b}$$

https://doi.org/10.1017/jfm.2019.608 Published online by Cambridge University Press

and hence the uncoupled model is hyperbolic if $0 < \Theta_1$ and $0 < \Theta_2$. Given that the mass ratio between the particles and fluid molecules is very large, we expect to have $\Theta_2 \ll \Theta_1$ (i.e. the speed of sound in the fluid phase is much larger than in the particle phase). As expected (Marble 1970), with only drag, the flux matrix for a very dilute system (i.e. $\varphi \ll 1$) has the form of two uncoupled compressible (i.e. perfect gas) systems with independent eigenvalues. Recall, however, that when $\varphi_2 \ll 1$, particle–particle collisions will be rare, and therefore second-order models for the particle phase will be inaccurate unless the particle Stokes number is very small (see discussion in Vié *et al.* 2015).

5.2. *Application of Sturm's theorem*

The eigenvalues of the complete 1-D model depend on the following five parameters:

$$Ma_s = \frac{u_2 - u_1}{\sqrt{5\Theta_1/3}}, \quad \Theta_r = \frac{\Theta_2}{\Theta_1}, \quad \mathcal{Z} = \frac{\rho_f}{\rho_p} = \frac{\rho_1\varphi_1}{\rho_2(1-\varphi_2)}, \quad \varphi_1, \quad \varphi_2. \tag{5.7a–e}$$

Because the model is Galilean invariant, in the frame of reference of the fluid, we can choose $u_1 = 0$ in the characteristic polynomial for the eigenvalues. Using this frame of reference, the six eigenvalues of the uncoupled model are

$$0, \pm 1, Ma_s, Ma_s \pm \sqrt{\Theta_r}, \tag{5.8}$$

and will be used to compare with the eigenvalues of the complete model. For the latter, the flux matrix $\boldsymbol{F}$ and the characteristic polynomial $p_0(x)$ can be computed using symbolic software, and depend on the five parameters above. In order to determine whether this sixth-degree polynomial has real roots, we make use of Sturm's theorem (Sturm 1829) for the interval $(-\infty, +\infty)$. For this purpose, we compute symbolically the Sturm chain $p_0(x)$, $p_1(x)$, ... , $p_6(x)$ using polynomial long division (https://fr.wikipedia.org/wiki/Théorème_de_Sturm). This sequence of polynomials has decreasing degree such that p_6 is zero-degree. According to Sturm's theorem, it suffices that the coefficient of the highest-order term in each of these polynomials be positive to prove that all six eigenvalues are real valued. For the 1-D model, it is found that only p_5 and p_6 are needed to determine whether the system is hyperbolic for a given choice of $(Ma_s, \Theta_r, \mathcal{Z}, \varphi_1, \varphi_2)$. While these two coefficients can be computed analytically using symbolic software, they are too complicated to analyse directly to find the constraints on the five parameters. However, they are easily computed numerically for a given set of parameters. In the analysis below, we define a test function $f(\varphi_2, \Theta_r)$ equal to the minimum of the Sturm coefficients for fixed parameters $(Ma_s, \mathcal{Z}, \varphi_1)$. According to Sturm's theorem, if $f(\varphi_2, \Theta_r) < 0$, then at least two eigenvalues are complex. Note that the maximum of f is unity due to the normalization of p_0. Below, we will use hyperbolicity plots in the φ_2–Θ_r plane to show where the Sturm test function is non-negative for fixed values of $(\varphi_1, Ma_s, \mathcal{Z})$.

In general, as will be shown in detail below, the hyperbolic region of the two-fluid model in table 4 is similar to that found by Houim & Oran (2016). In analogy to their notation, Ma_s corresponds to M_{slip}, Θ_r to C_r, and (roughly) $\mathcal{Z}$ to z. However, the present model depends separately on $\mathcal{Z}$, φ_1, φ_2, while, written in our notation, $z = \mathcal{Z}\varphi_2/(1-\varphi_2)$ and $\varphi_1 \to 0$ in Houim & Oran (2016), i.e. the two parameters are equal for a perfect gas when $\alpha_p = \frac{1}{2}$; otherwise, in most physically relevant cases, $z < \mathcal{Z}$. For $Ma_s = 0$ or $\mathcal{Z} = 0$, both models are strictly hyperbolic. However, as shown below, in contrast to the model in Houim & Oran (2016), the two-fluid

https://doi.org/10.1017/jfm.2019.608 Published online by Cambridge University Press

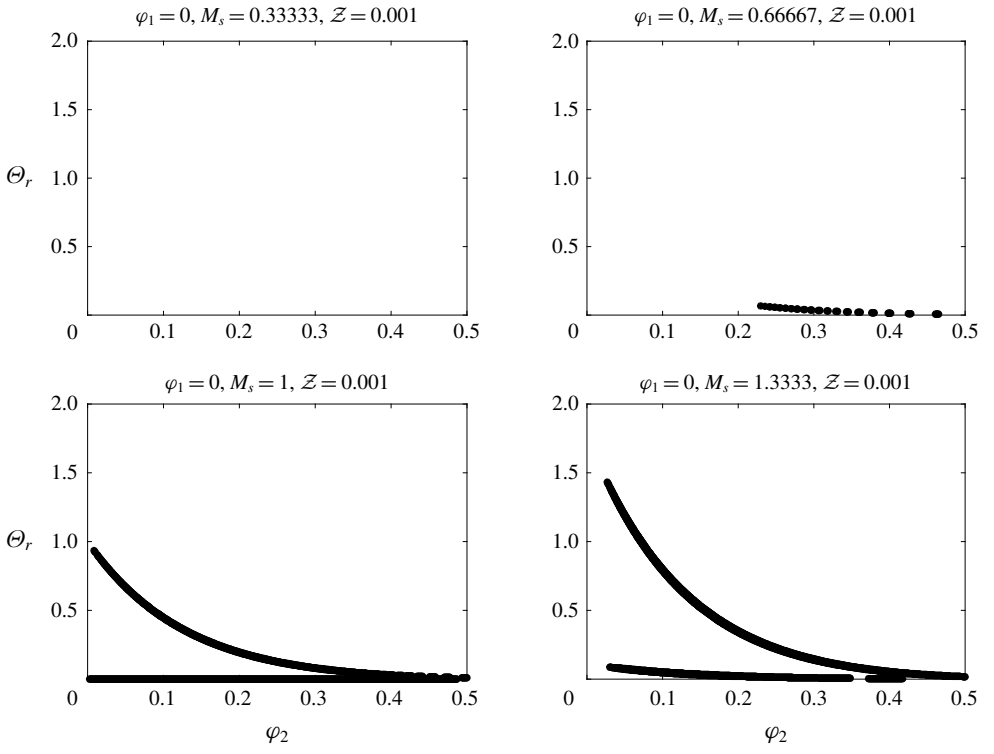


FIGURE 1. Hyperbolicity plot for perfect gas ($\varphi_1 = 0$) with $\mathcal{Z} = 0.001$ and varying Ma_s. The Sturm test function is negative in black regions, indicating that the 1-D model has complex eigenvalues.

model in table 4 is hyperbolic for all values of the other parameters if Ma_s is small enough, including $\mathcal{Z} \geqslant 0.1$. For larger Ma_s, the model is hyperbolic except for certain combinations of Θ_r and φ_α. Note that in a gas–particle flow, we expect physically that $\mathcal{Z} \ll 1$, i.e. the density of the gas will be (much) smaller than that of the solid. Having values of $\mathcal{Z} \geqslant 1$ can only occur when the fluid is a liquid (or with $\rho_1 \gg \rho_2$), in which case $\varphi_1 \approx 0.63$ for a pure fluid. For a pure liquid, φ_1 could be chosen to produce the correct speed of sound. For the hard-sphere fluid, the speed of sound increases due to g_0 as φ approaches unity. Nevertheless, a stiffened gas model, coupled with an added-mass model, may be a better choice for representing a compressible liquid. Thus, any complex eigenvalues observed when $\mathcal{Z} \geqslant 0.1$ and $\varphi_1 \ll 0.63$ are unphysical because of the unphysical choice of parameters. Moreover, when $\mathcal{Z} \geqslant 0.1$, the drag force will quickly damp out Θ_2 so that only small values of Θ_r are physically relevant. For practical applications, we will mainly be interested in the perfect gas model, which corresponds to the two-fluid model in table 3. Nonetheless, for completeness, we will consider all mathematically relevant values when testing the system for real eigenvalues.

5.3. *Perfect gas*

For a perfect gas ($\varphi_1 \to 0$), the regions where the Sturm test function is negative are shown in figures 1–4 for $\mathcal{Z} = 0.001$, 0.01 and 0.1, respectively. As noted above,

https://doi.org/10.1017/jfm.2019.608 Published online by Cambridge University Press

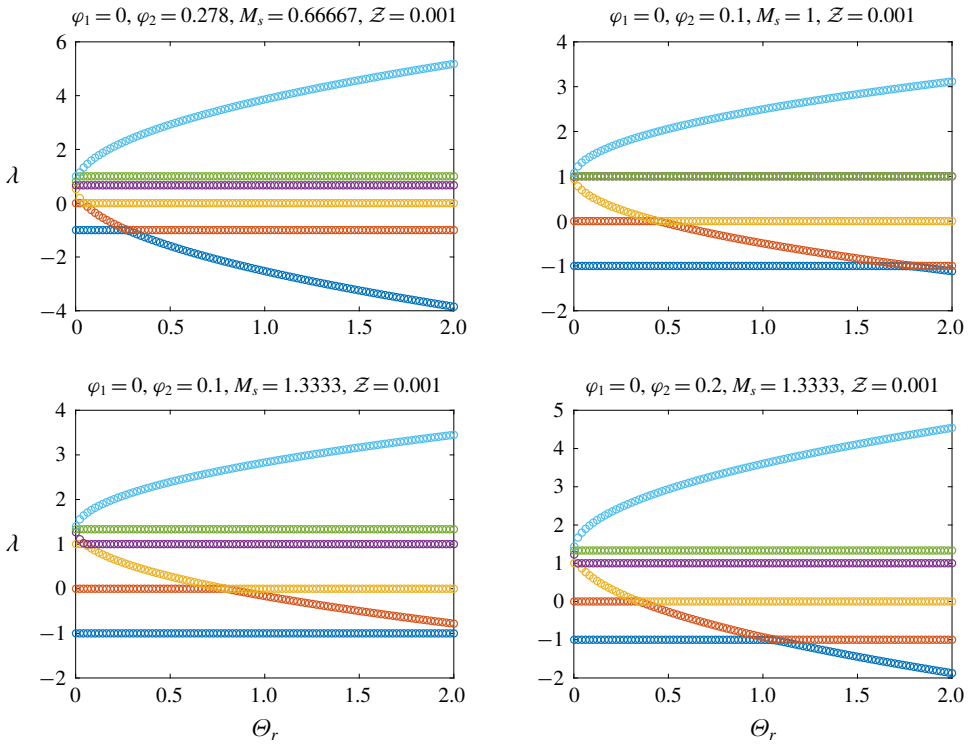


FIGURE 2. (Colour online) Real part of eigenvalues versus Θ_r for perfect gas ($\varphi_1 = 0$) with $\mathcal{Z} = 0.001$. Values of Ma_s and φ_2 are chosen to cross curves with a negative Sturm test function in figure 1.

the Sturm test function is non-negative for $\mathcal{Z} = 0$. In figure 1, we observe that the Sturm test function is non-negative for $M_s \leqslant 1/3$ for all values of φ_2. For $Ma_s \geqslant 2/3$, a curve exists for which the Sturm test function is negative. In figure 1(*c*), this curve extends to lower values of ϕ_2. Similarly, in figure 1(*d*), a second curve is evident along which the 1-D model loses hyperbolicity. In order to understand the behaviour of the eigenvalues when the Sturm test function is negative, we plot them against Θ_r in figure 2. In this figure, the 'gas-phase' eigenvalues correspond to $(-1, 0, 1)$, while two of the 'particle-phase' eigenvalues grow in magnitude with increasing Θ_r. The complex eigenvalues, when they exist, occur when one of these two eigenvalues overlap with the gas-phase eigenvalues. From figure 2, the complex eigenvalues occur at a single point (which is consistent with figure 1). Thus, for $\mathcal{Z}$ values typical of gas–particle flows we can expect that the loss of hyperbolicity will not be issue in numerical simulations, even if M_s is larger than unity. Moreover, in applications to real particles, we expect $0 < \Theta_r \ll 1$ (see Tavenashad *et al.* 2019, for examples) and, hence, the particle-phase eigenvalue will only interact with the gas-phase eigenvalue located at 0.

The results for larger $\mathcal{Z}$ are given in figures 3–5, where it can be seen that the non-hyperbolic regions grow larger as $\mathcal{Z}$ increases. For $Ma_s \leqslant 1/3$, the system is hyperbolic for all physically relevant values of φ_2 and Θ_f. When $Ma_s \geqslant 2/3$, the system can have a pair of complex eigenvalues in larger regions of φ_2–Θ_r space, which are significantly larger for $\mathcal{Z} = 0.1$. Houim & Oran (2016) found similar

https://doi.org/10.1017/jfm.2019.608 Published online by Cambridge University Press

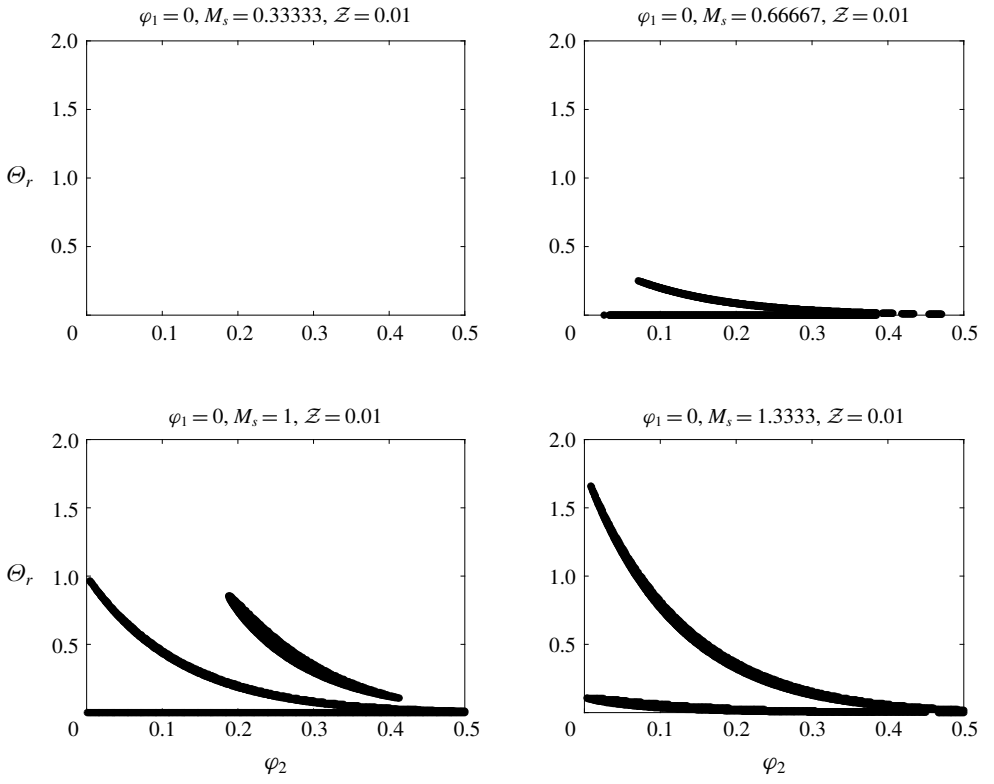


FIGURE 3. Hyperbolicity plot for perfect gas ($\varphi_1 = 0$) with $\mathcal{Z} = 0.01$ and varying Ma_s. The Sturm test function is negative in black regions, indicating that 1-D model has complex eigenvalues.

behaviour for their model, but in their case complex eigenvalues were found for $\Theta_r = 0$ for all values of Ma_s. Having complex eigenvalues with $\Theta_r = 0$ is particularly troublesome as this corresponds to the equilibrium value of Θ_2. However, tests with a kinetic-based added-mass term (not shown here) indicate that the system recovers hyperbolicity for small Θ_r because with added mass the three particle-phase eigenvalues are no longer equal at $\Theta_r = 0$. In figure 5 the eigenvalues are plotted for parameter sets that exhibit non-hyperbolic behaviour. We can observe from figure 5 that the Sturm test function correctly predicts the values of Θ_r where two eigenvalues have the same real parts (i.e. complex conjugates).

In summary, for a perfect gas the two-fluid model is strictly hyperbolic for all physically realistic values of the parameters if Ma_s and $\mathcal{Z}$ are not too large. The value of $Ma_s \leqslant 1/3$ is not a rigorous upper bound for hyperbolicity; however, as discussed in the derivation of the model, one should not expect the pair distribution function g_{12} in (2.11) to be accurate for larger values of Ma_s. Thus, the non-hyperbolic regions seen in the figures above for $Ma_s > 1/3$ should not be encountered in gas–particle simulations for which the proposed two-fluid model is physically applicable. In appendix C a simpler system with $g_0 = 0$ is investigated and confirms these conclusions. Indeed, with $g_0 = 0$ the hyperbolic region is much larger than when the particle phase has a non-ideal pressure model, which would seem counter-intuitive *vis-a-vis* the coupling with the gas phase.

https://doi.org/10.1017/jfm.2019.608 Published online by Cambridge University Press

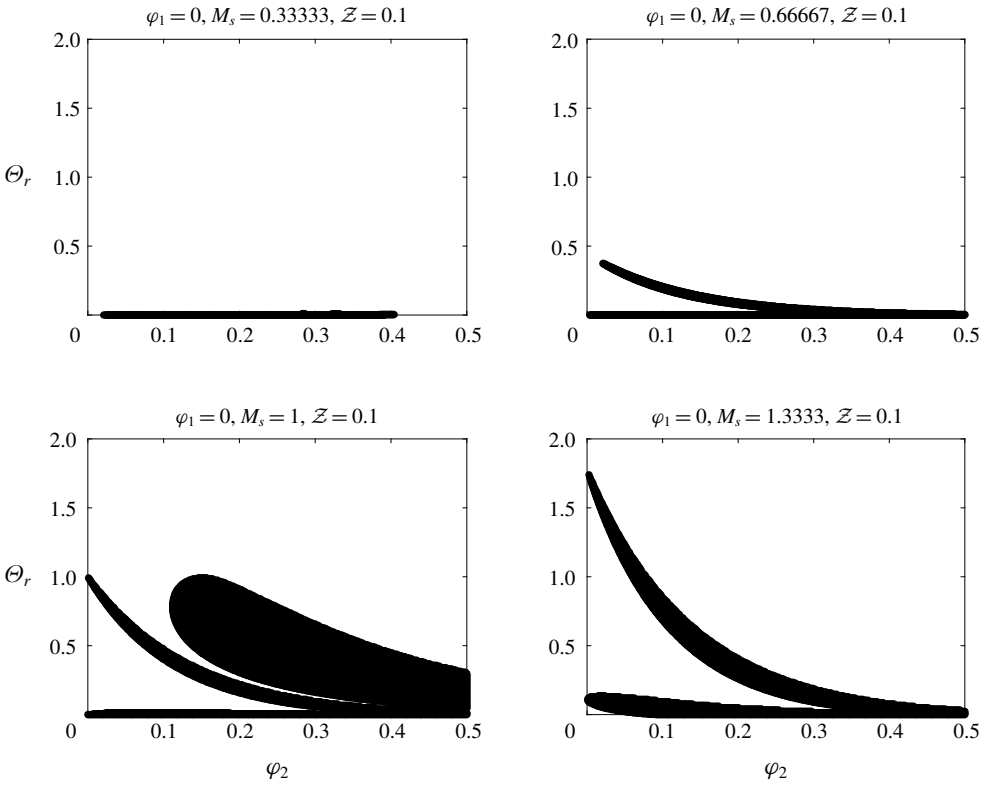


FIGURE 4. Hyperbolicity plot for perfect gas ($\varphi_1 = 0$) with $\mathcal{Z} = 0.1$ and varying Ma_s. The Sturm test function is negative in black regions, indicating that 1-D model has complex eigenvalues.

5.4. *Non-ideal gas*

By setting $\varphi = 0.01$, the gas becomes non-ideal and the gas-phase eigenvalues (with $\mathcal{Z} = 0$) depend on g_0 and thus are slightly larger than for the perfect gas. The hyperbolicity plots found from the Sturm test functions are given in figures 6–8, and example eigenvalues in figure 9. In these figures, all other parameters are treated in the same manner as done for the perfect gas. Qualitatively, the non-ideal gas behaves very similarly to the perfect gas. The regions in parameter space where the system is hyperbolic are slightly modified by increasing φ_1. Quantitatively, the eigenvalues have larger magnitudes due to the higher gas-phase speed of sound. In addition, when $M_s > 1/3$ there is a region with large φ_2 and Θ_r that has complex eigenvalues, and this region moves to smaller φ_2 as $\mathcal{Z}$ increase. Overall, the two-fluid model with a non-ideal gas is again hyperbolic for physically realistic values of the parameters if Ma_s and $\mathcal{Z}$ are not too large.

5.5. *Dense gas*

With $\varphi_1 = 0.1$, the gas is dense, i.e. the fluid molecular volume fraction is as large as the particle volume fraction φ_2. The Sturm test function plots for this case are given in figures 10–12, and example eigenvalues in figure 13. In these figures, all other parameters are treated in the same manner as done for the perfect and non-ideal gases.

https://doi.org/10.1017/jfm.2019.608 Published online by Cambridge University Press

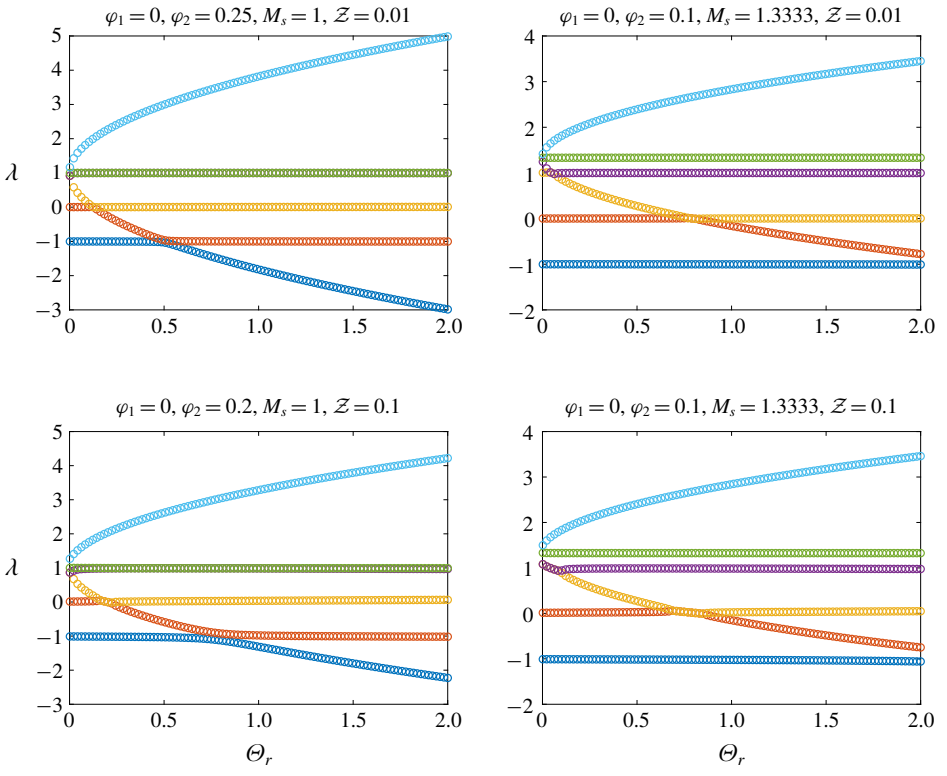


FIGURE 5. (Colour online) Real part of eigenvalues versus Θ_r for perfect gas ($\varphi_1 = 0$) with $\mathcal{Z} = 0.01$ and 0.1. Values of Ma_s and φ_2 are chosen to cross curves with a negative Sturm test function in figures 3 and 4.

As expected, the effect of g_0 is to push the two 'gas-phase' eigenvalues further from the origin. From the hyperbolicity plots, we can observe that the dense gas generally makes the system less hyperbolic for a given value of φ_2. For example, comparing figure 10 to figure 1, we can observe that for $M_s > 2/3$ the non-hyperbolic regions found with $\varphi_2 = 0.1$ occur at larger Θ_r in figure 10. Furthermore, in figure 12 we see that for the dense gas the non-hyperbolic region at $\Theta_r = 0$ is no longer present. In summary, the two-fluid model with a dense gas is hyperbolic for physically realistic values of the parameters if Ma_s is not too large.

6. Discussion and conclusions

As stated in § 1, the principal objective of this work is to provide a rigorous derivation of a two-fluid model for a particular system, namely a binary, hard-sphere mixture in the limit where the particle diameters are widely separated in size, but including the Archimedes force. To attain this objective, we make use of the Boltzmann–Enskog kinetic theory for hard spheres. In appendix A we demonstrate that by keeping terms up to first order in the spatial gradients in the BE collision model, the collisional fluxes and collisional source terms can be evaluated analytically for the velocity moments appearing in the two-fluid model. Remarkably, the BE contributions to the pressure tensors $\boldsymbol{P}_{BE}$ and to the energy fluxes $\boldsymbol{G}_{BE}$ appear in closed form, giving rise to closed expressions for the momentum/energy-exchange

https://doi.org/10.1017/jfm.2019.608 Published online by Cambridge University Press

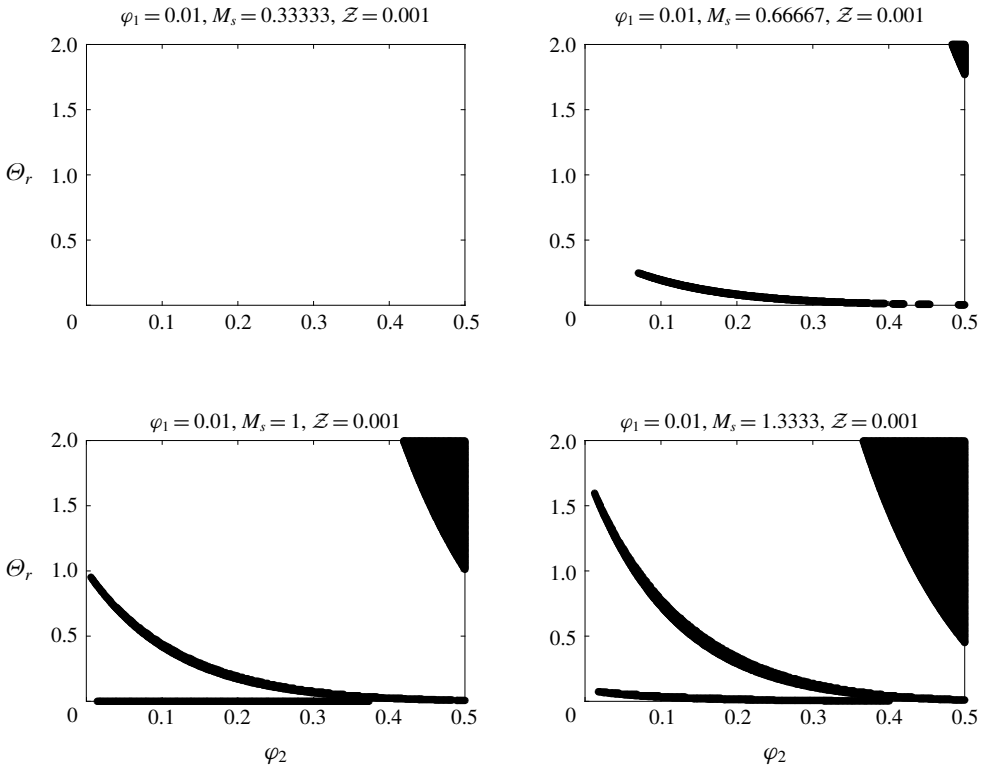


FIGURE 6. Hyperbolicity plot for non-ideal gas ($\varphi_1 = 0.01$) with $\mathcal{Z} = 0.001$ and varying Ma_s and φ_2. The Sturm test function is negative in black regions, indicating that the 1-D model has complex eigenvalues.

terms in the momentum and energy balances. By invoking the anisotropic Gaussian model wherein the third-order central velocity moments $\boldsymbol{Q}$ are null, the six-equation two-fluid model for a binary, hard-sphere mixture is completely defined in terms of the mass concentrations ϱ_α, the phase momenta $\varrho_\alpha \boldsymbol{u}_\alpha$ and the phase energy tensors $\varrho_\alpha \boldsymbol{E}_\alpha$ for $\alpha = 1, 2$.

The BE tensors $\boldsymbol{P}_{BE}$ and $\boldsymbol{G}_{BE}$ arise due to finite-size particles, but were neglected in previous derivations (e.g. Hamel 1966; Goldman & Sirovich 1967). It is notable that these tensors are exact (i.e. they do not depend on the form of the velocity distribution functions) and that they depend on the variables from both phases (e.g. the mean-slip velocity). In contrast to previous two-fluid models (with the exception of Zhang *et al.* 2006) for compressible particle-laden flows wherein the fluxes depend only on the variables for a given phase, the mass, momentum and energy fluxes in the two-fluid model in table 3 appear in closed form and depend on the variables from both phases. We should recall here that in 'classical' derivations of transport equations for binary hard-sphere mixtures (see, e.g. Hamel 1966; Goldman & Sirovich 1967; Barajas *et al.* 1973; Garzó *et al.* 2007, 2012), the mixture velocity and energy are employed instead of the phase variables (i.e. three, instead of six equations). For this reason, the 'classical' derivation requires closures for transport coefficients that will not be valid when the mean-slip velocity is significant (i.e. far from the equilibrium state). Thus, the price to be paid for using the two-fluid model in table 3 is that the

https://doi.org/10.1017/jfm.2019.608 Published online by Cambridge University Press

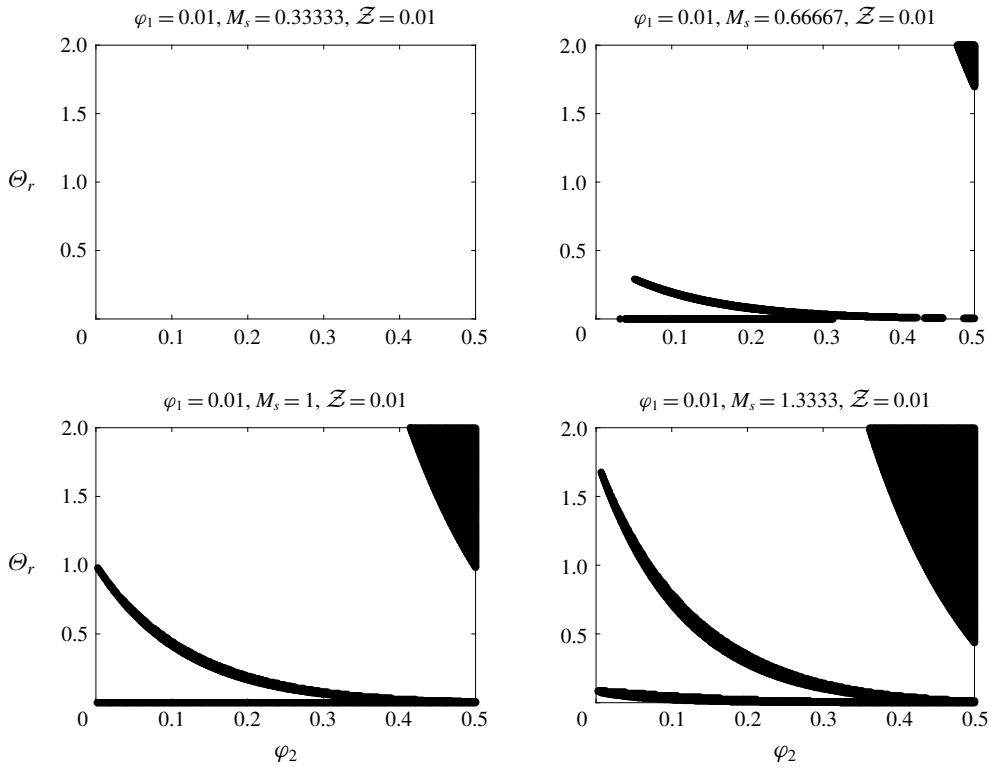


FIGURE 7. Hyperbolicity plot for non-ideal gas ($\varphi_1 = 0.01$) with $\mathcal{Z} = 0.01$ and varying Ma_s and φ_2. The Sturm test function is negative in black regions, indicating that the 1-D model has complex eigenvalues.

fluxes for each phase are coupled to the variables in the other phase. Finally, it is also noteworthy that $\boldsymbol{P}_{BE}$ and $\boldsymbol{G}_{BE}$ modify the fluxes and introduce a source term coupling the two phases. Thus, one can speculate that this would also be true for other source terms involving gradients in space and time. In other words, the addition of a source term will imply that the exact two-fluid model should have additional fluxes involving the variables from both phases, which is consistent with the results in Zhang *et al.* (2006).

As discussed in § 1, binary hard-sphere collisions are a particular case for the general kinetic-based framework developed in Zhang *et al.* (2006), as are the averaged equations studied in Zhang & Prosperetti (1994). Indeed, the momentum equations in the fluid–particle limit have a common form with the interspecies stress term appearing in the fluid momentum equation (i.e. $\boldsymbol{\sigma}^{(21)}$ in Zhang *et al.* (2006), $\boldsymbol{T}_C$ in Zhang & Prosperetti (1994) and $-\rho_f \boldsymbol{R}$ in table 3). The formal definition of this tensor is given by equation (7) in Zhang *et al.* (2006) and depends on the forces applied by particles of type-2 on particles of type-1. Therefore, the resulting expression for $\boldsymbol{\sigma}^{(21)}$ depends on the choice of these forces. Zhang & Prosperetti (1994) computed $\boldsymbol{T}_C$ from the pressure field exerted on the surface of a particle (type-2) by an Euler fluid (type-1) and found

$$\boldsymbol{T}_C = \tfrac{1}{5}\rho_f \left[2(u_{fp}^2 + 3\Theta_p)\boldsymbol{I} - \tfrac{9}{4}(\boldsymbol{u}_{fp} \otimes \boldsymbol{u}_{fp} + \boldsymbol{\sigma}_p)\right], \tag{6.1}$$

https://doi.org/10.1017/jfm.2019.608 Published online by Cambridge University Press

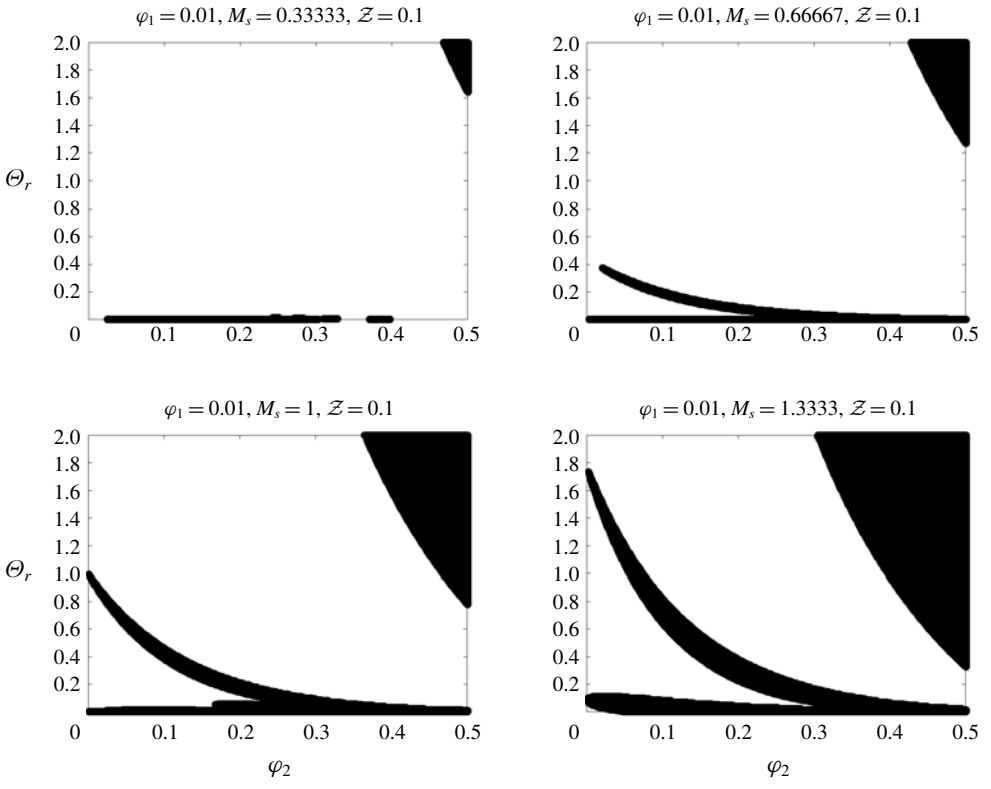


FIGURE 8. Hyperbolicity plot for non-ideal gas ($\varphi_1 = 0.01$) with $\mathcal{Z} = 0.1$ and varying Ma_s and φ_2. The Sturm test function is negative in black regions, indicating that the 1-D model has complex eigenvalues.

which has $\mathrm{tr}(\boldsymbol{T}_C) \geqslant 0$, i.e. their interspecies stress term reduces the mixture pressure. In contrast, with hard-sphere collisions we find that $\mathrm{tr}(\boldsymbol{R}) \geqslant 0$ so that the interspecies stress term increases the mixture pressure. For both choices, the tensorial components are the same (i.e. $\boldsymbol{I}$, $\boldsymbol{u}_{fp} \otimes \boldsymbol{u}_{fp}$ and $\boldsymbol{\sigma}_p$), but multiplied by different coefficients. From the standpoint of hyperbolicity, decreasing the mixture pressure will favour complex eigenvalues. Thus, from this standpoint, the hard-sphere expression for $\boldsymbol{\sigma}^{(21)}$ is preferable. However, the Euler fluid also produces an added-mass force that is not present in the hard-sphere model. Analysis of the hyperbolicity region for the Zhang & Prosperetti model would be needed before conclusions can be drawn concerning the relative merits of the two models. Nevertheless, it is likely that due to the starting point of their derivations (e.g. Euler fluid versus hard-sphere mixture) the two models are applicable to different regimes (i.e. bubbly flow versus compressible gas–solid flow, respectively).

The complete model in § 3 for a binary, hard-sphere mixture involves 20 variables: two mass densities, six velocity components and the 12 components of the (symmetric) energy tensors. In principle, this system could be solved using numerical methods developed for the anisotropic Gaussian model (Vié *et al.* 2015; Kong *et al.* 2017; Kong & Fox 2019). However, in the fluid limit where one particle diameter is very much smaller than the other, it should suffice to replace the energy tensors by their traces, assuming as a consequence that the velocity covariance tensors are isotropic.

https://doi.org/10.1017/jfm.2019.608 Published online by Cambridge University Press

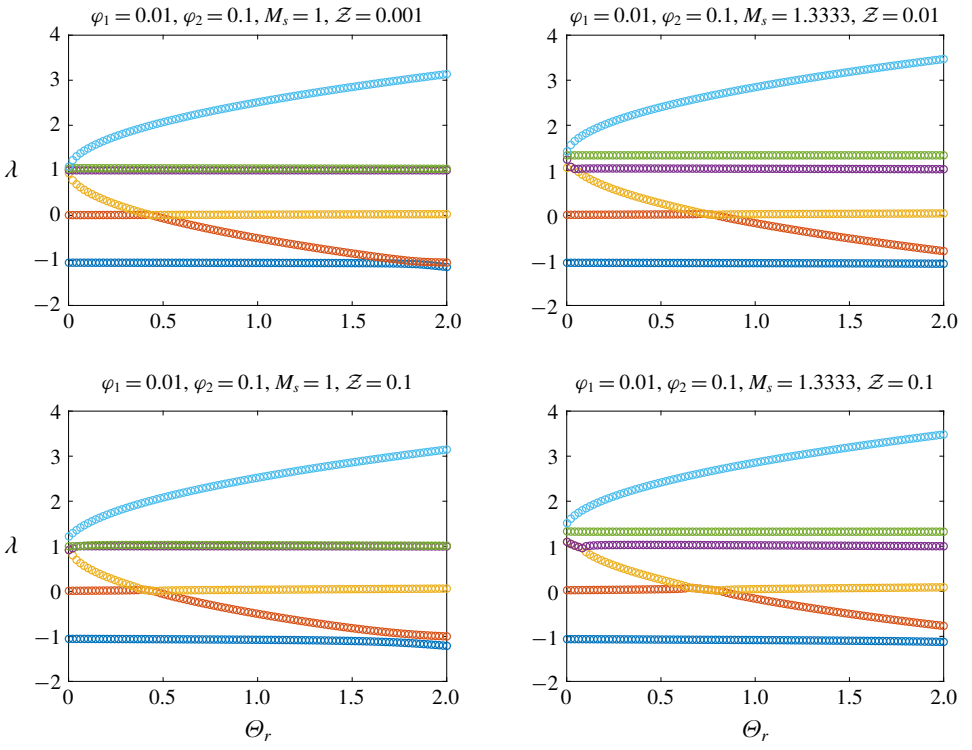


FIGURE 9. (Colour online) Real part of eigenvalues versus Θ_r for non-ideal gas ($\varphi_1 = 0.01$) with $\mathcal{Z} = 0.001$, 0.01, 0.1 and $Ma_s = 1$ and 4/3. Values of Ma_s and φ_2 are chosen to cross curves with a negative Sturm test function in figures 6–8.

The resulting fluid–particle model employs ten variables and the BE tensors only modify the momentum and energy fluxes in the fluid phase (see table 3). The 1-D version of the complete model (see table 4) has been analysed using Sturm's Theorem to determine under what conditions the system is hyperbolic. The overall conclusion from this analysis is that the 1-D model is hyperbolic for physically realistic model parameters, provided that the Mach number based on the mean-slip velocity Ma_s is not too large. Nonetheless, we must remind the reader that because the fluid–particle model derived from the BE kinetic equation only accounts for buoyancy, drag and lift terms, this model is unlikely to provide realistic predictions for larger $\mathcal{Z}$ where added-mass effects will be important.

In future work, the two-fluid model could be further developed in several directions. First, the extension to an N-component hard-sphere system with binary collisions follows immediately from the derivation of the collision integrals in appendix A (Kong & Fox 2019). For multi-component systems, the definition of y will depend on the collision partners α and β, as will parameters such as χ_α and μ_α. The formulae in appendix A apply for $d_\alpha \leqslant d_\beta$; however, they can be used for $d_\alpha \geqslant d_\beta$ if y and $1 - y$ are replaced by $1 - y$ and y, respectively. Second, the two-fluid model can be modified to account for inelastic collisions by employing the formulae in appendix A with $\omega_\alpha = \frac{1}{2}(1 + e)\mu_\alpha$ and $e < 1$. Again, care should be taken to use the restitution coefficient e appropriate for the collision pair. However, in order to account for the loss of kinetic energy due to inelastic collisions, it will

https://doi.org/10.1017/jfm.2019.608 Published online by Cambridge University Press

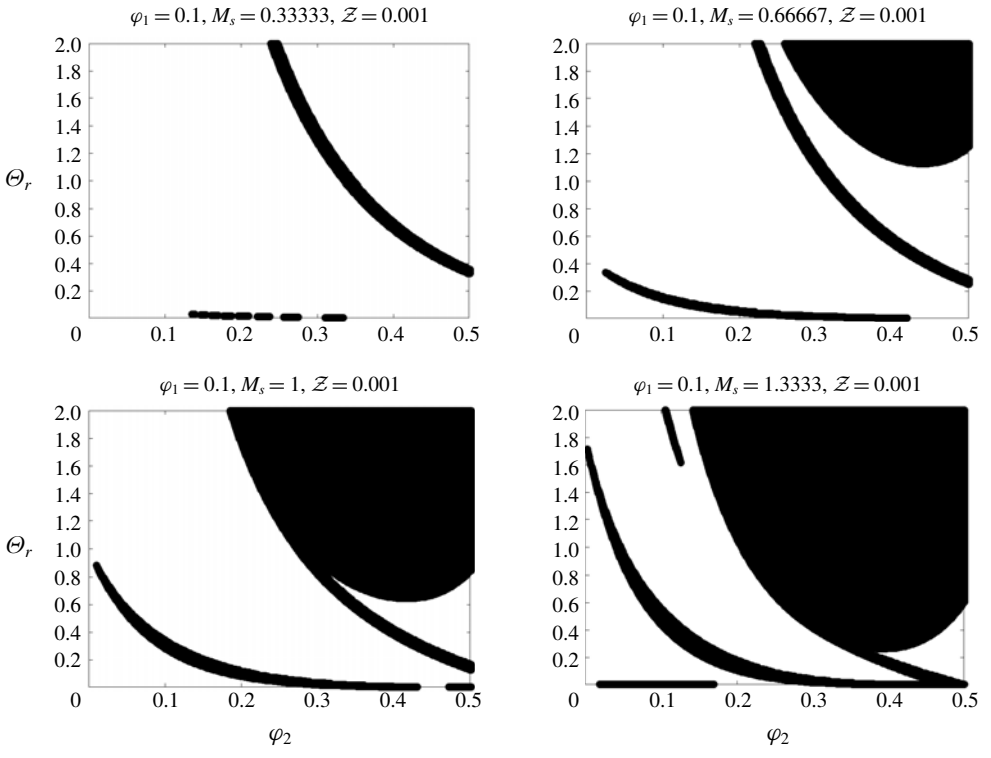


FIGURE 10. Hyperbolicity plot for dense gas ($\varphi_1 = 0.1$) with $\mathcal{Z} = 0.001$ and varying Ma_s and φ_2. The Sturm test function is negative in black regions, indicating that the 1-D model has complex eigenvalues.

be necessary to model the thermal energy of the particles, and then heat transfer between the fluid and particle phases (see Houim & Oran (2016) for an example). Third, in order to treat finite-size particles with $\varphi_2 > 0.5$, it will be necessary to add a frictional pressure term in the particle-phase momentum balance, as well as a frictional damping term in the particle-phase energy equation (see Kong & Fox (2017) for an example). Fourth, the two-fluid model in table 3 could be modified to account for added mass with a stiffened gas equation of state to handle the fluid phase. In this manner, it may be possible to investigate bubbly flows where $\rho_f \gg \rho_p$. Fifth, in order to model multi-species reacting flows, transport equations for the species mass fractions must be included for both phases, which will result in mass, momentum and energy-exchange terms between phases, as well as chemical reaction terms in each phase (see Houim & Oran (2016) for an example). Finally, it would be enlightening to extend the Euler-level model in table 3 to the Navier–Stokes level using a Chapman–Enskog expansion (Chapman & Cowling 1952) to determine the effective fluid- and particle-phase viscous stress tensors. These results could then be compared to those derived using volume averaging by Chu & Prosperetti (2016).

Another aspect that merits further investigation is the description of kinetic-energy transfer from the finite-size particles to the fluid phase. From the two-fluid model equations in table 3, we can observe that the fluid-phase kinetic energy is transferred from the particles to the fluid by drag, i.e. $K(3\Theta_p + |\boldsymbol{u}_{fp}|^2)$. As a result of this energy transfer, for finite-size particles pseudo-turbulent Reynolds stresses are generated

https://doi.org/10.1017/jfm.2019.608 Published online by Cambridge University Press

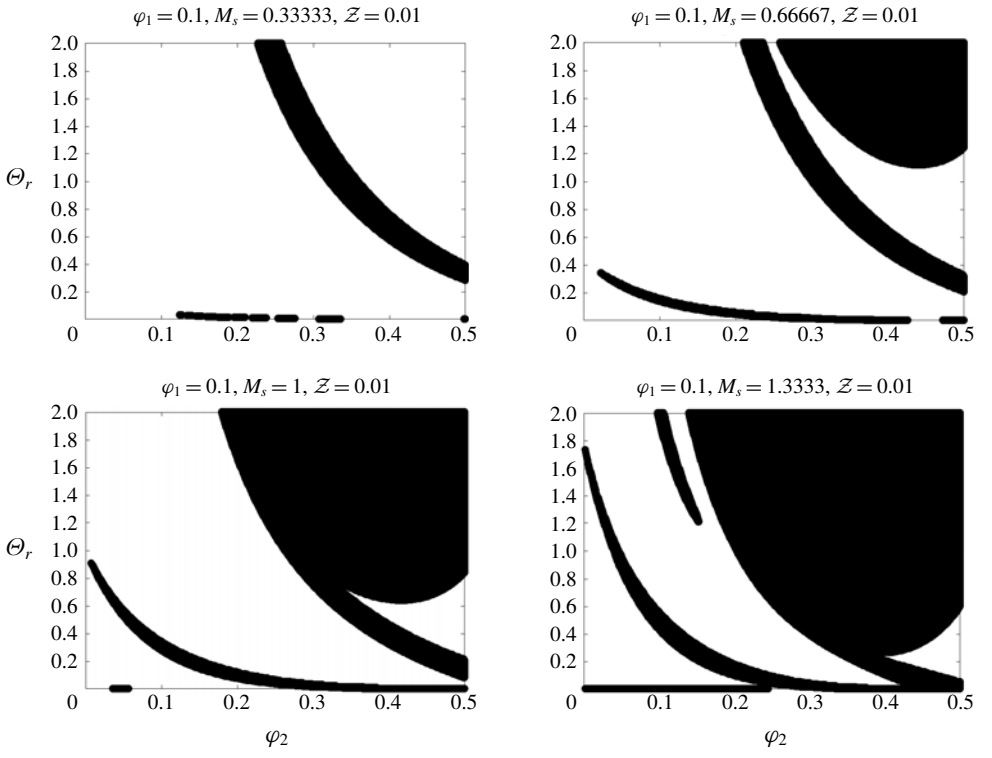


FIGURE 11. Hyperbolicity plot for dense gas ($\varphi_1 = 0.1$) with $\mathcal{Z} = 0.01$ and varying Ma_s and φ_2. The Sturm test function is negative in black regions, indicating that the 1-D model has complex eigenvalues.

in the fluid phase (Zhang *et al.* 2006; Tenneti & Subramaniam 2014; Mehrabadi *et al.* 2015; Maxey 2017; Risso 2018). With this mechanism in mind, it would be interesting (see Fox 2014, for a detailed discussion of how this is done at the macroscale) to derive a transport equation for the pseudo-turbulent Reynolds stresses. For the limiting case where the pseudo-turbulent Reynolds stresses are in dynamic equilibrium, an algebraic model could be employed (Shallcross, Fox & Capecelatro 2019). In any case, such a mesoscale transport model would have the potential to describe the anisotropic transport in 3-D compressible particle-laden flows due to pseudo-turbulence as observed experimentally (Ling *et al.* 2012; Wagner *et al.* 2012; Theofanous *et al.* 2016, 2018) and in direct-numerical simulations (Mehta, Jackson & Balachandar 2019; Osnes *et al.* 2019).

In summary, the main conclusion that can be drawn from this work is that, starting from a well-defined microscale description, it is possible to derive a hyperbolic two-fluid model wherein the fluxes and source terms have unambiguous definitions. The ramifications in the more general context of two-fluid modelling are manifold (see, for example, Zhang *et al.* 2006; Minier 2015, for an overview of other approaches). However, the most significant may be that 'generic' two-fluid models with simple definitions of the spatial fluxes and source terms do not exist, but rather the flow-specific microscale physics must be taken into account for each system. From a modelling perspective, the inclusion of physics-based source terms in two-fluid models is likely to be relatively straightforward (e.g. using correlations

https://doi.org/10.1017/jfm.2019.608 Published online by Cambridge University Press

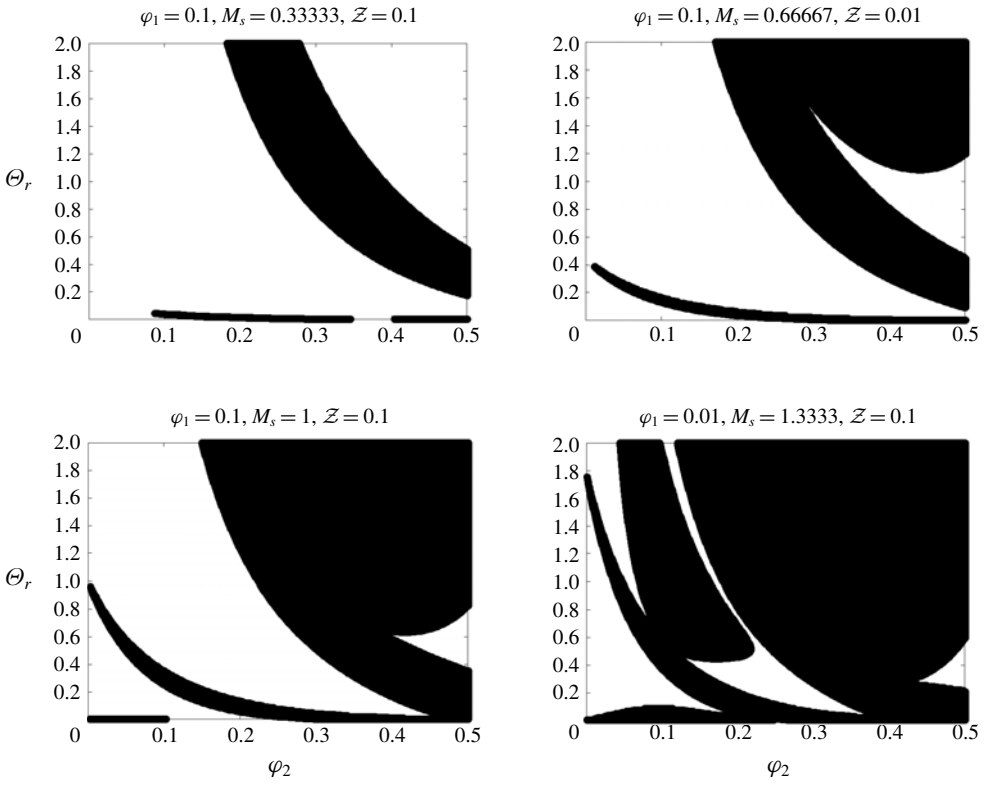


FIGURE 12. Hyperbolicity plot for dense gas ($\varphi_1 = 0.1$) with $\mathcal{Z} = 0.1$ and varying Ma_s and φ_2. The Sturm test function is negative in black regions, indicating that the 1-D model has complex eigenvalues.

found from direct-numerical simulations (Tenneti & Subramaniam 2014)). Thus, the greater challenge in the formulation of two-fluid models for other disperse systems will be to find consistent (non-equilibrium) flux models, which, as shown here and in Zhang *et al.* (2006), can potentially depend on all of the phase variables.

Acknowledgements

This research was supported by grants from the U.S. National Science Foundation (CBET-1437865 and ACI-1440443). The author gratefully acknowledges the Francqui Foundation, Belgium, for support as an International Francqui Professor, for the period during which this research was initiated.

Appendix A. Boltzmann–Enskog kinetic theory for hard spheres

In this appendix, we describe how the collisional flux and source terms in the moment equations are derived starting from the Boltzmann–Enskog kinetic equation. The reader interested in more details (particularly on the method to evaluate the collision integrals) should consult Fox & Vedula (2010) and chap. 6 in Marchisio & Fox (2013). In addition to the notation introduced in § 2, we define the unit vector

https://doi.org/10.1017/jfm.2019.608 Published online by Cambridge University Press

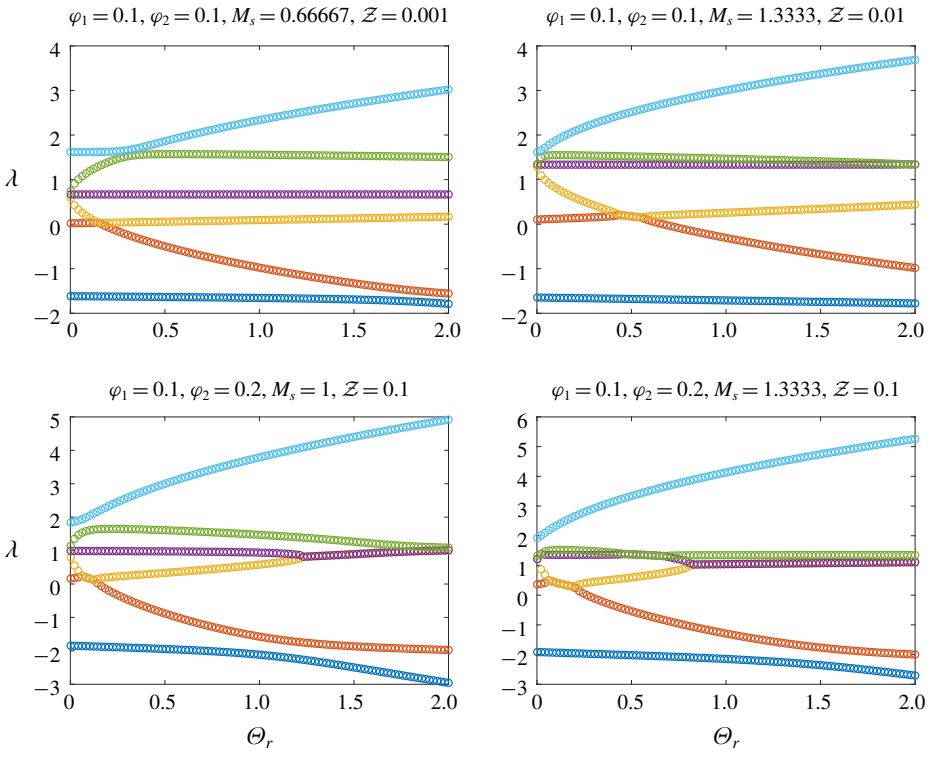


FIGURE 13. (Colour online) Real part of eigenvalues versus Θ_r for dense gas ($\varphi_1 = 0.1$) with $\mathcal{Z} = 0.010$, 0.01, 0.1 and $Ma_s = 2/3$, 1 and 4/3. Values of Ma_s and φ_2 are chosen to cross curves with a negative Sturm test function in figures 10–12.

(see figure 14)

$$\boldsymbol{x}_{12} := \frac{\boldsymbol{x}_2 - \boldsymbol{x}_1}{|\boldsymbol{x}_2 - \boldsymbol{x}_1|}, \tag{A 1}$$

in the direction between the particle centres (i.e. the collision vector), and $\boldsymbol{v}_{12} = \boldsymbol{v}_1 - \boldsymbol{v}_2$ (with magnitude v_{12}), which is the velocity difference before a direct collision. The surface $\mathbb{S}^+$ is the unit half-sphere on which $\boldsymbol{v}_{12} \cdot \boldsymbol{x}_{12} = v_{12} \cos\theta > 0$ (i.e. velocity differences that result in collisions), where θ is the collision angle (whose value is such that $\cos\theta$ is positive when collisions occur). Allowing for inelastic collisions, we define $\omega_\alpha = \frac{1}{2}(1+e)\mu_\alpha$ where $0 \leqslant e \leqslant 1$ is the coefficient of restitution, taken to be independent of the collision velocity. For the elastic collisions in the main text $e = 1$ so that $\omega_\alpha = \mu_\alpha$. In general, e depends on the properties of the particle pair.

In order to write the formulae for the collision integral, we introduce the particle-pair distribution function $f^{(2)}(\boldsymbol{x}_1, m_1, \boldsymbol{v}_1; \boldsymbol{x}_2, m_2, \boldsymbol{v}_2)$, which is proportional to the probability of finding a particle of type-1 at location $\boldsymbol{x}_1$ with velocity $\boldsymbol{v}_1$ and a particle of type-2 at location $\boldsymbol{x}_2$ with velocity $\boldsymbol{v}_2$. (The particle masses m_α do not change during collisions. We include them in the definition of $f^{(2)}$ to indicate dependence on the particle types.) As is well known (Chapman & Cowling 1952; Cercignani 1988), in the kinetic theory of hard-sphere collisions the closure of $f^{(2)}$ in terms of the one-particle VDFs f_α in (2.1) is the principal challenge, especially for finite-size particles. In the approach used here, first the model for $f^{(2)}$ is specified,

https://doi.org/10.1017/jfm.2019.608 Published online by Cambridge University Press

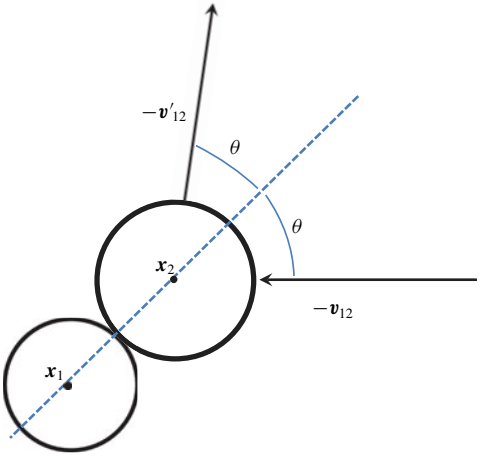


FIGURE 14. (Colour online) Direct collision between two hard spheres with diameters $d_1 < d_2$. At contact, the sphere centres are located at $\boldsymbol{x}_1$ and $\boldsymbol{x}_2$, and the relative velocity is $\boldsymbol{v}_{12} = \boldsymbol{v}_1 - \boldsymbol{v}_2$.

then the integral over $\mathbb{S}^+$ is performed for an arbitrary form for f_α. In some cases, the integrals with respect to the velocity can be performed exactly (e.g. the spatial fluxes), while for others (e.g. the source terms) these integrals must be approximated using classical methods (see, e.g. Morse 1963; Andries *et al.* 2002). As noted in the main text, of primary interest are the Boltzmann–Enskog terms arising due to finite-size particles.

A.1. *Collision integrals in BE kinetic equation*

The hard-sphere collision model for the change of $f_1(t, \boldsymbol{x}, \boldsymbol{v}_1)$ in (2.1) is given by $\mathcal{C}_1 = \mathcal{C}_{11} + \mathcal{C}_{12}$ for like collisions (the particle masses m_α appear in these expressions because f_α is defined to be the mass VDF, as opposed to the number VDF, in the main text)

$$\mathcal{C}_{11}(\boldsymbol{x}, \boldsymbol{v}_1) := \frac{d_1^2}{m_1} \int_{\mathbb{R}^3} \int_{\mathbb{S}^+} \left[\frac{1}{e^2} f^{(2)}(\boldsymbol{x}, m_1, \boldsymbol{v}_1''; \boldsymbol{x} - d_1 \boldsymbol{x}_{12}, m_1, \boldsymbol{v}_2'') - f^{(2)}(\boldsymbol{x}, m_1, \boldsymbol{v}_1; \boldsymbol{x} + d_1 \boldsymbol{x}_{12}, m_1, \boldsymbol{v}_2) \right] |\boldsymbol{v}_{12} \cdot \boldsymbol{x}_{12}| \mathrm{d}\boldsymbol{x}_{12} \, \mathrm{d}\boldsymbol{v}_2, \tag{A 2}$$

and unlike collisions

$$\mathcal{C}_{12}(\boldsymbol{x}, \boldsymbol{v}_1) := \frac{d^2}{m_2} \int_{\mathbb{R}^3} \int_{\mathbb{S}^+} \left[\frac{1}{e^2} f^{(2)}(\boldsymbol{x}, m_1, \boldsymbol{v}_1''; \boldsymbol{x} - d \boldsymbol{x}_{12}, m_2, \boldsymbol{v}_2'') - f^{(2)}(\boldsymbol{x}, m_1, \boldsymbol{v}_1; \boldsymbol{x} + d \boldsymbol{x}_{12}, m_2, \boldsymbol{v}_2) \right] |\boldsymbol{v}_{12} \cdot \boldsymbol{x}_{12}| \mathrm{d}\boldsymbol{x}_{12} \, \mathrm{d}\boldsymbol{v}_2, \tag{A 3}$$

where $1/e^2$ is a factor relating the pre-collision velocities for direct collisions $(\boldsymbol{v}_1, \boldsymbol{v}_2)$ to those for inverse collisions $(\boldsymbol{v}_1'', \boldsymbol{v}_2'')$. The collision integral over $\mathbb{S}^+$ accounts for all initial positions leading to a binary collision for given values of $\boldsymbol{v}_1$ and $\boldsymbol{v}_2$. The

https://doi.org/10.1017/jfm.2019.608 Published online by Cambridge University Press

positive term in the collision model corresponds to collisions that produce a particle of type-1 with velocity $\boldsymbol{v}_1$, while the negative term corresponds to particles of type-1 changing velocity due to a collision.

The pre-collision velocities are related by

$$\left.\begin{aligned}\boldsymbol{v}_1 &= \boldsymbol{v}_1'' - \omega_\alpha(\boldsymbol{v}_{12}''\cdot\boldsymbol{x}_{12})\boldsymbol{x}_{12},\\ \boldsymbol{v}_2 &= \boldsymbol{v}_2'' + \omega_\alpha(\boldsymbol{v}_{12}''\cdot\boldsymbol{x}_{12})\boldsymbol{x}_{12},\end{aligned}\right\} \tag{A 4}$$

where $\boldsymbol{v}_{12}'' = \boldsymbol{v}_1'' - \boldsymbol{v}_2''$ (with magnitude v_{12}'') is the velocity difference before an inverse collision. Note that the post-collision velocities after direct collisions are given by

$$\left.\begin{aligned}\boldsymbol{v}_1' &= \boldsymbol{v}_1 - \omega_\alpha(\boldsymbol{v}_{12}\cdot\boldsymbol{x}_{12})\boldsymbol{x}_{12},\\ \boldsymbol{v}_2' &= \boldsymbol{v}_2 + \omega_\alpha(\boldsymbol{v}_{12}\cdot\boldsymbol{x}_{12})\boldsymbol{x}_{12}.\end{aligned}\right\} \tag{A 5}$$

Thus, each direct collision can result in a loss of energy, the amount of which depends on e

$$m_1\boldsymbol{v}_1\cdot\boldsymbol{v}_1 + m_2\boldsymbol{v}_2\cdot\boldsymbol{v}_2 \geqslant m_1\boldsymbol{v}_1'\cdot\boldsymbol{v}_1' + m_2\boldsymbol{v}_2'\cdot\boldsymbol{v}_2', \tag{A 6}$$

where (as in the main text) the equality holds for $e = 1$. On the other hand, both mass and momentum are conserved during collisions. In any case, it is necessary to provide a closure for the particle-pair distribution function appearing in (A 2) and (A 3) in order to evaluate the collision integrals.

A.2. *Collision terms for moments*

We express (2.1) as

$$\partial_t f_1 + \boldsymbol{v}\cdot\partial_{\boldsymbol{x}} f_1 = \mathcal{C}_{11} + \mathcal{C}_{12}, \quad \partial_t f_2 + \boldsymbol{v}\cdot\partial_{\boldsymbol{x}} f_2 = \mathcal{C}_{22} + \mathcal{C}_{21}, \tag{A 7a,b}$$

where $\mathcal{C}_{\alpha\beta}$ denotes a collision integral of the form given in § A.1. As in the main text, we are interested in moments of the VDF, which can be expressed in terms of the functional (for moments up to second order, the relevant functions are $\psi = 1$, $\psi = \boldsymbol{v}$ and $\psi = \boldsymbol{v}\otimes\boldsymbol{v}$. The mathematical manipulations can be done with these definitions in place of (A 8), directly yielding the tensor forms for the collisional fluxes and source terms)

$$\psi(\boldsymbol{v}) := v_1^{l_1} v_2^{l_2} v_3^{l_3}, \tag{A 8}$$

where (l_1, l_2, l_3) are non-negative integers dependent of the order of the moment of interest. In particular, we will need $l_1 + l_2 + l_3 = 0$, $l_1 + l_2 + l_3 = 1$, and $l_1 + l_2 + l_3 = 2$, corresponding to mass, momentum and energy. The rate of change of the moments due to collisions is

$$\mathbb{C}_{\alpha\beta}(\psi) := \int_{\mathbb{R}^3} \psi(\boldsymbol{v}_\alpha)\mathcal{C}_{\alpha\beta}(\boldsymbol{x}, \boldsymbol{v}_\alpha)\,\mathrm{d}\boldsymbol{v}_\alpha, \tag{A 9}$$

for like ($\alpha = \beta$) and unlike ($\alpha \neq \beta$) particles.

For an arbitrary functional $\psi(\boldsymbol{v})$, the unlike collision terms can be written as (see Fox & Vedula (2010) and Marchisio & Fox (2013) for details)

$$\begin{aligned}\mathbb{C}_{12}(\psi) \;=\; & \frac{6\chi_2^3}{\pi\rho_2 d}\int_{\mathbb{R}^6}\int_{\mathbb{S}^+}[\psi(\boldsymbol{v}_1') - \psi(\boldsymbol{v}_1)]\\ & \times f^{(2)}(\boldsymbol{x}, m_1, \boldsymbol{v}_1; \boldsymbol{x} + d\,\boldsymbol{x}_{12}, m_2, \boldsymbol{v}_2)|\boldsymbol{v}_{12}\cdot\boldsymbol{x}_{12}|\mathrm{d}\boldsymbol{x}_{12}\,\mathrm{d}\boldsymbol{v}_2\,\mathrm{d}\boldsymbol{v}_1,\end{aligned} \tag{A 10}$$

https://doi.org/10.1017/jfm.2019.608 Published online by Cambridge University Press

and

$$\mathbb{C}_{21}(\psi) = \frac{6\chi_1^3}{\pi\rho_1 d}\int_{\mathbb{R}^6}\int_{\mathbb{S}^+}[\psi(\boldsymbol{v}_2')-\psi(\boldsymbol{v}_2)] \times f^{(2)}(\boldsymbol{x}-d\boldsymbol{x}_{12}, m_1, \boldsymbol{v}_1; \boldsymbol{x}, m_2, \boldsymbol{v}_2)|\boldsymbol{v}_{12}\cdot\boldsymbol{x}_{12}|\mathrm{d}\boldsymbol{x}_{12}\,\mathrm{d}\boldsymbol{v}_2\,\mathrm{d}\boldsymbol{v}_1. \quad (A\,11)$$

Note that the same formulae hold for like collisions (i.e. $d\to d_\alpha$ and $\chi_\alpha = 1$). In (A 10) and (A 11), the primed velocities are related to the unprimed velocities by (A 5). Using a Taylor series, we can write

$$\left.\begin{aligned}\psi(\boldsymbol{v}_1')-\psi(\boldsymbol{v}_1) &= \textstyle\sum_{n=1}^{\infty}\dfrac{(-\omega_2)^n}{n!}(\boldsymbol{v}_{12}\cdot\boldsymbol{x}_{12})^n(\boldsymbol{x}_{12}\cdot\boldsymbol{\nabla}_v)^n\psi(\boldsymbol{v}_1),\\ \psi(\boldsymbol{v}_2')-\psi(\boldsymbol{v}_2) &= \textstyle\sum_{n=1}^{\infty}\dfrac{(\omega_1)^n}{n!}(\boldsymbol{v}_{12}\cdot\boldsymbol{x}_{12})^n(\boldsymbol{x}_{12}\cdot\boldsymbol{\nabla}_v)^n\psi(\boldsymbol{v}_2),\end{aligned}\right\} \quad (A\,12)$$

where $\boldsymbol{\nabla}_v$ is the gradient operator with respect to $\boldsymbol{v}$. For integer moments, the summations on the right-hand side are finite (i.e. for $n > l_1+l_2+l_3$ the gradients are null). As shown in detail in chap. 6 of Marchisio & Fox (2013), the integrals over the collision angles $\mathbb{S}^+$ in (A 10) and (A 11) can be evaluated exactly after a closure is provided for the particle-pair distribution function.

A.3. *BE expansion for collisional sources and fluxes*

In the next step, the collision integrals are expanded around a point between $\boldsymbol{x}_1$ and $\boldsymbol{x}_2$. This procedure yields collisional source terms and collisional fluxes in the moment equations of the form (Chapman & Cowling 1952; Fox & Vedula 2010):

$$\mathbb{C}_{\alpha\beta}(\psi) = C_{\alpha\beta}(\psi) - \partial_{\boldsymbol{x}}\cdot\boldsymbol{G}_{\alpha\beta}(\psi). \quad (A\,13)$$

As is strictly valid for hard-sphere systems (Barajas *et al.* 1973), only the zero- and first-order terms are kept in (A 13) (see chap. 6 in Marchisio & Fox 2013, for the complete expansion). The expansion point $\boldsymbol{x}$ is determined using a geometric parameter y, whose definition is provided by (2.9) in the main text. Hereinafter, we assume that $d_1 \leqslant d_2$ so that at contact the particle centres are related to the expansion point by $\boldsymbol{x}_1 = \boldsymbol{x} - yd\boldsymbol{x}_{12}$ and $\boldsymbol{x}_2 = \boldsymbol{x} + (1-y)d\boldsymbol{x}_{12}$. The resulting collisional source terms are

$$C_{12}(\psi) = \frac{6\chi_2^3}{\pi\rho_2 d}\int_{\mathbb{R}^6}\int_{\mathbb{S}^+}[\psi(\boldsymbol{v}_1')-\psi(\boldsymbol{v}_1)] \times f^{(2)}(\boldsymbol{x}-yd\boldsymbol{x}_{12}, m_1, \boldsymbol{v}_1; \boldsymbol{x}+(1-y)d\boldsymbol{x}_{12}, m_2, \boldsymbol{v}_2)|\boldsymbol{v}_{12}\cdot\boldsymbol{x}_{12}|\mathrm{d}\boldsymbol{x}_{12}\,\mathrm{d}\boldsymbol{v}_2\,\mathrm{d}\boldsymbol{v}_1, \quad (A\,14)$$

and

$$C_{21}(\psi) = \frac{6\chi_1^3}{\pi\rho_1 d}\int_{\mathbb{R}^6}\int_{\mathbb{S}^+}[\psi(\boldsymbol{v}_2')-\psi(\boldsymbol{v}_2)] \times f^{(2)}(\boldsymbol{x}-yd\boldsymbol{x}_{12}, m_1, \boldsymbol{v}_1; \boldsymbol{x}+(1-y)d\boldsymbol{x}_{12}, m_2, \boldsymbol{v}_2)|\boldsymbol{v}_{12}\cdot\boldsymbol{x}_{12}|\mathrm{d}\boldsymbol{x}_{12}\,\mathrm{d}\boldsymbol{v}_2\,\mathrm{d}\boldsymbol{v}_1; \quad (A\,15)$$

the collisional fluxes are

$$\boldsymbol{G}_{12}(\psi) = -\frac{6\chi_2^3 y}{\pi\rho_2}\int_{\mathbb{R}^6}\int_{\mathbb{S}^+}\boldsymbol{x}_{12}[\psi(\boldsymbol{v}_1')-\psi(\boldsymbol{v}_1)] \times f^{(2)}(\boldsymbol{x}-yd\boldsymbol{x}_{12}, m_1, \boldsymbol{v}_1; \boldsymbol{x}+(1-y)d\boldsymbol{x}_{12}, m_2, \boldsymbol{v}_2)|\boldsymbol{v}_{12}\cdot\boldsymbol{x}_{12}|\mathrm{d}\boldsymbol{x}_{12}\,\mathrm{d}\boldsymbol{v}_2\,\mathrm{d}\boldsymbol{v}_1, \quad (A\,16)$$

https://doi.org/10.1017/jfm.2019.608 Published online by Cambridge University Press

and

$$\boldsymbol{G}_{21}(\psi) = \frac{6\chi_1^3(1-y)}{\pi\rho_1}\int_{\mathbb{R}^6}\int_{\mathbb{S}^+}\boldsymbol{x}_{12}[\psi(\boldsymbol{v}_2')-\psi(\boldsymbol{v}_2)] \times f^{(2)}(\boldsymbol{x}-yd\boldsymbol{x}_{12}, m_1, \boldsymbol{v}_1; \boldsymbol{x}+(1-y)d\boldsymbol{x}_{12}, m_2, \boldsymbol{v}_2)|\boldsymbol{v}_{12}\cdot\boldsymbol{x}_{12}|\,\mathrm{d}\boldsymbol{x}_{12}\,\mathrm{d}\boldsymbol{v}_2\,\mathrm{d}\boldsymbol{v}_1. \quad (A\,17)$$

Note that although these terms are exact, they remain unclosed until we have related $f^{(2)}$ to the one-particle VDFs.

A.4. *Model for particle-pair distribution function*

The next step needed to close the moment equations is to provide a model for the particle-pair distribution function. Keeping terms up to first order, we propose the model in (2.6). The functions h_1 and h_2 are chosen such that the isotropic flux pressure and the buoyancy pressure are identical for each phase. For a binary hard-sphere fluid with no mean slip, g_{12} is well described by the approximation in (2.11) (Santos *et al.* 1999; Hansen-Goos & Roth 2006). However, in the presence of significant mean slip, one could expect a higher collision frequency on the upstream side of the slower particles. For example, to describe this situation, one might use a function of the form

$$g_{12} = g_{0,12}\left(1-\frac{\kappa}{\sqrt{\Theta}}\boldsymbol{u}_{12}\cdot\boldsymbol{x}_{12}\right), \quad (A\,18)$$

where $\boldsymbol{u}_{12}$ is the mean-slip velocity defined in the main text. More generally, g_{12} must be a non-negative scalar function of (possibly) $\boldsymbol{x}_{12}$ and of the moments of the VDFs. Hereinafter, we will employ the model in (2.11), but keep in mind that it has limited accuracy when the mean-slip velocity is large relative to $\sqrt{\Theta}$. Furthermore, this model does not include terms to model other forces, such as added mass or particle–particle interactions mediated by the other component; hence, the resulting two-fluid model will be limited to gas–solid flows wherein such forces are negligible.

A.5. *Collisional source terms and fluxes for integer moments*

Having defined all of the models needed to close the BE collision terms, we can now write the collisional source term in two parts corresponding to the two terms in (2.6)

$$C_{12}(\psi) = C_{12}^{(0)}(\psi) + C_{12}^{(1)}(\psi), \quad (A\,19)$$

where the 'drag' contribution is

$$C_{12}^{(0)}(\psi) = \frac{6\chi_2^3 g_{12}}{\pi\rho_2 d}\sum_{n=1}^{\infty}\frac{(-\omega_2)^n}{n!}\int_{\mathbb{R}^6}\left(\int_{\mathbb{S}^+}(\boldsymbol{v}_{12}\cdot\boldsymbol{x}_{12})^{n+1}(\boldsymbol{x}_{12}\cdot\nabla_v)^n\psi(\boldsymbol{v}_1)\,\mathrm{d}\boldsymbol{x}_{12}\right) \times f_1 f_2\,\mathrm{d}\boldsymbol{v}_2\,\mathrm{d}\boldsymbol{v}_1, \quad (A\,20)$$

and the gradient contribution is

$$C_{12}^{(1)}(\psi) = \frac{6\chi_2^3}{\pi\rho_2}\sum_{n=1}^{\infty}\frac{(-\omega_2)^n}{n!}\int_{\mathbb{R}^6}\left(\int_{\mathbb{S}^+}\boldsymbol{x}_{12}\,(\boldsymbol{v}_{12}\cdot\boldsymbol{x}_{12})^{n+1}(\boldsymbol{x}_{12}\cdot\nabla_v)^n\psi(\boldsymbol{v}_1)\,\mathrm{d}\boldsymbol{x}_{12}\right) \cdot\left[\frac{(1-y)}{\mathcal{V}_{12}}\varrho_1 f_1^\star\partial_{\boldsymbol{x}}(h_2 f_2) - \frac{y}{\mathcal{V}_{12}}\varrho_2 f_2^\star\partial_{\boldsymbol{x}}(h_1 f_1)\right]\mathrm{d}\boldsymbol{v}_2\,\mathrm{d}\boldsymbol{v}_1. \quad (A\,21)$$

https://doi.org/10.1017/jfm.2019.608 Published online by Cambridge University Press

Likewise, the collisional flux term is

$$\boldsymbol{G}_{12}(\psi) = -\frac{6\chi_2^3 g_{12} y}{\pi\rho_2}\sum_{n=1}^{\infty}\frac{(-\omega_2)^n}{n!} \times \int_{\mathbb{R}^6}\left(\int_{\mathbb{S}^+}\boldsymbol{x}_{12}\,(\boldsymbol{v}_{12}\cdot\boldsymbol{x}_{12})^{n+1}(\boldsymbol{x}_{12}\cdot\nabla_v)^n\psi(\boldsymbol{v}_1)\,\mathrm{d}\boldsymbol{x}_{12}\right) f_1 f_2\,\mathrm{d}\boldsymbol{v}_2\,\mathrm{d}\boldsymbol{v}_1. \quad (A\,22)$$

Similar expressions are found for C_{21} and $\boldsymbol{G}_{21}$. It is interesting to note that the gradient contribution and the collisional flux both arise from the same collision integral in the BE approximation. This would imply that adding exchange forces to a consistent two-fluid model may require corresponding changes to the spatial fluxes.

The two integrals in parenthesis in (A 20) and (A 21) over the collision angles $\mathbb{S}^+$ can be done analytically (see chap. 16 in Chapman & Cowling (1952) for examples). (These two integrals differ by the presence of the vector $\boldsymbol{x}_{12}$ in the second, which is dotted with the spatial gradient. In general, adding more terms in the BE expansions will add more vector products of $\boldsymbol{x}_{12}$. In Marchisio & Fox (2013) results for the next collision integral involving $\boldsymbol{x}_{12}\otimes\boldsymbol{x}_{12}$ are provided.) (The same integral appears in (A 21) and (A 22).) The detailed manipulations are given in Marchisio & Fox (2013). For the results below, we make use of the identities

$$f_1^\star\partial_{\boldsymbol{x}}(h_2 f_2) = \partial_{\boldsymbol{x}}(h_2 f_2 f_1^\star) - h_2 f_2\partial_{\boldsymbol{x}} f_1^\star, \quad f_2^\star\partial_{\boldsymbol{x}}(h_1 f_1) = \partial_{\boldsymbol{x}}(h_1 f_1 f_2^\star) - h_1 f_1\partial_{\boldsymbol{x}} f_2^\star. \quad (A\,23a,b)$$

For integer moments with ψ defined by (A 8), the final results are

$$C^{(0)}_{l_1l_2l_3,12} = \frac{6\rho_1\chi_2^3 g_{12}\varphi_1\varphi_2}{d}\int_{\mathbb{R}^6} I^{(0)}_{l_1l_2l_3}(\omega_2,\boldsymbol{v}_1,\boldsymbol{v}_1-\boldsymbol{v}_2)|\boldsymbol{v}_1-\boldsymbol{v}_2|f_1^\star f_2^\star\,\mathrm{d}\boldsymbol{v}_1\,\mathrm{d}\boldsymbol{v}_2, \quad (A\,24)$$

$$C^{(0)}_{l_1l_2l_3,21} = \frac{6\rho_2\chi_1^3 g_{12}\varphi_1\varphi_2}{d}\int_{\mathbb{R}^6} I^{(0)}_{l_1l_2l_3}(-\omega_1,\boldsymbol{v}_2,\boldsymbol{v}_1-\boldsymbol{v}_2)|\boldsymbol{v}_1-\boldsymbol{v}_2|f_1^\star f_2^\star\,\mathrm{d}\boldsymbol{v}_1\,\mathrm{d}\boldsymbol{v}_2, \quad (A\,25)$$

$$\begin{aligned} C^{(1)}_{l_1l_2l_3,12} = {} & \frac{3\rho_1}{4y}\sum_{m=1}^{3}\int_{\mathbb{R}^6} I^{(m)}_{l_1l_2l_3}(\omega_2,\boldsymbol{v}_1,\boldsymbol{v}_1-\boldsymbol{v}_2) \\ & \times\left[y\varphi_2\frac{\partial}{\partial x_m}(h_1\varphi_1 f_1^\star f_2^\star) - (1-y)\varphi_1\frac{\partial}{\partial x_m}(h_2\varphi_2 f_1^\star f_2^\star)\right]\mathrm{d}\boldsymbol{v}_1\,\mathrm{d}\boldsymbol{v}_2 \\ & -\frac{3\rho_1}{4y}\sum_{m=1}^{3}\int_{\mathbb{R}^6} I^{(m)}_{l_1l_2l_3}(\omega_2,\boldsymbol{v}_1,\boldsymbol{v}_1-\boldsymbol{v}_2) \\ & \times\left[y\varphi_2 h_1\varphi_1 f_1^\star\frac{\partial f_2^\star}{\partial x_m} - (1-y)\varphi_1 h_2\varphi_2 f_2^\star\frac{\partial f_1^\star}{\partial x_m}\right]\mathrm{d}\boldsymbol{v}_1\,\mathrm{d}\boldsymbol{v}_2, \end{aligned} \quad (A\,26)$$

$$\begin{aligned} C^{(1)}_{l_1l_2l_3,21} = {} & \frac{3\rho_2}{4(1-y)}\sum_{m=1}^{3}\int_{\mathbb{R}^6} I^{(m)}_{l_1l_2l_3}(-\omega_1,\boldsymbol{v}_2,\boldsymbol{v}_1-\boldsymbol{v}_2) \\ & \times\left[y\varphi_2\frac{\partial}{\partial x_m}(h_1\varphi_1 f_1^\star f_2^\star) - (1-y)\varphi_1\frac{\partial}{\partial x_m}(h_2\varphi_2 f_1^\star f_2^\star)\right]\mathrm{d}\boldsymbol{v}_1\,\mathrm{d}\boldsymbol{v}_2 \end{aligned}$$

https://doi.org/10.1017/jfm.2019.608 Published online by Cambridge University Press

$$-\frac{3\rho_2}{4(1-y)}\sum_{m=1}^{3}\int_{\mathbb{R}^6} I^{(m)}_{l_1l_2l_3}(-\omega_1,\,\boldsymbol{v}_2,\,\boldsymbol{v}_1-\boldsymbol{v}_2)$$
$$\times\left[y\varphi_2 h_1\varphi_1 f_1^\star\frac{\partial f_2^\star}{\partial x_m}-(1-y)\varphi_1 h_2\varphi_2 f_2^\star\frac{\partial f_1^\star}{\partial x_m}\right]\mathrm{d}\boldsymbol{v}_1\,\mathrm{d}\boldsymbol{v}_2, \tag{A 27}$$

and, for the mth component of $\boldsymbol{G}$,

$$G_{m,l_1l_2l_3,12}=6\rho_1\chi_2^3 g_{12}y\varphi_1\varphi_2\int_{\mathbb{R}^6} I^{(m)}_{l_1l_2l_3}(\omega_2,\,\boldsymbol{v}_1,\,\boldsymbol{v}_1-\boldsymbol{v}_2)f_1^\star f_2^\star\,\mathrm{d}\boldsymbol{v}_1\,\mathrm{d}\boldsymbol{v}_2, \tag{A 28}$$

$$G_{m,l_1l_2l_3,21}=6\rho_2\chi_1^3 g_{12}(y-1)\varphi_1\varphi_2\int_{\mathbb{R}^6} I^{(m)}_{l_1l_2l_3}(-\omega_1,\,\boldsymbol{v}_2,\,\boldsymbol{v}_1-\boldsymbol{v}_2)f_1^\star f_2^\star\,\mathrm{d}\boldsymbol{v}_1\,\mathrm{d}\boldsymbol{v}_2. \tag{A 29}$$

The first contribution in (A 26) and (A 27) has the same phase-space integral as in (A 28) and (A 29), while the second contribution involving the spatial derivative of the VDF is more complicated to evaluate. Nonetheless, both contributions can be computed analytically and do not depend on the form of the VDF. In the main text, the second contribution leads to the terms involving the operator $\partial^{(\alpha)}_{\boldsymbol{x}}$. The expressions for $I^{(m)}_{l_1l_2l_3}$ for moments up to second order are provided in tables 5–7 (by definition, $I^{(m)}_{000}=0$). Results for moments up to fifth order are available in Marchisio & Fox (2013).

A.6. *Integrals over velocity phase space*

The final step needed to arrive at the equations in the main text is to integrate over velocity phase space. The four integrals that must be evaluated are

$$\langle I^{(0)}_{l_1l_2l_3}\rangle_{12}=\int_{\mathbb{R}^6} I^{(0)}_{l_1l_2l_3}(\omega_2,\,\boldsymbol{v}_1,\,\boldsymbol{v}_1-\boldsymbol{v}_2)|\boldsymbol{v}_1-\boldsymbol{v}_2|f_1^\star f_2^\star\,\mathrm{d}\boldsymbol{v}_1\,\mathrm{d}\boldsymbol{v}_2, \tag{A 30}$$

$$\langle I^{(0)}_{l_1l_2l_3}\rangle_{21}=\int_{\mathbb{R}^6} I^{(0)}_{l_1l_2l_3}(-\omega_1,\,\boldsymbol{v}_2,\,\boldsymbol{v}_1-\boldsymbol{v}_2)|\boldsymbol{v}_1-\boldsymbol{v}_2|f_1^\star f_2^\star\,\mathrm{d}\boldsymbol{v}_1\,\mathrm{d}\boldsymbol{v}_2, \tag{A 31}$$

$$\langle I^{(m)}_{l_1l_2l_3}\rangle_{12}=\int_{\mathbb{R}^6} I^{(m)}_{l_1l_2l_3}(\omega_2,\,\boldsymbol{v}_1,\,\boldsymbol{v}_1-\boldsymbol{v}_2)f_1^\star f_2^\star\,\mathrm{d}\boldsymbol{v}_1\,\mathrm{d}\boldsymbol{v}_2,\quad m=1,\,2,\,3; \tag{A 32}$$

$$\langle I^{(m)}_{l_1l_2l_3}\rangle_{21}=\int_{\mathbb{R}^6} I^{(m)}_{l_1l_2l_3}(-\omega_1,\,\boldsymbol{v}_2,\,\boldsymbol{v}_1-\boldsymbol{v}_2)f_1^\star f_2^\star\,\mathrm{d}\boldsymbol{v}_1\,\mathrm{d}\boldsymbol{v}_2,\quad m=1,\,2,\,3; \tag{A 33}$$

for $l_1+l_2+l_3=1$ and $l_1+l_2+l_3=2$. Note that in (A 26) and (A 27), the integrals over the independent variables $\boldsymbol{v}_1$ and $\boldsymbol{v}_2$ can be taken inside the spatial derivatives. Integrals (A 30) and (A 31) appear in the 'drag' terms $C^{(0)}$, which do not have spatial gradients. Thus, although these integrals are not closed, they can be accurately approximated for Gaussian VDFs (i.e. see (3.5) and Andries *et al.* (2002)). Remarkably, integrals (A 32) and (A 33) are closed for arbitrary forms of the VDFs. For the first- and second-order moments, the exact integrals are given in tables 8 and 9, respectively. The results in table 8 are used with (A 32) and (A 33) to construct the second-order pressure tensor $\boldsymbol{P}_{BE}$, and those in table 9 are used to construct the third-order energy flux tensors $\boldsymbol{G}_{BE}$ given in table 1.

https://doi.org/10.1017/jfm.2019.608 Published online by Cambridge University Press

$$I^{(0)}_{000}=0 \quad I^{(0)}_{100}=-\frac{\omega}{2}g_1 \qquad I^{(0)}_{010}=-\frac{\omega}{2}g_2 \quad I^{(0)}_{001}=-\frac{\omega}{2}g_3$$
$$I^{(0)}_{200}=\frac{\omega^2}{12}g^2+\frac{\omega^2}{4}g_1^2-\omega g_1v_1 \qquad I^{(0)}_{110}=\frac{\omega^2}{4}g_1g_2-\frac{\omega}{2}g_2v_1-\frac{\omega}{2}g_1v_2$$
$$I^{(0)}_{020}=\frac{\omega^2}{12}g^2+\frac{\omega^2}{4}g_2^2-\omega g_2v_2 \qquad I^{(0)}_{101}=\frac{\omega^2}{4}g_1g_3-\frac{\omega}{2}g_3v_1-\frac{\omega}{2}g_1v_3$$
$$I^{(0)}_{002}=\frac{\omega^2}{12}g^2+\frac{\omega^2}{4}g_3^2-\omega g_3v_3 \qquad I^{(0)}_{011}=\frac{\omega^2}{4}g_2g_3-\frac{\omega}{2}g_3v_2-\frac{\omega}{2}g_2v_3$$

TABLE 5. $I^{(0)}_{l_1l_2l_3}(\omega,\boldsymbol{v},\boldsymbol{g})$ for moments up to second order.

$$I^{(1)}_{100}=\frac{2\omega}{15}(g^2+2g_1^2) \qquad I^{(2)}_{100}=\frac{4\omega}{15}g_1g_2 \qquad I^{(3)}_{100}=\frac{4\omega}{15}g_1g_3$$
$$I^{(1)}_{010}=\frac{4\omega}{15}g_1g_2 \qquad I^{(2)}_{010}=\frac{2\omega}{15}(g^2+2g_2^2) \qquad I^{(3)}_{010}=\frac{4\omega}{15}g_2g_3$$
$$I^{(1)}_{001}=\frac{4\omega}{15}g_1g_3 \qquad I^{(2)}_{001}=\frac{4\omega}{15}g_2g_3 \qquad I^{(3)}_{001}=\frac{2\omega}{15}(g^2+2g_3^2)$$

TABLE 6. $I^{(m)}_{l_1l_2l_3}(\omega,\boldsymbol{v},\boldsymbol{g})$ for first-order moments with $m=1,2,3$.

$$I^{(1)}_{200}=-\frac{2\omega^2}{35}(3g^2+2g_1^2)g_1+\frac{4\omega}{15}(g^2+2g_1^2)v_1$$
$$I^{(1)}_{110}=-\frac{2\omega^2}{35}(g^2+2g_1^2)g_2+\frac{4\omega}{15}g_1g_2v_1+\frac{2\omega}{15}(g^2+2g_1^2)v_2$$
$$I^{(1)}_{101}=-\frac{2\omega^2}{35}(g^2+2g_1^2)g_3+\frac{4\omega}{15}g_1g_3v_1+\frac{2\omega}{15}(g^2+2g_1^2)v_3$$
$$I^{(1)}_{020}=-\frac{2\omega^2}{35}(g^2+2g_2^2)g_1+\frac{8\omega}{15}g_1g_2v_2$$
$$I^{(1)}_{011}=-\frac{4\omega^2}{35}g_1g_2g_3+\frac{4\omega}{15}g_1g_3v_2+\frac{4\omega}{15}g_1g_2v_3$$
$$I^{(1)}_{002}=-\frac{2\omega^2}{35}(g^2+2g_3^2)g_1+\frac{8\omega}{15}g_1g_3v_3$$

TABLE 7. $I^{(1)}_{l_1l_2l_3}(\omega,\boldsymbol{v},\boldsymbol{g})$ for second-order moments. The corresponding terms for $m=2$ and 3 can be found by a permutation of the indices.

Appendix B. Body forces

Let $\boldsymbol{g}$ be the acceleration due to a body force (e.g. gravity) acting on each particle. The kinetic equations with a body force are

$$\partial_t f_1+\boldsymbol{v}\cdot\partial_{\boldsymbol{x}}f_1+\boldsymbol{g}\cdot\partial_{\boldsymbol{v}}f_1=\mathcal{C}_1, \quad \partial_t f_2+\boldsymbol{v}\cdot\partial_{\boldsymbol{x}}f_2+\boldsymbol{g}\cdot\partial_{\boldsymbol{v}}f_2=\mathcal{C}_2. \tag{B 1a,b}$$

The body force has no effect on the mass balances. For the momentum and energy balances, the new source terms appearing on the right-hand sides are

$$\boldsymbol{F}_\alpha:=-\int_{\mathbb{R}^3}\boldsymbol{v}\,\boldsymbol{g}\cdot\partial_{\boldsymbol{v}}f_\alpha\,\mathrm{d}\boldsymbol{v}=\varrho_\alpha\boldsymbol{g}, \quad \text{and} \quad \boldsymbol{\mathcal{E}}_\alpha:=-\frac{1}{2}\int_{\mathbb{R}^3}\boldsymbol{v}\otimes\boldsymbol{v}\,\boldsymbol{g}\cdot\partial_{\boldsymbol{v}}f_\alpha\,\mathrm{d}\boldsymbol{v}=\varrho_\alpha(\boldsymbol{g}\otimes\boldsymbol{u}_\alpha)^\dagger. \tag{B 2a,b}$$

https://doi.org/10.1017/jfm.2019.608 Published online by Cambridge University Press

$$\langle I^{(1)}_{100}\rangle_{12} = \frac{4\omega_2}{15}\left(\frac{3}{2}\Theta + \sigma_{11,1} + \sigma_{11,2} + u^2_{1,12}\right)$$
$$\langle I^{(2)}_{100}\rangle_{12} = \frac{4\omega_2}{15}(\sigma_{12,1} + \sigma_{12,2} + u_{1,12}u_{2,12})$$
$$\langle I^{(3)}_{100}\rangle_{12} = \frac{4\omega_2}{15}(\sigma_{13,1} + \sigma_{13,2} + u_{1,12}u_{3,12})$$
$$\langle I^{(1)}_{010}\rangle_{12} = \frac{4\omega_2}{15}(\sigma_{12,1} + \sigma_{12,2} + u_{1,12}u_{2,12})$$
$$\langle I^{(2)}_{010}\rangle_{12} = \frac{4\omega_2}{15}\left(\frac{3}{2}\Theta + \sigma_{22,1} + \sigma_{22,2} + u^2_{2,12}\right)$$
$$\langle I^{(3)}_{010}\rangle_{12} = \frac{4\omega_2}{15}(\sigma_{23,1} + \sigma_{23,2} + u_{2,12}u_{3,12})$$
$$\langle I^{(1)}_{001}\rangle_{12} = \frac{4\omega_2}{15}(\sigma_{13,1} + \sigma_{13,2} + u_{1,12}u_{3,12})$$
$$\langle I^{(2)}_{001}\rangle_{12} = \frac{4\omega_2}{15}(\sigma_{23,1} + \sigma_{23,2} + u_{2,12}u_{3,12})$$
$$\langle I^{(3)}_{001}\rangle_{12} = \frac{4\omega_2}{15}\left(\frac{3}{2}\Theta + \sigma_{33,1} + \sigma_{33,2} + u^2_{3,12}\right)$$

TABLE 8. $\langle I^{(m)}_{l_1l_2l_3}\rangle_{12}$ for first-order moments with $m = 1, 2, 3$. $\langle I^{(m)}_{l_1l_2l_3}\rangle_{21}$ is found by replacing ω_2 with $-\omega_1$. Here $\boldsymbol{u}_{12} = \boldsymbol{u}_1 - \boldsymbol{u}_2$ is the mean velocity difference with components $u_{i,12}$; Θ is defined in (2.5) and $\sigma_{ij,1}$, $\sigma_{ij,2}$ are the components of the velocity covariance tensors. Note that these integrals can be written as a second-order symmetric tensor, i.e. $(4\omega_2/15)(\frac{3}{2}\Theta\boldsymbol{I} + \boldsymbol{\sigma}_1 + \boldsymbol{\sigma}_2 + \boldsymbol{u}_{12}\otimes\boldsymbol{u}_{12})$. This tensor appears in the main text in the definition of the collisional contribution to the granular pressure tensor $\boldsymbol{P}_{BE}$.

$$\langle I^{(1)}_{200}\rangle_{12} = -\frac{4\omega_2^2}{35}\left(\frac{3}{2}\langle g^2 g_1\rangle + \langle g_1^3\rangle\right) + \frac{8\omega_2}{15}\left(\frac{1}{2}\langle g^2 v_{1,1}\rangle + \langle g_1^2 v_{1,1}\rangle\right)$$
$$\langle I^{(1)}_{110}\rangle_{12} = -\frac{4\omega_2^2}{35}\left(\frac{1}{2}\langle g^2 g_2\rangle + \langle g_1^2 g_2\rangle\right) + \frac{4\omega_2}{15}\left(\langle g_1 g_2 v_{1,1}\rangle + \frac{1}{2}\langle g^2 v_{2,1}\rangle + \langle g_1^2 v_{2,1}\rangle\right)$$
$$\langle I^{(1)}_{101}\rangle_{12} = -\frac{4\omega_2^2}{35}\left(\frac{1}{2}\langle g^2 g_3\rangle + \langle g_1^2 g_3\rangle\right) + \frac{4\omega_2}{15}\left(\langle g_1 g_3 v_{1,1}\rangle + \frac{1}{2}\langle g^2 v_{3,1}\rangle + \langle g_1^2 v_{3,1}\rangle\right)$$
$$\langle I^{(1)}_{020}\rangle_{12} = -\frac{4\omega_2^2}{35}\left(\frac{1}{2}\langle g^2 g_1\rangle + \langle g_2^2 g_1\rangle\right) + \frac{8\omega_2}{15}\langle g_1 g_2 v_{2,1}\rangle$$
$$\langle I^{(1)}_{011}\rangle_{12} = -\frac{4\omega_2^2}{35}\langle g_1 g_2 g_3\rangle + \frac{4\omega_2}{15}(\langle g_1 g_3 v_{2,1}\rangle + \langle g_1 g_2 v_{3,1}\rangle)$$
$$\langle I^{(1)}_{002}\rangle_{12} = -\frac{4\omega_2^2}{35}\left(\frac{1}{2}\langle g^2 g_1\rangle + \langle g_3^2 g_1\rangle\right) + \frac{8\omega_2}{15}\langle g_1 g_3 v_{3,1}\rangle$$

TABLE 9. $\langle I^{(1)}_{l_1l_2l_3}\rangle_{12}$ for second-order moments. The expressions for $m = 2$ and 3 can be found by permutation of the indices. $\langle I^{(1)}_{l_1l_2l_3}\rangle_{21}$ is found by replacing ω_2 with $-\omega_1$ and $\boldsymbol{v}_1$ by $\boldsymbol{v}_2$. The expected values on the right-hand sides are given in terms of the velocity moments in table 10. Note that these integrals can be written as a third-order tensor, which appears in the main text in the definition of the collisional contribution to the energy flux tensor $\boldsymbol{G}_{BE}$.

https://doi.org/10.1017/jfm.2019.608 Published online by Cambridge University Press

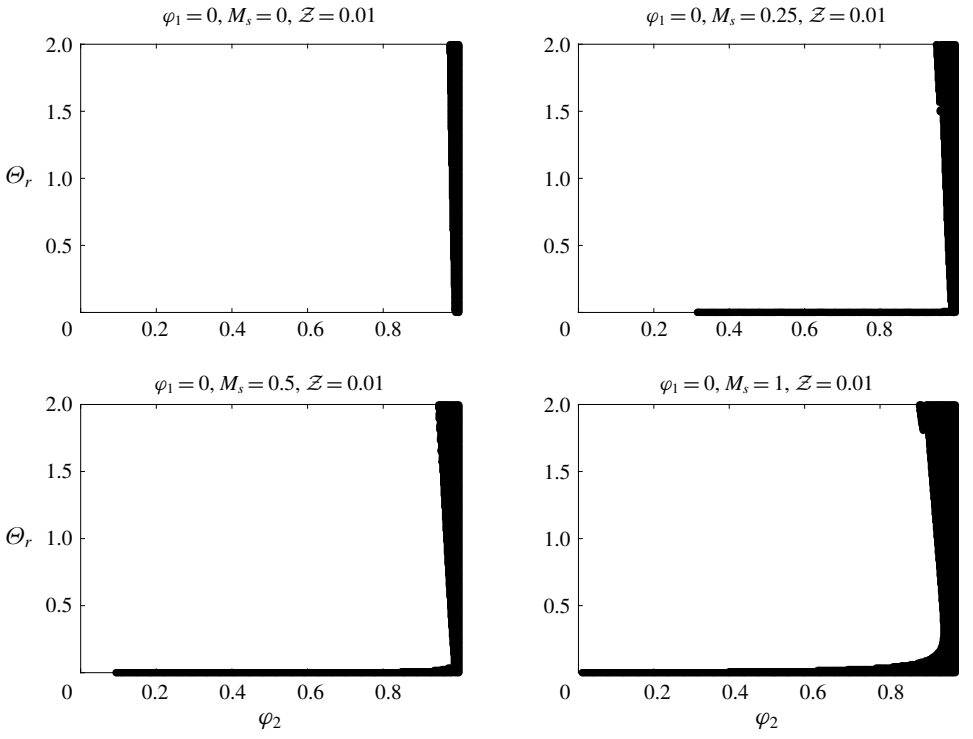


FIGURE 15. Hyperbolicity plot for perfect gas and $g_0 = 0$ with $\mathcal{Z} = 0.01$ and varying Ma_s. The Sturm test function is negative in black regions, indicating that the 1-D model has complex eigenvalues.

$$\langle g_i g_j v_{k,1} \rangle = Q_{ijk,1} + u_{i,12}\sigma_{jk,1} + u_{j,12}\sigma_{ik,1} + u_{k,1}(\sigma_{ij,1} + \sigma_{ij,2}) + u_{i,12}u_{j,12}u_{k,1}$$
$$\langle g_i g_j v_{k,2} \rangle = Q_{ijk,2} - u_{i,12}\sigma_{jk,2} - u_{j,12}\sigma_{ik,2} + u_{k,2}(\sigma_{ij,1} + \sigma_{ij,2}) + u_{i,12}u_{j,12}u_{k,2}$$
$$\langle g_i g_j g_k \rangle = \langle g_i g_j v_{k,1} \rangle - \langle g_i g_j v_{k,2} \rangle \quad \langle g^2 g_k \rangle = \sum_{i=1}^{3} \langle g_i g_i g_k \rangle$$
$$\langle g^2 v_{k,1} \rangle = \sum_{i=1}^{3} \langle g_i g_i v_{k,1} \rangle \quad \langle g^2 v_{k,2} \rangle = \sum_{i=1}^{3} \langle g_i g_i v_{k,2} \rangle$$

TABLE 10. Definitions of terms appearing in $\langle I^{(m)}_{l_1 l_2 l_3} \rangle_{12}$ and $\langle I^{(m)}_{l_1 l_2 l_3} \rangle_{21}$ for second-order moments in table 9. The symbols are defined as follows: $\boldsymbol{u}_{12} = \boldsymbol{u}_1 - \boldsymbol{u}_2$ is the mean velocity difference with components $u_{i,12}$; $\boldsymbol{\sigma}_1$, $\boldsymbol{\sigma}_2$ are the velocity covariance tensors with components $\sigma_{ij,1}$, $\sigma_{ij,2}$; and $\boldsymbol{Q}_1$, $\boldsymbol{Q}_2$ are the third-order central velocity moment tensors with components $Q_{ijk,1}$, $Q_{ijk,2}$. For Gaussian velocity distributions, $\boldsymbol{Q}$ is null. Note that these formulae also hold with like particles where $\boldsymbol{u}_{11}$ is null.

These terms are included in the compressible gas–particle two-fluid model in table 3.

Unlike the interaction terms, the body force is non-conservative: $\boldsymbol{F}_1 + \boldsymbol{F}_2 = (\varrho_1 + \varrho_2)\boldsymbol{g}$ and $\mathcal{E}_1 + \mathcal{E}_2 = (\varrho_1 \boldsymbol{u}_1 + \varrho_2 \boldsymbol{u}_2) \cdot \boldsymbol{g}$. Note that the fluctuating energy source terms, $\mathcal{E}_\alpha - \boldsymbol{u}_\alpha \cdot \boldsymbol{F}_\alpha$, are null, and thus the body force does not appear in the transport equations for Θ_α. As body forces do not involve spatial nor temporal gradients, they do not affect the hyperbolicity of the two-fluid model.

https://doi.org/10.1017/jfm.2019.608 Published online by Cambridge University Press

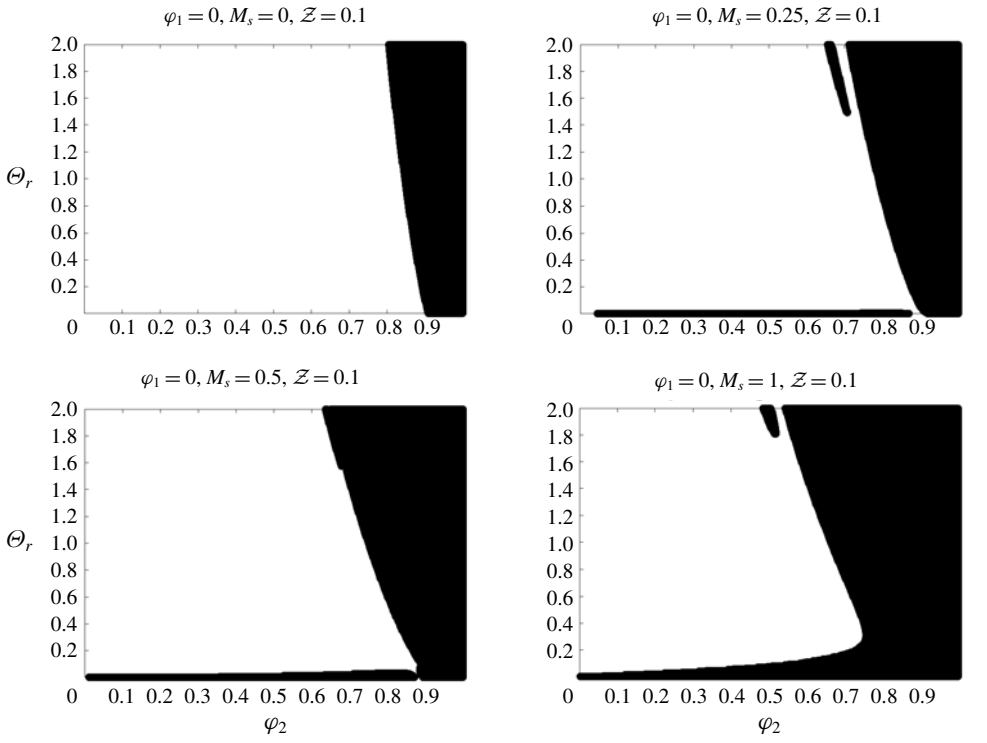


FIGURE 16. Hyperbolicity plot for perfect gas and $g_0 = 0$ with $\mathcal{Z} = 0.1$ and varying Ma_s. The Sturm test function is negative in black regions, indicating that the 1-D model has complex eigenvalues.

Appendix C. Two-fluid model with $g_0 = 0$

In order to isolate the effect of non-ideal behaviour in the particle phase, we can set $g_0 = 0$ so that $p_p = \rho_p \alpha_p \Theta_p$ and treat the gas phase as perfect as done in § 5.3. The characteristic polynomial for this case has a much simpler form due to the absence of the nonlinear dependence of g_0 on φ. In fact, with $M_s = 0$ it is possible to compute the eigenvalues analytically using symbolic software. The hyperbolicity plots for $\mathcal{Z} = 0.01$ and 0.1 are shown in figures 15 and 16, respectively. Note that in these figures the range of φ_2 has been extended up to 1. It can be observed that this system is hyperbolic almost everywhere in parameter space. For fixed $\mathcal{Z}$ and increasing Ma_s, the non-hyperbolic region increases along the axis $\Theta_r = 0$, moving inward from the right.

In general, increasing $\mathcal{Z}$ results in a larger region of non-hyperbolic behaviour. Compared to the perfect-gas model presented in § 5.3, neglecting g_0 for the particle phase increases the range of parameters for which the 1-D model is hyperbolic. As noted in the main text, for non-negligible values of the density ratio $\mathcal{Z}$ the effect of added mass should be significant and will affect the eigenvalues near $\Theta_r = 0$. Thus, by including a model for added mass, we would expect to recover hyperbolicity along the axis $\Theta_r = 0$, leaving only the vertically oriented non-hyperbolic region associated with large φ_2 in figures 15 and 16. In future work, it would be interesting to explore (i) why adding g_0 to the particle-phase pressure increases the non-hyperbolic regions significantly, (ii) if this observation depends on added mass and (iii) whether

https://doi.org/10.1017/jfm.2019.608 Published online by Cambridge University Press

additional physics-based coupling terms (e.g. form of interspecies stress tensor) would remove this dependency.

REFERENCES

AGRAWAL, K., LOEZOS, P. N., SYAMLAL, M. & SUNDARESAN, S. 2001 The role of meso-scale structures in rapid gas–solid flows. *J. Fluid Mech.* **445**, 151–185.

ANDRIES, P., AOKI, K. & PERTHAME, B. 2002 A consistent BGK-type model for gas mixtures. *J. Stat. Phys.* **106** (5/6), 993–1018.

BARAJAS, L., GARCIA-COLIN, L. S. & PINÃ, E. 1973 On the Enskog–Thorne theory for a binary mixture of dissimilar rigid spheres. *J. Stat. Phys.* **7** (2), 161–183.

BLANC, F., LEMAIRE, É, MUENIER, A. & PETERS, F. 2013 Microstructure in sheared non-Brownian concentrated suspensions. *J. Rheol.* **57**, 273–292.

BUYEVICH, Y. A. & SHCHELCHKOVA, I. N. 1978 Flow of dense suspensions. *Prog. Aerosp. Sci.* **18**, 121–150.

CAPECELATRO, J. & DESJARDINS, O. 2013 An Euler–Lagrange strategy for simulating particle-laden flows. *J. Comput. Phys.* **238**, 1–31.

CAPECELATRO, J., DESJARDINS, O. & FOX, R. O. 2015 On fluid–particle dynamics in fully developed cluster-induced turbulence. *J. Fluid Mech.* **780**, 578–635.

CAPECELATRO, J., DESJARDINS, O. & FOX, R. O. 2016*a* Strongly coupled fluid–particle flows in vertical channels. I. Reynolds-averaged two-phase turbulence statistics. *Phys. Fluids* **28**, 033306.

CAPECELATRO, J., DESJARDINS, O. & FOX, R. O. 2016*b* Strongly coupled fluid–particle flows in vertical channels. II. Turbulence modeling. *Phys. Fluids* **28**, 033307.

CAPECELATRO, J., DESJARDINS, O. & FOX, R. O. 2018 On the transition between turbulence regimes in particle-laden channel flows. *J. Fluid Mech.* **845**, 499–519.

CARNAHAN, N. F. & STARLING, K. E. 1969 Equation of state for nonattracting rigid spheres. *J. Chem. Phys.* **51**, 635–636.

CERCIGNANI, C. 1988 *The Boltzmann Equation and Its Applications*. Springer.

CHALONS, C., FOX, R. O., LAURENT, F., MASSOT, M. & VIÉ, A. 2017 Multivariate Gaussian extended quadrature method of moments for turbulent fluid–particle flows. *Multiscale Model. Simul.* **15** (4), 1553–1583.

CHAPMAN, S. 1912 Kinetic theory of a gas constituted of spherically symmetrical molecules. *Phil. Trans. R. Soc.* A **211**, 433–483.

CHAPMAN, S. & COWLING, T. G. 1952 *The Mathematical Theory of Non-Uniform Gases*, 2nd edn. Cambridge University Press.

CHLIAMOVITCH, C., MALASPINAS, O. & CHOPARD, B. 2017 Kinetic theory beyond the Stosszahlansatz. *Entropy* **19**, 381.

CHU, S. & PROSPERETTI, A. 2016 On flux terms in volume averaging. *Intl J. Multiphase Flow* **80**, 176–180.

CRAVATH, A. M. 1930 The rate at which ions lose energy in elastic collisions. *Phys. Rev.* **36**, 248–250.

DESJARDINS, O., FOX, R. O. & VILLEDIEU, P. 2008 A quadrature-based moment method for dilute fluid–particle flows. *J. Comput. Phys.* **227** (4), 2514–2539.

DREW, P. A. & PASSMAN, S. L. 1998 *Theory of Multicomponent Fluids*. Springer.

ENSKOG, D. 1911*a* Bemerkungen zu einer Fundamentalgleichung in der kinetishen Gastheorie. *Phys. Z.* **12**, 533–539.

ENSKOG, D. 1911*b* Über eine Verallgemeinerung de zweiten Maxwellschen Theorie der Gase. *Phys. Z.* **12**, 56–60.

FÉVRIER, P., SIMONIN, O. & SQUIRES, K. D. 2005 Partitioning of particle velocities in gas–solid turbulent flow into a continuous field and a spatially uncorrelated random distribution: theoretical formalism and numerical study. *J. Fluid Mech.* **533**, 1–46.

https://doi.org/10.1017/jfm.2019.608 Published online by Cambridge University Press

Fox, R. O. 2008 A quadrature-based third-order moment method for dilute gas–particle flow. *J. Comput. Phys.* **227** (12), 6313–6350.

Fox, R. O. 2009 Higher-order quadrature-based moment methods for kinetic equations. *J. Comput. Phys.* **228**, 7771–7791.

Fox, R. O. 2012 Large-eddy-simulation tools for multiphase flows. *Annu. Rev. Fluid Mech.* **44**, 47–76.

Fox, R. O. 2014 On multiphase turbulence models for collisional fluid–particle flows. *J. Fluid Mech.* **742**, 368–424.

Fox, R. O., Laurent, F. & Massot, M. 2008 Numerical simulation of spray coalescence in an Eulerian framework: direct quadrature method of moments and multi-fluid method. *J. Comput. Phys.* **227**, 3058–3088.

Fox, R. O., Laurent, F. & Vié, A. 2018 Conditional hyperbolic quadrature method of moments for kinetic equations. *J. Comput. Phys.* **365**, 269–293.

Fox, R. O. & Vedula, P. 2010 Quadrature-based moment method for moderately dense polydisperse gas–particle flows. *Indust. Engng Chem. Res.* **49**, 5174–5187.

Garzó, V., Dufty, J. W. & Hrenya, C. M. 2007 Enskog theory for polydisperse granular mixtures. Part 1. Navier–Stokes order transport. *Phys. Rev.* E **76**, 031303.

Garzó, V., Santos, A. & Brey, J. J. 1989 A kinetic model for a multicomponent gas. *Phys. Fluids* A **1**, 380–383.

Garzó, V., Tenneti, S., Subramaniam, S. & Hrenya, C. M. 2012 Enskog kinetic theory for monodisperse gas–solid flows. *J. Fluid Mech.* **712**, 129–168.

Goldman, E. & Sirovich, L. 1967 Equations for gas mixtures. *Phys. Fluids* **10** (9), 1928–1940.

Goldman, E. & Sirovich, L. 1969 Equations for gas mixtures. II. *Phys. Fluids* **12** (1), 245–247.

Grad, H. 1960 Theory of rarefied gases. In *Rarefied Gas Dynamics* (ed. F. Devienne). Pergamon Press.

Gross, E. P. & Krook, M. 1956 Model for collision processes in gases: small-amplitude oscillations of charged two-component systems. *Phys. Rev.* **102** (3), 593–604.

Guazzelli, É. & Pouliquen, O. 2018 Rheology of dense granular suspensions. *J. Fluid Mech.* **852**, P1-1-73.

Hamel, B. B. 1965 Kinetic model for binary gas mixtures. *Phys. Fluids* **8** (1), 418–425.

Hamel, B. B. 1966 Two-fluid hydrodynamic equations for a neutral, disparate-mass, binary mixture. *Phys. Fluids* **9** (12), 12–22.

Hank, S., Saurel, R. & Le Metayer, O. 2011 A hyperbolic Eulerian model for dilute two-phase suspensions. *J. Modern Phys.* **2**, 997–1011.

Hansen-Goos, H. & Roth, R. 2006 A new generalization of the Carnahan–Starling equation of state to additive mixtures of hard spheres. *J. Chem. Phys.* **124**, 154506.

Houim, R. W. & Oran, E. S. 2016 A multiphase model for compressible granular–gasous flows: Formulation and initial tests. *J. Fluid Mech.* **789**, 166–220.

Jackson, R. 1997 Locally averaged equations of motion for a mixture of identical spherical particles and a Newtonian fluid. *Chem. Engng Sci.* **52**, 2457–2469.

Jenkins, J. T. & Savage, S. B. 1983 A theory for the rapid flow of identical, smooth, nearly elastic, spherical particles. *J. Fluid Mech.* **130**, 187–202.

Kolodner, I. 1957 Moment description of gas mixtures, I. *Tech. Rep.* NYU–7980. Courant Institute of Mathematical Sciences, New York University.

Kong, B. & Fox, R. O. 2017 A solution algorithm for fluid–particle flows across all flow regimes. *J. Comput. Phys.* **344**, 575–594.

Kong, B. & Fox, R. O. 2019 A moment-based kinetic theory model for polydisperse gas–particle flows. *Powder Technol*; doi:10.1016/j.powtec.2019.04.031.

Kong, B., Fox, R. O., Feng, H., Capecelatro, J., Patel, R. & Desjardins, O. 2017 Euler–Euler anisotropic Gaussian mesoscale simulation of homogeneous cluster-induced gas–particle turbulence. *AIChE J.* **63** (7), 2630–2643.

Kumbaro, A. & Ndjinga, M. 2011 Influence of interfacial pressure term on the hyperbolicity of a general multifluid model. *J. Comput. Multiphase Flows* **3** (3), 177–195.

Levermore, C. D. 1996 Moment closure hierarchies for kinetic theories. *J. Stat. Phys.* **83** (5/6), 1021–1065.

https://doi.org/10.1017/jfm.2019.608 Published online by Cambridge University Press

LEVERMORE, C. D. & MOROKOFF, W. 1996 The Gaussian moment closure for gas dynamics. *SIAM J. Appl. Math.* **59**, 72–96.

LHUILLIER, D., CHANG, C.-H. & THEOFANOUS, T. G. 2013 On the quest for a hyperbolic effective-field model of disperse flows. *J. Fluid Mech.* **731**, 184–194.

LHUILLIER, D. & THEOFANOUS, T. G. 2010 Multiphase flows: compressible multi-hydrodynamics Part 1: effective field formulation of multiphase flows. In *Handbook of Nuclear Engineering* (ed. D. G. Cacuci), pp. 1813–1857. Springer.

LING, Y., WAGNER, J. L., BERESH, S. J., KEARNEY, S. P. & BALACHANDAR, S. 2012 Interaction of a planar shock wave with a dense particle curtin: modeling and experiments. *Phys. Fluids* **24**, 113301.

MARBLE, F. E. 1970 Dynamics of dusty gases. *Annu. Rev. Fluid Mech.* **2** (1), 397–446.

MARCHISIO, D. L. & FOX, R. O. 2013 *Computational Models for Polydisperse Particulate and Multiphase Systems*. Cambridge University Press.

MAXEY, M. 2017 Simulation methods for particulate flows and concentrated suspensions. *Annu. Rev. Fluid Mech.* **49**, 171–193.

MCGRATH II, T. P., ST. CLAIR, J. G. & BALACHANDAR, S. 2016 A compressible two-phase model for dispersed particle flows with application from dense to dilute regimes. *J. Appl. Phys.* **119** (17), 174903.

MEHRABADI, M., TENNETI, S., GARG, R. & SUBRAMANIAM, S. 2015 Pseudo-turbulent gas-phase velocity fluctuations in homogeneous gas–solid flow: fixed particle assemblies and freely evolving suspensions. *J. Fluid Mech.* **770**, 210–246.

MEHTA, Y., JACKSON, T. L. & BALACHANDAR, S. 2019 Pseudo-turbulence in inviscid simulations of shock interacting with a bed of randomly distributed particles. *Shock Waves* doi:10.1007/s00193-019-00905-3.

MÉTIVIER, G. 2005 Remarks on the well-posedness of the nonlinear Cauchy problem. In *Contemporary Mathematics, Geometric Analysis of PDE and Several Complex Variables*, vol. 368, pp. 337–356. American Mathematical Society.

MINIER, J.-P. 2015 On Lagrangian stochastic methods for turbulent polydisperse two-phase reactive flows. *Prog. Energy Combust. Sci.* **50**, 1–62.

MORSE, T. F. 1963 Energy and momentum exchange between nonequipartition gases. *Phys. Fluids* **6** (10), 1420–1427.

MORSE, T. F. 1964 Kinetic model equations for a gas mixture. *Phys. Fluids* **7** (12), 2012–2013.

NDJINGA, M. 2007 Influence of interfacial pressure on the hyperbolicity of the two-fluid model. *C. R. Acad. Sci. Paris* 1 **344**, 407–412.

NIGMATULIN, R. I. 1979 Spatial averaging in the mechanics of heterogeneous and dispersed systems. *Intl J. Multiphase Flow* **5**, 353–385.

OSNES, A. N., VARTDAL, M., OMANG, M. G. & REIF, B. A. P. 2019 Computational analysis of shock-induced flow through stationary particle clouds. *Intl J. Multiphase Flow* **114**, 268–286.

PANICKER, N., PASSALACQUA, A. & FOX, R. O. 2018 On the hyperbolicity of the two-fluid model for gas–liquid flows. *Appl. Math. Model.* **57**, 432–447.

PATEL, R., DESJARDINS, O., KONG, B., CAPECELATRO, J. & FOX, R. O. 2017 Verification of Eulerian–Eulerian and Eulerian–Lagrangian simulations for turbulent fluid–particle flow. *AIChE J.* **63** (12), 5396–5412.

PATEL, R. G., DESJARDINS, O. & FOX, R. O. 2019 Three-dimensional conditional hyperbolic quadrature method of moments. *J. Comput. Phys. X* **1**, 100006.

RISSO, F. 2018 Agitation, mixing, and transfers induced by bubbles. *Annu. Rev. Fluid Mech.* **50**, 25–48.

SANTOS, A., YUSTE, S. B. & LÓPEZ DE HARO, M. 1999 Equation of state of a multicomponent *d*-dimensional hard-sphere fluid. *Mol. Phys.* **96**, 1–5.

SAUREL, R. & ABGRALL, R. 1999 A multiphase Godunov method for compressible multifluid and multiphase flows. *J. Comput. Phys.* **150** (2), 425–467.

SAUREL, R., CHINNAYYA, A. & CARMOUZE, Q. 2017 Modelling compressible dense and dilute two-phase flows. *Phys. Fluids* **29**, 063301.

SHALLCROSS, G. S., FOX, R. O. & CAPECELATRO, J. 2019 A volume-filtered description of compressible particle-laden flows. *Intl J. Multiphase Flow* (submitted).

https://doi.org/10.1017/jfm.2019.608 Published online by Cambridge University Press

SINCLAIR, J. & JACKSON, R. 1989 Gas–particle flow in a vertical pipe with particle–particle interactions. *AIChE J.* **35** (9), 1473–1486.

SIROVICH, L. 1962 Kinetic modeling of gas mixtures. *Phys. Fluids* **5** (8), 908–918.

SIROVICH, L. 1963 Errata: kinetic modeling of gas mixtures. *Phys. Fluids* **6**, 598.

STRUCHTRUP, H. 2005 *Macroscopic Transport Equations for Rarefied Gas Flows*. Springer.

STURM, J. C. F. 1829 Mémoire sur la résolution des équations numériques. *Bull. Sci. Férussac* **11**, 419–425.

SYAMLAL, M. 2011 A hyperbolic model for fluid–solids two-phase flow. *Chem. Engng Sci.* **66**, 4421–4425.

TAVENASHAD, V., PASSALACQUA, A., FOX, R. O. & SUBRAMANIAM, S. 2019 Effect of density ratio on velocity fluctuations in dispersed multiphase flow from simulations of finite-size particles. *Acta Mech.* **230** (2), 469–484.

TENNETI, S. & SUBRAMANIAM, S. 2014 Particle-resolved direct numerical simulation for gas–solid flow model development. *Annu. Rev. Fluid Mech.* **46**, 199–230.

THAM, M. K. & GUBBINS, K. E. 1971 Kinetic theory of multicomponent dense fluid mixtures of rigid spheres. *J. Chem. Phys.* **55**, 268–279.

THEOFANOUS, T. G. & CHANG, C.-H. 2017 The dynamics of dense particle clouds subjected to shock waves. Part 2. Modeling/numerical issues and the way forward. *Intl J. Multiphase Flow* **89**, 177–206.

THEOFANOUS, T. G., MITKIN, V. & CHANG, C.-H. 2016 The dynamics of dense particle clouds subjected to shock waves. Part I: experiments and scaling laws. *J. Fluid Mech.* **792**, 655–681.

THEOFANOUS, T. G., MITKIN, V. & CHANG, C.-H. 2018 Shock dispersal of dilute particle clouds. *J. Fluid Mech.* **841**, 732–745.

TORRILHON, M. 2016 Modeling nonequilibrium gas flow based on moment equations. *Annu. Rev. Fluid Mech.* **48**, 429–458.

VAZQUEZ-GONZALEZ, T., LLOR, A. & FOCHESATO, C. 2016 Ransom test results from various two-fluid schemes: Is enforcing hyperbolicity a thermodynamically consistent option? *Intl J. Multiphase Flow* **81**, 104–112.

VIÉ, A., CHALONS, C., FOX, R. O., LAURENT, F. & MASSOT, M. 2011 A multi-Gaussian quadrature method of moments for simulating high-Stokes-number turbulent two-phase flows. In *Annu. Res. Briefs CTR*, pp. 309–320.

VIÉ, A., DOISNEAU, F. & MASSOT, M. 2015 On the anisotropic Gaussian velocity closure for inertial-particle laden flows. *Commun. Comput. Phys.* **17** (01), 1–46.

WAGNER, J. L., BERESH, S. J., KEARNEY, S. P., TROTT, W. M., CASTANEDA, J. N., PRUETT, B. O. & BEAR, M. R. 2012 A multiphase shock tube for shock wave interactions with dense particle fields. *Exp. Fluids* **52**, 1507–1517.

ZHANG, D. Z., MA, X. & RAUENZAHN, R. M. 2006 Interspecies stress in momentum equations for dense binary particulate systems. *Phys. Rev. Lett.* **97** (4), 048301.

ZHANG, D. Z. & PROSPERETTI, A. 1994 Averaged equations for inviscid dispersed two-phase flows. *J. Fluid Mech.* **267**, 185–219.

https://doi.org/10.1017/jfm.2019.608 Published online by Cambridge University Press